

UNIVERSITY OF TRENTO

Department of Physics



Doctoral Program in Physics

XXXII Cycle

**Laser-synthesis and optical
functionalization of NV-fluorescent
nanodiamonds for quantum sensing
applications**

PhD candidate:

Luca Basso

Supervisor:

Prof. Antonio Miotello

Co-supervisor:

Prof. Angelo Bifone

January 24th, 2020

Laser-synthesis and optical functionalization of NV-fluorescent nanodiamonds for quantum sensing applications

by

Luca Basso

B.S. in Physics University of Trento, Italy (2014)

M.S. in Physics University of Trento, Italy (2016)

Thesis submitted to the Doctoral Program in Physics in partial fulfillment of the requirements for the degree of

Doctor of Philosophy in Physics

Committee members:

Prof. Chiara Maurizio

Department of Physics and Astronomy

University of Padova, Italy

Prof. Maulik Patel

Department Mechanical Materials and Aerospace

University of Liverpool, UK

Prof. Marco Zanatta

Department of Physics

University of Trento, Italy

Abstract

The absence of a cheap and easily scalable synthesis technique for nitrogen-vacancy (NV) centers enriched nanodiamonds (NDs) is a critical factor for the development of devices based on this very peculiar nanoparticle. Indeed, the combination between the unique NV fluorescence properties and NDs characteristics allow to obtain a tool having quantum sensing capabilities, with nanometric spatial resolution, which is able to operate in a wide range of temperature, pressures and in harsh chemical conditions. NV-enriched NDs applications in nanothermometry, nanomagnetometry and in bio-imaging have already been reported. However, most of the standard fluorescent NDs production techniques present common drawbacks: poor control in NDs size distribution and in nitrogen concentration, as well as the need of post-synthesis process to clean the NDs surface from impurities and to increase the NV density. In this thesis, an alternative method for fluorescent NDs synthesis based on pulsed laser ablation (PLA) of graphite is demonstrated. After the introductory chapters on NV-centers physics and NDs properties (Chapter 2 and 3), the demonstration that PLA is a viable route for synthesis of NDs is given in Chapter 4. In particular, PLA of graphite and of diamond-like carbon is performed in water. Here, a thermodynamic model taking into account the peculiar physical processes occurring during PLA is developed to explain NDs formation. Then, synthesis of NV-enriched NDs is demonstrated through PLA of graphite in a nitrogen atmosphere (Chapter 5) and in liquid nitrogen (Chapter 6). In both chapters, the thermodynamic model is adapted to explain diamond phase formation in a gaseous environment and in a cryogenic liquid. Furthermore, NV centers optical properties are fully characterized with optically detected magnetic resonance (ODMR) spectroscopy. Finally, in Chapter 7, fluorescent NDs are produced by laser ablation of N-doped graphite in water. This particular target is then used for a quantitative comparison between the other fluorescent NDs laser-synthesis, with the aim of establishing in which condition the highest NV-center formation efficiency is achieved.

Contents

Abstract	v
1 Introduction	1
2 Quantum technologies with Nitrogen Vacancy centers	9
2.1 NV physical structure	10
2.2 Optical properties	11
2.3 Electronic structure	12
2.4 NV ground state spin Hamiltonian	15
2.5 ODMR of NV centers	20
2.6 NV applications in quantum technology	23
3 Nanodiamonds properties and synthesis	31
3.1 Nanodiamond properties and applications	31
3.2 Synthesis techniques	34
3.3 Pulsed laser ablation for nanodiamonds synthesis	40
3.3.1 Phase explosion	41
3.3.2 Pulsed laser ablation in liquid	44
4 Nanodiamonds synthesis through pulsed laser ablation	51
4.1 Introduction	52
4.2 NDs obtained through ablation of graphite in water	53
4.2.1 Experimental setup for PLA in water	53
4.2.2 Purification method	54
4.2.3 NDs characterization	56

4.3	NDs obtained through ablation of DLC	
	in water	57
4.3.1	DLC synthesis	57
4.3.2	NDs synthesis and characterization	58
4.4	Thermodynamic model	59
4.5	Conclusions	62
5	Pulsed laser deposition of NV-fluorescent nanodiamonds	65
5.1	Introduction	66
5.2	Experimental methods	67
5.2.1	Pulsed laser deposition	67
5.2.2	Sample characterization	67
5.3	Results and discussion	69
5.3.1	NDs synthesis and characterization	69
5.4	Sensing of nanodiamonds native strain field with NV centers	74
5.5	Modeling of nanodiamond formation mechanism	76
5.6	Conclusions	79
6	NV-enriched nanodiamonds through laser ablation of graphite in liquid nitrogen	83
6.1	Introduction	84
6.2	Pulsed laser ablation in liquid: experimental methods	84
6.3	Results and discussion	86
6.3.1	NDs synthesis and characterization	86
6.3.2	Thermodynamic model to explain NDs formation	90
6.4	Comparison with nitrogen atmosphere	
	PLD-synthesized fluorescent NDs	93
6.5	Conclusions	97
7	Fluorescent NDs from N-doped graphite target and comparison between different laser-synthesis techniques	101
7.1	Introduction	102
7.2	Experimental methods	103
7.2.1	N-doped target preparation	103
7.2.2	Pulsed laser ablation	103

7.2.3	Characterization techniques	104
7.3	Results and discussion	104
7.3.1	NDs synthesis and characterization	104
7.3.2	NDs production yield: role of the confining medium	107
7.3.3	NDs production yield: role of the target	109
7.4	Conclusions	111
	Conclusions	115

CONTENTS

Chapter 1

Introduction

The purpose of this thesis is the development of a novel technique for the synthesis of fluorescent nanodiamonds (NDs) for quantum sensing applications. The fluorescence of this particular nanoparticle is given by a point-defect of diamond structure called nitrogen vacancy (NV) center. This defect consists of a substitutional nitrogen atom in a diamond lattice site having as a nearest neighbor a vacancy. NV centers exist in two charge states: neutral, NV^0 , and negatively charged, NV^- . Between the two, the NV^- is the most interesting one and attracted wide research for quantum technology applications [1, 2]. The reason relies in its optical properties. The NV^- shows bright and stable photoluminescence (PL) under convenient excitation by visible light (usually a 532 nm laser source is used). The NV PL emission has zero phonon line at 637 nm, with a sideband due to NV-phonon coupling extending till ~ 800 nm. The NV emission is highly suitable for applications given its photostability (no bleaching is observed at room temperature) and the small relaxation time (~ 10 ns) [3]. However, the most important property of NV optical transitions is their dependence on electron spin-states [4]. The outcome is that NV fluorescence intensity changes in the presence of perturbations acting on the spin-state, such as electromagnetic fields. This, combined with the possibility of accurately manipulate the spin levels population in the ground state, allowed NV centers to be used as quantum sensors of environmental physical parameters, like magnetic [5] or electric fields [6] and temperature [7]. Furthermore, spin-dependent fluorescence intensity can be used to read-out the NV spin-state [8]. This property, together with the possibility of optically pump most of the electrons in a specific spin-sublevels with very large spin-coherence lifetime [9] (as long as milliseconds),

makes NV centers an ideal solid state qubit for quantum information science. Finally, it was shown that the NV spin polarization can be transferred to the surrounding environment [10], such as ^{13}C nuclear spin, opening to the potential use in nuclear magnetic resonance (NMR) applications [11]. In the last decade, the possibility of NV centers hosted by nanodiamonds (NDs) acquired a lot of attention. Nanodiamonds, that are diamonds nanoparticles having size in the nanometer range, allow to transfer at the nanoscale most of the unique properties of bulk diamond. For this reason, NDs attracted a great interest and consequent active research. These properties [12] include high hardness, the most known characteristic of diamond-phase, high thermal conductivity and electrical resistivity, chemical stability, biocompatibility, tunable surface structure and resistance to harsh environment. These physical properties make NDs suitable for many applications in different fields: tribology, catalysis [13], biomedical application [14] and drug delivery [15]. Furthermore, the combination between NDs physical and NV-centers optical properties provides a unique tool for quantum sensing: a probe that allow detection with nanoscale precision of environmental parameters in a wide range of temperature (from cryogenic to well above 300 K) and pressures, as well as in harsh chemical environments and in biological material given NDs non-toxicity. Measurements of temperature [16] and magnetic/electric fields [17] with NV-enriched NDs have already been reported. Additionally, as NDs can be chemically attached to a large variety of species (from DNA molecules to proteins) [18], NV-fluorescence can be used to track the position of the macromolecules [19]. Moreover, NDs linked to cells membrane could provide a sensor to study cell activity [20]. An efficient synthesis technique of NV-enriched NDs is then critical for the development of these and other applications. Many NDs production methods were proposed, the main ones being detonation [12] and milling [21] of macroscopic diamond synthesized either by chemical vapor deposition (CVD) or high temperature high pressure (HPHT). These standard techniques however present common drawbacks: the control of the size and shape of NDs is poor, and the synthesis process often introduced contaminants, thus requiring post-production processes to clean NDs surfaces (usually strong chemical treatments are required) [22]. Moreover, the nitrogen doping of the NDs – which is the first step to obtain NV centers – is inefficient, since only the native nitrogen atoms in the carbon precursor is exploited, resulting in NDs with small density of NV. To increase NV number, a multi-step post-synthesis treatment of the NDs is required, consisting in nitrogen ions implantation and subsequent annealing at high temperatures to create the

NV couple [23]. An alternative way for NDs production is represented by pulsed laser ablation (PLA). PLA is nowadays a standard top-down technique for the synthesis of a wide variety of nanoparticles [24]. It consists on irradiating the surface of a bulk target with short (nanoseconds) and intense (GW cm^{-2}) laser pulses: the nanoparticles are mainly formed upon a well-known physical phenomenon called phase explosion [25]. PLA can be performed in different environment, both liquid or gaseous, to cause chemical reactions between the ablated species and the atoms of the medium. When PLA is performed on a graphite target, the extreme thermodynamic condition reached during laser irradiation, namely high temperature and pressure, allows the transition of the nanodroplets expelled from the surface from graphitic-carbon into diamond. As it will be shown in this thesis, when laser ablation occurs in a nitrogen containing medium, direct synthesis of NDs containing NV-centers is obtained.

Thesis outline

The first part of this thesis describes the general context and the background in which the original work of this project is developed. Chapter 2 provides an introduction on NV centers. In particular, details on the defect physical structure and on the various terms describing the spin Hamiltonian are given. An overview of the main NV characterization technique employed here, namely optically detected magnetic resonance (ODMR) is also provided. Finally, current and potential applications in the quantum technology field, with particular attention on quantum sensing, are described.

Then, chapter 3 is dedicated to nanodiamonds. Their physical and chemical properties are fully described, together with the applications arising from those NDs peculiarities. Moreover, standard NDs synthesis such as detonation or milling are reported. The discussion here is centered on the limitations of these techniques, in order to introduce the synthesis methods developed in the experimental section of this thesis. Finally, the fundamentals of pulsed laser ablation are described, with a particular emphasis on its use for NDs production. From this point, the original work developed during the PhD project is reported.

In chapter 4, the synthesis of NDs through pulsed laser ablation of carbon materials in water is described. The carbon materials used here as a target for PLA are graphite and diamond-like carbon. The aim of this section is to prove NDs synthesis, and show their characteristics, upon PLA of graphite before moving in the synthesis of fluorescent NDs. The characterization is provided by many analytical techniques:

scanning electron microscopy (SEM) for NDs size and shape, energy dispersive X-ray spectroscopy (EDXS) for the chemical composition and Raman spectroscopy to study the crystal structure. Furthermore, a novel procedure for NDs cleaning from residual sp^2 by-products is developed. It is based on UV-irradiation of the NDs immersed in hydrogen peroxide H_2O_2 that selectively etch sp^2 carbon atoms. Moreover, a full description of the thermodynamic model developed to explain diamond-phase formation during PLA experiment of graphitic precursor is given. This model describes the multi-step process occurring during laser irradiation, where melted carbon enters in an undercooled state in which diamond forms as a metastable phase. The role of the liquid in which the target is immersed is also fully studied. This model will be then re-used and adapted to the specific cases, namely ablation in gaseous and liquid nitrogen, in the chapters 5 and 6. From here, the novel synthesis technique developed during the PhD work for synthesis of NV-enriched nanodiamonds are described. They are based in PLA of graphite in nitrogen containing media, to achieve nitrogen doping of the laser-synthesized NDs.

Chapter 5 reports on the production of fluorescent nanodiamonds upon laser ablation of a graphite target in a controlled nitrogen atmosphere. The characterization of the NDs is given, together with analysis on the formed NV centers. The latter in particular is provided by optically detected magnetic resonance (ODMR) spectroscopy, a technique that unequivocally proves presence of NV-centers in the laser-synthesized NDs. Moreover, this technique is used to measure the native strain field acting in the nanoparticles, due to high surface to volume ratio, which in turn is related to NDs diameter: the results obtained are consistent with SEM observation, thus showing the possibility to use these fluorescent NDs as sensors for physical parameters.

In chapter 6 another technique for NV-containing NDs synthesis is described. In this case, PLA of graphite is performed in liquid nitrogen. NDs are characterized also with transmission electron microscopy (TEM), and again ODMR proves the formation of NV-centers. In this chapter ODMR is used to measure and compare the quality – namely the amount of sp^2 defects – on NDs surface between this sample and the one described in chapter 5. The reported result allows to conclude that a post-process fluorescence activation is not necessary.

Finally, in chapter 7 fluorescent NDs are obtained through ablation of a N-doped graphite target in water. This target is then used to quantitative compare the optical

properties of the NV-centers laser-synthesized in different media: water, gaseous and liquid nitrogen. The results show that the best sample, in term of number of NV hosted by the NDs, is obtained for PLA in liquid nitrogen. The thermodynamic model is then used to theoretically justify this experimental observation: the explanation relies in the different thermodynamic conditions reached during ablation in liquid nitrogen, in particular the favored under cooling process responsible to graphite-diamond transition. Moreover, it is proved that the use of the N-doped graphite target could bring to a technique for the synthesis of NDs with a tunable fluorescence level, obtained by adjusting N-concentration in the initial target.

References for chapter 1

- [1] Childress, L., & Hanson, R. (2013). Diamond NV centers for quantum computing and quantum networks. *MRS bulletin*, 38(2), 134-138.
- [2] Hong, S., Grinolds, M. S., Pham, L. M., Le Sage, D., Luan, L., Walsworth, R. L., & Yacoby, A. (2013). Nanoscale magnetometry with NV centers in diamond. *MRS bulletin*, 38(2), 155-161.
- [3] Collins, A. T., Thomaz, M. F., & Jorge, M. I. B. (1983). Luminescence decay time of the 1.945 eV centre in type Ib diamond. *Journal of Physics C: Solid State Physics*, 16(11), 2177.
- [4] Doherty, M. W., Manson, N. B., Delaney, P., Jelezko, F., Wrachtrup, J., & Hollenberg, L. C. (2013). The nitrogen-vacancy colour centre in diamond. *Physics Reports*, 528(1), 1-45.
- [5] Degen, C. L. (2008). Scanning magnetic field microscope with a diamond single-spin sensor. *Applied Physics Letters*, 92(24), 243111.
- [6] Dolde, F., Fedder, H., Doherty, M. W., Nöbauer, T., Rempp, F., Balasubramanian, et al. (2011). Electric-field sensing using single diamond spins. *Nature Physics*, 7(6), 459.
- [7] Acosta, V. M., Bauch, E., Ledbetter, M. P., Waxman, A., Bouchard, L. S., & Budker, D. (2010). Temperature dependence of the nitrogen-vacancy magnetic resonance in diamond. *Physical review letters*, 104(7), 070801.
- [8] Acosta, V., & Hemmer, P. (2013). Nitrogen-vacancy centers: physics and applications. *MRS bulletin*, 38(2), 127-130.
- [9] Balasubramanian, G., Neumann, P., Twitchen, D., Markham, M., Kolesov, R., Mizuochi, et al. (2009). Ultralong spin coherence time in isotopically engineered diamond. *Nature materials*, 8(5), 383.

BIBLIOGRAPHY

- [10] Álvarez, G. A., Bretschneider, C. O., Fischer, R., London, P., Kanda, H., Onoda, S., et al. (2015). Local and bulk ^{13}C hyperpolarization in nitrogen-vacancy-centred diamonds at variable fields and orientations. *Nature communications*, 6, 8456.
- [11] King, J. P., Jeong, K., Vassiliou, C. C., Shin, C. S., Page, R. H., Avalos, C. E., et al. (2015). Room-temperature in situ nuclear spin hyperpolarization from optically pumped nitrogen vacancy centres in diamond. *Nature communications*, 6, 8965.
- [12] Mochalin, V. N., Shenderova, O., Ho, D., & Gogotsi, Y. (2012). The properties and applications of nanodiamonds. *Nature nanotechnology*, 7(1), 11.
- [13] Bogatyreva, G. P., Marinich, M. A., Ishchenko, E. V., Gvyazdovskaya, V. L., Bazalii, G. A., & Oleinik, N. A. (2004). Application of modified nanodiamonds as catalysts of heterogeneous and electrochemical catalyses. *Physics of the Solid State*, 46(4), 738-741.
- [14] Vaijayanthimala, V. & Chang, H. C. (2009). Functionalized fluorescent nanodiamonds for biomedical applications. *Nanomedicine* 4, 47-55
- [15] Zhu, Y., Li, J., Li, W., Zhang, Y., Yang, X., Chen, N., et al. (2012). The biocompatibility of nanodiamonds and their application in drug delivery systems. *Theranostics*, 2(3), 302.
- [16] Sotoma, S., Terada, D., Segawa, T. F., Igarashi, R., Harada, Y., & Shirakawa, M. (2018). Enrichment of ODMR-active nitrogen-vacancy centres in five-nanometre-sized detonation-synthesized nanodiamonds: Nanoprobes for temperature, angle and position. *Scientific reports*, 8(1), 5463.
- [17] Maze, J. R., Stanwix, P. L., Hodges, J. S., Hong, S., Taylor, J. M., Cappellaro, P., et al. (2008). Nanoscale magnetic sensing with an individual electronic spin in diamond. *Nature*, 455(7213), 644.
- [18] Krueger, A., & Lang, D. (2012). Functionality is key: recent progress in the surface modification of nanodiamond. *Advanced Functional Materials*, 22(5), 890-906.
- [19] McGuinness, L. P., Yan, Y., Stacey, A., Simpson, D. A., Hall, L. T., Maclaurin, D., et al. (2011). Quantum measurement and orientation tracking of fluorescent nanodiamonds inside living cells. *Nature nanotechnology*, 6(6), 358.
- [20] Schirhagl, R., Chang, K., Loretz, M., & Degen, C. L. (2014). Nitrogen-vacancy centers in diamond: nanoscale sensors for physics and biology. *Annual review of physical chemistry*, 65, 83-105.
- [21] Boudou, J. P., Curmi, P. A., Jelezko, F., Wrachtrup, J., Aubert, P., Sennour, M., et al. (2009). High yield fabrication of fluorescent nanodiamonds. *Nanotechnology*, 20(23), 235602.
- [22] Dolmatov, V. Y. (2001). Detonation synthesis ultradispersed diamonds: properties and applications. *Russian Chemical Reviews*, 70(7), 607-626.

- [23] Boudou, J. P., Tisler, J., Reuter, R., Thorel, A., Curmi, P. A., Jelezko, F., & Wrachtrup, J. (2013). Fluorescent nanodiamonds derived from HPHT with a size of less than 10 nm. *Diamond and Related Materials*, 37, 80-86.
- [24] Zeng, H., Du, X. W., Singh, S. C., Kulinich, S. A., Yang, S., He, J., & Cai, W. (2012). Nanomaterials via laser ablation/irradiation in liquid: a review. *Advanced Functional Materials*, 22(7), 1333-1353.
- [25] Miotello, A., & Kelly, R. (1999). Laser-induced phase explosion: new physical problems when a condensed phase approaches the thermodynamic critical temperature. *Applied Physics A*, 69(1), S67-S73.

BIBLIOGRAPHY

Chapter 2

Quantum technologies with Nitrogen Vacancy centers

Diamond naturally exists in a lot of different colors, due to the presence of crystal defects in its structure called color centers. Among the many, nitrogen-vacancy (NV) centers acquired a great interest since, in 1997, spin manipulation at 300 K was experimentally demonstrated by Wrachtrup and coworkers [1]. In the last decade, thanks to the efficient optical pumping and spin-readout, NV center has acquired a central role as a leading candidate for solid-state qubits in quantum information technologies. During this time, it was also observed that NV centers, unlike semiconductor quantum dots or others color centers, present a stable luminescence, without bleaching or blinking. Luminescence stability together with the unique NV spin-dependent optical properties has made NV centers ideal for quantum sensing applications. Furthermore, the combination between these features and the biocompatibility of (nano)diamond, opened the way to the use of nanodiamond-hosted NV centers as bio-markers in biological systems. The first sections of this chapter provides the details of the NV centers physical structure (section 2.1), optical properties (section 2.2) and electronic configuration (section 2.3). Afterwards, in section 2.4, the spin-Hamiltonian of the NV centers is constructed. In particular, the various terms of the Hamiltonian describing the coupling between NV spin states and external perturbation are discussed. The aim of this theoretical description is to give the general guidelines to interpret the experiments, so it is far from being a thorough and complete analysis of the NV physics. Optically detected magnetic resonance (ODMR) spectroscopy, the technique that will be used in this thesis to

characterize the NV centers, is presented in section 2.5. Finally, a short review of NV applications in quantum technologies is reported, with a particular interest in quantum sensing and quantum information science.

2.1 NV physical structure

NV center is a point defect of diamond structure, consisting in a substitutional nitrogen atom in a diamond lattice site having as a nearest neighbor a carbon-vacancy (Fig. 2.1(a)). The NV axis, corresponding to the axis connecting the nitrogen atom and the vacancy, is aligned along the $[111]$ crystallographic direction of diamond lattice. The center has C_{3v} symmetry, with a total of six group elements: two rotation C_3 of $\pm 2\pi/3$ around the NV axis, three reflections σ_v respect to the plane containing the NV axis and one carbon atom and the identity E (Fig. 2.1(b)). The dangling bonds of the three carbon atoms surrounding the vacancy provide three electrons that, together with the two outer-shell electrons of nitrogen, complete the five electrons configuration of the center. This state of the NV, known as NV^0 , is neutral. Spin manipulation of NV^0 is theoretically possible [2,3], but no experimental detection of the ground state ODMR signal has been yet observed. Of much more interest is the negatively charged

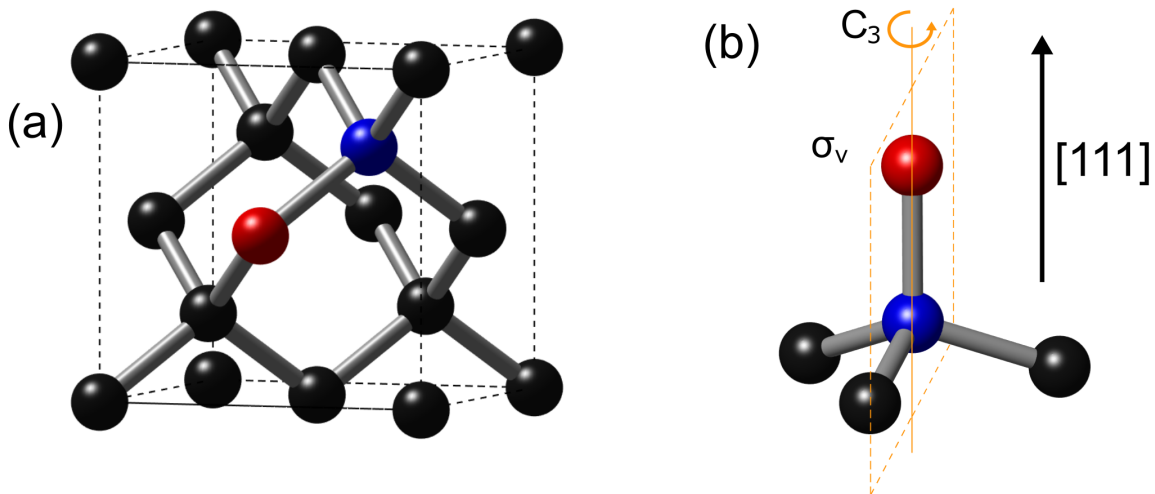


Fig. 2.1: (a) Diamond lattice unit cell with a nitrogen vacancy center, made by a substitutional nitrogen atom (red atom) having a vacancy as nearest neighbor (blue ball). Black atoms represents carbon atoms. (b) Nitrogen vacancy center structure showing the symmetry operations of the C_{3v} group: C_3 rotation of $\pm 2\pi/3$ around the NV axis (aligned along $[111]$ direction of diamond lattice) and σ_v reflection respect to the plane containing the NV axis.

NV^- center, which is formed when the vacancy captures a sixth electrons from the environment. In this configuration the center has two unpaired electrons and a spin $S = 1$ ground state. As a consequence, the NV^- center allows simple manipulation of the ground state sublevels, whose population is sensitive to external fields. For this reason, NV^- centers attracted wide research due to the many potential applications [4, 12], such as in magnetometry [6]. These parts will be detailed in the section dedicated to the spin Hamiltonian and NV applications. From here throughout this thesis, with NV we implicitly refer to is the NV^- center.

2.2 Optical properties

NV center emission spectrum is reported in Fig. 2.2(a). The zero phonon lines (ZPL) of the two NV charge states are clearly visible at 575 nm and 637 nm for, respectively, NV^0 and NV^- centers. The sharp ZPLs means that the NV electronic levels where optical transitions occur are deep inside the diamond band gap [7], far from valence and conduction band. As it can be clearly seen, the emission has a relevant vibronic sideband, caused by NV-phonon coupling, extending to lower energies respect to the ZPL. To understand this behavior, a simple model is used. The ground and excited states are modeled as harmonic oscillators with discrete vibrational states, as shown in Fig. 2.2(b). At room temperature, we can safely assume that most of the NV centers are in the lowest vibrational level of the ground state. Upon laser pumping, electrons from the lower state are excited into the electronic excited state. According to Franck-Condon principle [8], the most probable transition is between the two states having the most overlapping wave functions. In the case of NV^- the final excited states corresponds to 4 vibrational quanta. This shift is related to the significant difference in the nuclear coordinates of the electronic ground and excited state. Moreover, this model simply explain why in usual NV spin manipulation experiments the excitation is not done by using a resonant 637 nm source, but it is performed more efficiently with a 532 nm laser pumping. Once excited, the electrons quickly decay into the lowest vibrational state and then radiatively return in the ground state, in any of the vibrational states. Photon side band (PSB) emission extending till 800 nm is the sum of all the decay transitions to different electronic ground vibrational states.

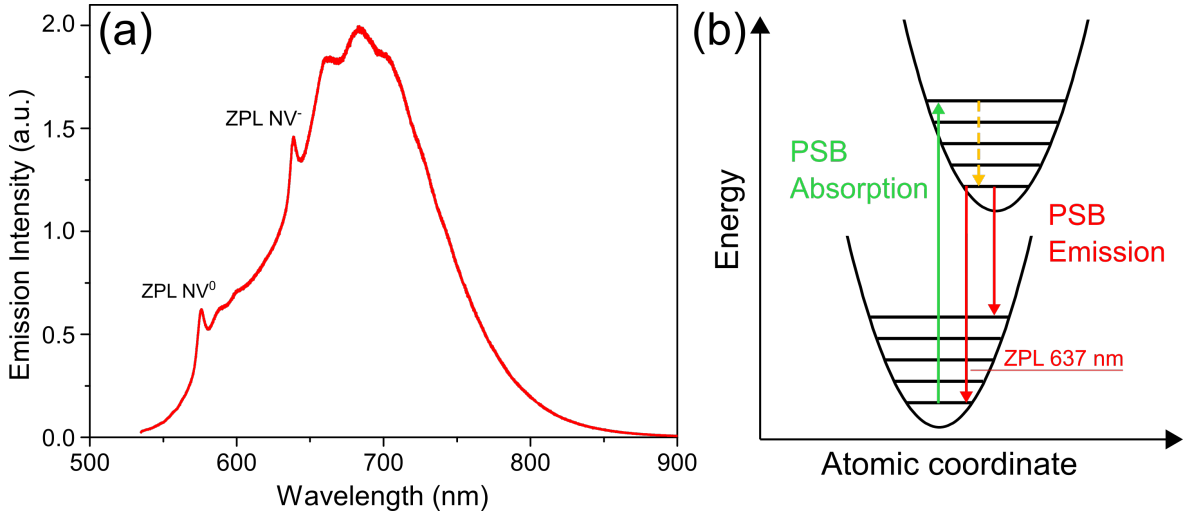


Fig. 2.2: (a) Optical emission spectrum (under 532 nm optical excitation) of nitrogen vacancy center. The ZPLs of NV⁰ and NV⁻ are indicated, respectively, at 575 nm and 637 nm. (b) Harmonic oscillator model for the vibronic levels of the NV⁻ center, highlighting the origin of the phonon side band (PSB) emission observed in panel (a). Non radiative transition is indicated by the dashed yellow line.

2.3 Electronic structure

To fully understand NV spin manipulation and ODMR observation of the ground state and excited states eigenvalues, it is crucial to see how electronic orbitals and spin parts of the NV wave function combine. Here, only a brief review is reported, since a thorough discussion of NV electronic properties is not the scope of this chapter. More detailed analysis can be found in literature [9]. Firstly, we start from building the electronic structure diagram. NV⁻ center has four atomic orbitals: one is the sp³ hybridized nitrogen orbital σ_N , while the other three σ_i ($i = 1, 2, 3$) are the sp³ orbitals of the three carbon atoms (Fig. 2.3(a)). By applying linear combination of the atomic orbitals, through projection operator, and imposing that the resulting combinations transform according to C_{3v} group, the NV molecular orbitals are:

$$a_1 = \beta \frac{\sigma_1 + \sigma_2 + \sigma_3}{3} + \alpha \sigma_N \quad a'_1 = \alpha \frac{\sigma_1 + \sigma_2 + \sigma_3}{3} + \beta \sigma_N \quad (2.1a)$$

$$e_x = \frac{2\sigma_1 + \sigma_2 + \sigma_3}{\sqrt{6}} \quad e_y = \frac{\sigma_2 - \sigma_3}{\sqrt{2}} \quad (2.1b)$$

where the parameters α and β are related to Coulomb interaction energy between electrons [9]. These four levels are filled with 6 electrons following Pauli principle

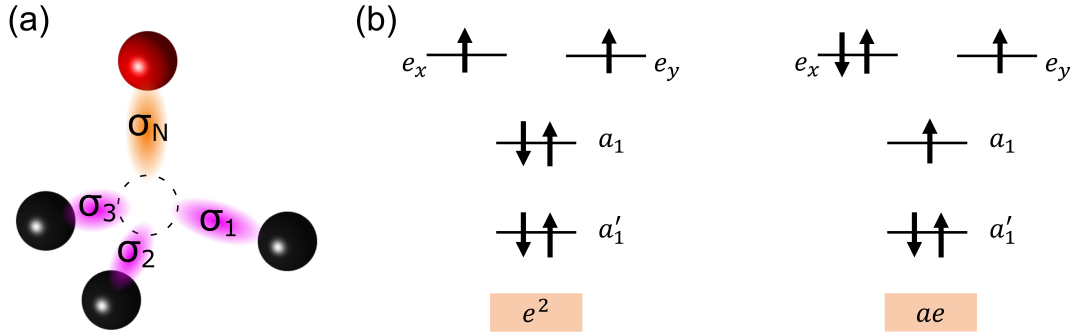


Fig. 2.3: (a) Atomic orbitals whose combinations brings to molecular orbital of the NV⁻ center. The carbon atoms surrounding the vacancy contributes with the three orbitals σ_i ($i = 1, 2, 3$), while σ_N is the orbital of the substitutional nitrogen. All 4 orbitals are sp^3 hybridized. (b) NV ground state electronic configuration, labeled as e^2 . (c) First-excited electronic configuration ae .

and Hund's rules, the latter stating that the electron configuration maximizing spin multiplicity is the most stable one. The two lowest energetic molecular orbitals, a'_1 and a_1 , are filled with two electrons each. The remaining two electrons must be in the e_x and e_y orbitals: to satisfy Hund's rule, spin must be maximized, thus a triplet state with $S = 1$ is formed. The ground state configuration, labeled as e^2 , is represented in Fig. 2.3(b), with the first-excited configuration ae in Fig. 2.3(c). To obtain the total electronic wave function, combinations of the orbital states with the spin states are built, with appropriate symmetric constraint. The complete NV electronic wave functions are reported in Table 2.1. The labels A and E come from group theory, and are related to how the state transform under the symmetric operation of C_{3v} group (A and E represent C_{3v} irreducible representations), whereas the apex indicates the spin levels state, singlet or triplet. For instance, the ground state is a spin triplet (symmetric) with an antisymmetric orbital wave function A_2 , thus the notation is 3A_2 . The excited state 3E is more complicated, with a total of six states. An important feature are the singlet states. Despite they cannot be reached through electrical dipole transitions - that are spin conserving - from the ground state, those levels are linked to the excited states through non-radiative transitions. As we will see in details later in this chapter, this process allows ODMR measurements.

Configuration	State	State label	m_s
$e^2(T)$	$ e_x e_y - e_y e_x\rangle \otimes \uparrow\uparrow\rangle$	3A_2	+1
	$ e_x e_y - e_y e_x\rangle \otimes \downarrow\downarrow\rangle$		-1
	$ e_x e_y - e_y e_x\rangle \otimes \uparrow\downarrow + \downarrow\uparrow\rangle$		0
$e^2(S)$	$ e_x e_x - e_y e_y\rangle \otimes \uparrow\downarrow - \downarrow\uparrow\rangle$	} 1E	0
	$ e_x e_y + e_y e_x\rangle \otimes \uparrow\downarrow - \downarrow\uparrow\rangle$		0
	$ e_x e_x - e_y e_y\rangle \otimes \uparrow\downarrow - \downarrow\uparrow\rangle$	1A_1	0
$ae(T)$	$ a_1 e_x\rangle \otimes \uparrow\uparrow\rangle$	3E	+1
	$ a_1 e_x\rangle \otimes \downarrow\downarrow\rangle$		-1
	$ a_1 e_y\rangle \otimes \uparrow\uparrow\rangle$		+1
	$ a_1 e_y\rangle \otimes \downarrow\downarrow\rangle$		-1
	$ a_1 e_x + e_x a_1\rangle \otimes \uparrow\downarrow + \downarrow\uparrow\rangle$		0
	$ a_1 e_y + e_y a_1\rangle \otimes \uparrow\downarrow + \downarrow\uparrow\rangle$		0
$ae(S)$	$ a_1 e_x + e_x a_1\rangle \otimes \uparrow\downarrow + \downarrow\uparrow\rangle$	1E	0
	$ a_1 e_y + e_y a_1\rangle \otimes \uparrow\downarrow + \downarrow\uparrow\rangle$		0

Table 2.1: NV ground e^2 and excited ae states wave functions, obtained by combining electronic configuration and spin state. The T and S labels in the first column indicate the triplet or singlet state. The state label comes from group theory. The last column gives the spin-projection along the NV axis of the state total spin. This table is adapted from [9]. The wave functions here are expressed in the hole notation. To completely fill the electrons shell two electrons are needed: instead of considering the NV as a 6 electrons system, it is convenient to use a two-holes model. The result obtained through the holes notation is completely equivalent to the electrons notation outcome.

2.4 NV ground state spin Hamiltonian

In this section, the Hamiltonian of the ground state 3A_2 will be described. The interaction of the NV spin states with external perturbations - magnetic/electric fields, temperature, strain - will be studied, in order to understand how the spin state degeneracy is removed, and how this can be used to measure those environmental parameters. From here, it will be evident why NV centers have been proposed as a tool for quantum sensing. The basic form for the Hamiltonian of the ground state is [10]:

$$H_{GS} = H_{SS} + H_{SO} \quad (2.2)$$

where H_{SS} is the spin-spin interaction and H_{SO} is the spin-orbit term. The term describing external perturbations will be described case by case in this chapter. Since this introduction has the aim to give the theoretical background of the experimental observations, we are neglecting additional terms, such as the hyperfine structure [11] arising from the interaction between NV electrons and nuclear spins of surrounding ${}^{14}\text{N}$ or ${}^{13}\text{C}$. All the described terms are normalized by the Planck constant h , to express the Hamiltonian in frequency units.

Spin-spin interaction

This term arises from the dipolar coupling between the two unpaired electrons of the NV ground state. The interaction between the two magnetic dipole moments is given by [12]:

$$H_{SS} = \frac{\mu_0}{4\pi} g^2 \mu_B^2 \left(\frac{\hat{S}_1 \cdot \hat{S}_2}{r^3} - \frac{3(\hat{S}_1 \cdot \hat{r})(\hat{S}_2 \cdot \hat{r})}{r^5} \right) \quad (2.3)$$

where μ_0 , μ_B and g are respectively vacuum permeability, Bohr magneton and the electron g-factor $g = 2.003$. \hat{r} is the distance between the two electrons, while \hat{S}_1 and \hat{S}_2 are the associated spin operators. This equation can be written into a matrix form:

$$H_{SS} = \frac{\mu_0}{4\pi} g^2 \mu_B^2 (S_{1x} \ S_{1y} \ S_{1z}) \begin{pmatrix} \frac{r^2-3x^2}{r^5} & \frac{-3xy}{r^5} & \frac{-3xz}{r^5} \\ \frac{-3xy}{r^5} & \frac{r^2-3y^2}{r^5} & \frac{-3yz}{r^5} \\ \frac{-3xz}{r^5} & \frac{-3yz}{r^5} & \frac{r^2-3z^2}{r^5} \end{pmatrix} \begin{pmatrix} S_{1x} \\ S_{1y} \\ S_{1z} \end{pmatrix} \quad (2.4a)$$

$$H_{SS} = \hat{S}_1 \cdot \hat{D} \cdot \hat{S}_2 \quad (2.4b)$$

By defining $\hat{S} = \hat{S}_1 + \hat{S}_2$, one can easily notice that $\hat{S} \cdot \hat{D} \cdot \hat{S} = 2\hat{S}_1 \cdot \hat{D} \cdot \hat{S}_2$, allowing to

reduce the term to the simple formula:

$$H_{SS} = \hat{S} \cdot \hat{D} \cdot \hat{S} \quad (2.5)$$

with \hat{D} being

$$\hat{D} = \frac{\mu_0}{8\pi} g^2 \mu_B^2 \left(\frac{r^2 \delta_{\alpha\beta} - 3\alpha\beta}{r^5} \right) \quad \alpha, \beta = x, y, z \quad (2.6)$$

Here, \hat{D} is a symmetric matrix with zero trace: for the spectral theorem \hat{D} can be written in a diagonal traceless form. H_{SS} can be written as:

$$H_{SS} = D_x S_x^2 + D_y S_y^2 + D_z S_z^2 \quad (2.7)$$

where D_x , D_y and D_z are the diagonal term of \hat{D} , with $D_x + D_y + D_z = 0$. It is convenient to work in the basis

$$|0\rangle = \begin{pmatrix} 0 \\ 1 \\ 0 \end{pmatrix} \quad |-1\rangle = \begin{pmatrix} 0 \\ 0 \\ 1 \end{pmatrix} \quad |+1\rangle = \begin{pmatrix} 1 \\ 0 \\ 0 \end{pmatrix} \quad (2.8)$$

where the spin operators are represented by the Pauli matrices for $S = 1$

$$S_x = \frac{1}{\sqrt{2}} \begin{pmatrix} 0 & 1 & 0 \\ 1 & 0 & 1 \\ 0 & 1 & 0 \end{pmatrix} \quad S_y = \frac{1}{\sqrt{2}} \begin{pmatrix} 0 & -i & 0 \\ i & 0 & -i \\ 0 & i & 0 \end{pmatrix} \quad S_z = \begin{pmatrix} 1 & 0 & 0 \\ 0 & 0 & 0 \\ 0 & 0 & -1 \end{pmatrix} \quad (2.9)$$

Putting 2.9 in 2.7 brings to:

$$H_{SS} = \frac{3}{2} D_z \left(S_z^2 - \frac{\hat{S}^2}{3} \right) + \frac{D_x - D_y}{2} (S_x^2 - S_y^2) \quad (2.10)$$

by defining $D_{gs} = \frac{3}{2} D_z$ and $E = \frac{D_x - D_y}{2}$, we obtain the final form of the spin-spin interaction:

$$H_{SS} = D_{gs} \left(S_z^2 - \frac{\hat{S}^2}{3} \right) + E (S_x^2 - S_y^2) \quad (2.11)$$

The effect of the spin-spin interaction is to remove the degeneracy between the $m_s = 0$ and the $m_s = \pm 1$ spin sublevels of the ground state through the longitudinal zero-field splitting $D_{gs} = 2.87$ GHz. The parameter E , also called transverse zero-field splitting, depends on the local strain acting on the diamond matrix hosting the NV center, so it is

sample dependent. Values for E ranges from ~ 100 KHz for CVD-grown diamonds [13], to a few MHz for nanodiamonds [14].

Spin-orbit interaction

The spin-orbit interaction term is:

$$H_{SO} = L \cdot S \lambda_z L_z S_z + \lambda_{\perp} (L_x S_x + L_y S_y) \quad (2.12)$$

where $\lambda_z = 5.5$ MHz and $\lambda_{\perp} = 7.3$ MHz are the axial and non-axial strength of the spin orbit interaction [9] (the z axis being the NV axis). The spin-orbit interaction has two consequences. Firstly, it removes the degeneracy of the non-zero spin states. However, this effect is negligible since the corrections of the ground state Hamiltonian eigenvalues are in the second-order [15]. The second effect is more relevant. The term λ_z links states with $m_s = 0$ with other states in the same electronic configuration and spin-projection. The non-axial λ_{\perp} instead term can be rewritten using the ladder operators as $\lambda_{\perp} (L_+ S_- + L_- S_+)$. From this form is evident that this term connects states with $m_s = \pm 1$ to singlet having $m_s = 0$, but in different electronic configurations because of L_+ and L_- operators. The mixing of these states through non-conserving spin transitions achieved by spin-orbit coupling is a key property of NV^- centers, allowing spin-read out and initialization. This aspect will be detailed in the chapter regarding ODMR.

Now we move to the description of the interactions between the NV center with external perturbations.

Magnetic field - Zeeman splitting

When an external magnetic field is applied to the NV center, an additional term is added to the ground state Hamiltonian, describing Zeeman interaction

$$H_Z = \gamma \vec{B} \cdot \vec{S} \quad (2.13)$$

where $\gamma = 2.8$ MHz G^{-1} is the NV gyromagnetic ratio. The total Hamiltonian (neglecting spin-orbit) becomes:

$$H_{NV} = D_{gs} \left(S_z^2 - \frac{\hat{S}^2}{3} \right) + E(S_x^2 - S_y^2) + g\mu_B \vec{B} \cdot \vec{S} \quad (2.14)$$

Using again Pauli matrices for $S = 1$ in the basis $|0\rangle, |+\rangle, |-\rangle$ the Hamiltonian in matrix form is:

$$H_{NV} = \begin{pmatrix} D_{gs} + \gamma B_z & 0 & E \\ 0 & 0 & 0 \\ E & 0 & D_{gs} - \gamma B_z \end{pmatrix} \quad (2.15)$$

Where only the component of the magnetic field parallel to the NV axis is considered. After matrix diagonalization one can find the eigenvalues ν_{\pm} for the Hamiltonian eigenstates $|+\rangle$ and $|-\rangle$:

$$\nu_{\pm} = D_{gs} \pm \sqrt{(\gamma B_z)^2 + E^2} \quad (2.16)$$

While external magnetic field does not modify the state with $m_s = 0$, it removes the degeneracy of the $m_s = \pm 1$ states. The situation is depicted in Fig. 2.4(b). For this particular reason NV centers were proposed as magnetometer, since the eigenvalues of the Hamiltonian can be measured experimentally through ODMR, thus leading to a measure of the applied magnetic field. Only the parallel component of the magnetic field is considered: if the transverse component B_{\perp} are taken into account as a small perturbation of the Hamiltonian, the corrections are in the form $\gamma^2 B_{\perp}^2 / D$ [16]. In usual experiments $D \gg \gamma B_{\perp}$, and the corrections (in the < 1 kHz range) are irrelevant. If $B_{\perp} \gg B_z$, the electron spin states are mixed, and the $m_s = 0$ and $m_s = \pm 1$ are no longer good quantum numbers, making magnetic field measurements more difficult (Eq. 2.16 is not valid). Obviously, since only B_z is considered, NV centers with different orientations respect to the external magnetic field will be subjected to different Zeeman splittings.

Electric/strain fields

The Hamiltonian term describing the interaction of the NV electrons with an external electric field is:

$$H_E = d_{gs}^{\parallel} \varepsilon_z (S_z^2 - \vec{S}^2/3) + d_{gs}^{\perp} \varepsilon_x (S_y^2 - S_x^2) + d_{gs}^{\perp} \varepsilon_y (S_x S_y + S_y S_x) \quad (2.17)$$

where $d_{gs}^{\parallel} = 0.35 \text{ Hz (V/cm)}^{-1}$ and $d_{gs}^{\perp} = 17 \text{ Hz (V/cm)}^{-1}$ are the axial and non-axial electric field coupling constant, while ε_i ($i = x, y, z$) is the electric field component respect to the NV axis (which is parallel to the z axis). Eq. 2.17 is summed to the

spin-spin term of the Hamiltonian (Eq. 2.11), resulting in:

$$H_{NV} = \begin{pmatrix} D_{gs} + d_{gs}^{\parallel} \varepsilon_z & d_{gs}^{\perp} (-\varepsilon_x - i\varepsilon_y) & 0 \\ d_{gs}^{\perp} (-\varepsilon_x + i\varepsilon_y) & 0 & d_{gs}^{\perp} (-\varepsilon_x - i\varepsilon_y) \\ 0 & d_{gs}^{\perp} (-\varepsilon_x + i\varepsilon_y) & D_{gs} + d_{gs}^{\parallel} \varepsilon_z \end{pmatrix} \quad (2.18)$$

where the Hamiltonian is already written in the $m_s = 0$, $m_s = -1$, $m_s = +1$ basis, and supposing $E = 0$ for simplicity. After diagonalization, and defining $\varepsilon_{\perp} = \sqrt{\varepsilon_x^2 + \varepsilon_y^2}$, the new eigenvalues for the $m_s = \pm 1$ level of the ground states are:

$$\nu_{\pm} = D_{gs} + d_{gs}^{\parallel} \varepsilon_z \pm d_{gs}^{\perp} \varepsilon_{\perp} \quad (2.19)$$

The effect of a axial component of the electric field ε_z is to increase the energy separation between $|0\rangle$ and $|\pm\rangle$ by $d_{gs}^{\parallel} \varepsilon_z$, whereas the transverse component ε_{\perp} removes linearly the degeneracy between the $|\pm\rangle$ states, to a total shift of $2d_{gs}^{\perp} \varepsilon_{\perp}$. A strain field in the diamond lattice changes the relative distance between the atoms around the NV center. As a consequence, the local charge environment is different respect to the equilibrium case, thus bringing to a different electric field sensed by the NV electrons. For this reason, the effect of a strain field is treated in the same way of the electric field perturbation. The $|0\rangle$ and $|\pm\rangle$ shift according to Eq. 2.19, but with different coupling constants, that become $d_{gs}^{\parallel} = 5.46$ GHz and $d_{gs}^{\perp} = 19.63$ GHz, and with $\vec{\varepsilon}$ indicating strain field.

Temperature

The effect of temperature fluctuation of the matrix surrounding the NV center is a shift of the zero-field splitting D_{gs} by a factor -78.6 kHz/K [17]. The minus sign indicates that an increase in the temperature brings to a decrease in the zero-field splitting. This effect is related to the crystal lattice expansion [18]

$$\frac{1}{D_{gs}} \frac{dD_{gs}}{dT} = \frac{1}{D_{gs}} \frac{d\langle (r_{12}^2 - 3z_{12}^2)/r_{12}^2 \rangle}{dR} \frac{dR}{dT} \quad (2.20)$$

R is the distance between two carbon atoms in diamond lattice, r_{12} is the displacement between two spins and z_{12} is the component along NV axis of r_{12} .

Pressure

As in the case of temperature, a pressure brings to a linear shift of the ground-state

splitting D_{gs} by a factor 14.58 MHz/GPa [19]. In this case an increase in the pressure leads to an increase of D_{gs} , due to lattice compression. In particular, pressure increases the electronic density in the vacancy site. Another consequence is the shift of the ZPL line emission toward lower wavelength.

2.5 ODMR of NV centers

As we have just seen, NV centers are a powerful tool for sensing different environmental physical parameters. One of the main advantage offered by the NV centers is that this sensing ability is available at room temperature. The reason is that the NV energy levels are buried inside the large diamond band gap (5.5 eV), meaning that an NV can be treated as an isolated system with a localized wavefunction and high spin coherence times [20], without the need of cryogenic condition. In this section, the technique used to experimentally measure the coupling strength between the NV energy levels and the environmental perturbations, namely optically detected magnetic resonance (ODMR), is described. This technique allows to optically read the spin-state of the NV center, and to pump the electrons in a specific spin sublevel. ODMR exploits the spin-dependent fluorescence of the NV^- , caused by inter-system crossing. When the NV center is

Transition	Transition rate (10^6 Hz)
$ 0\rangle_g \rightarrow 0\rangle_e$	77
$ \pm\rangle_g \rightarrow \pm\rangle_e$	77
$ \pm\rangle_e \rightarrow s\rangle$	30
$ 0\rangle_e \rightarrow s\rangle$	0
$ s\rangle \rightarrow 0\rangle_g$	3.3
$ s\rangle \rightarrow \pm\rangle_g$	0

Table 2.2: NV energetic levels transition rate. The subscripts g and e indicate the ground and excited levels. The state $|s\rangle$ is the singlet state. For simplicity the singlets states 1E and 1A_1 are treated as a single one.

excited through laser pumping (usually at 532 nm), the final state must fulfill selection rules for electric dipole operator. For electronic transitions, selection rule are $\Delta l = \pm 1$ and $\Delta m_s = 0$, meaning that the final state is in another electronic configuration but in

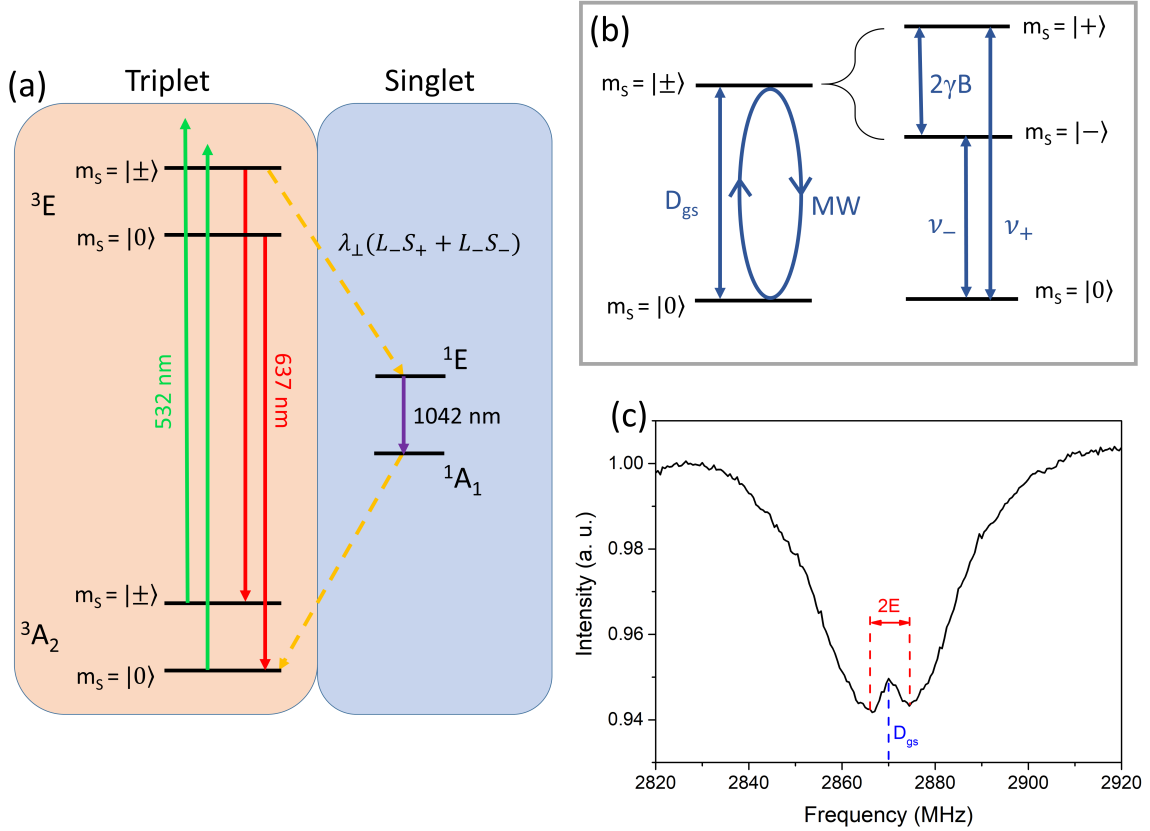


Fig. 2.4: (a) Schematic of the NV⁻ spin energetic levels. Triplet ground 3A_2 and excited state 3E are highlighted by the orange region, while singlet metastable states 1E and 1A_1 in the light blue box. Optical pumping at 532 nm and ZPL relaxation are indicated by the green and red arrows. Non radiative transitions, related to spin orbit interaction, are represented by dashed yellow lines. (b) Detail of the ground state spin sublevels. During ODMR experiments, a MW transition resonant to D_{gs} populates the $m_s = \pm 1$ levels; when the degeneracy is removed, for instance by Zeeman effect $2\gamma B$, two different MW transitions are observed, ν_+ and ν_- . (c) Typical ODMR spectrum for NV⁻ center hosted in 40nm-diameter nanodiamonds. Zero field splitting $D_{gs} = 2.87$ GHz and transverse field splitting are indicated in blue and red respectively.

the same spin state. Thus, from the ground state 3A_2 upon laser pumping the electrons are brought in the 3E level. While NV in the $m_s = 0$ decay only radiatively back to the ground level, NV that are in the state with spin projection $m_s = \pm 1$ have a certain probability to decay non-radiatively to the ground singlet state 1A_1 . From this level then the systems decays in the ground 3A_2 in the sublevel with $m_s = 0$. This inter-system crossing (ISC) is a direct consequence of the spin-orbit interaction ($\lambda_{\perp}(L_+S_- + L_-S_+)$), that mixes the singlet and triplet states in different electronic configuration. All the transitions rates are listed in Table 2.2 and represented in Fig. 2.4(a). ISC has two main consequences. The first one is that NV center can be optically pumped into the ground state $m_s = 0$ level: values of 90% electron population in this level after a few optical cycles has been reported [21]. The possibility to achieve spin polarization simply by optical pumping is a key feature of NV, that has opened many applications in nuclear spin polarization [22, 23] and quantum information science [24]. The second consequence of ISC is the spin-dependent fluorescence. NV emission intensity is highest when most electrons are in the $m_s = 0$ state, so when after pumping only decay through radiative transition is possible. But, when a part of electrons are in the $m_s = \pm 1$ states, some NV will decay trough ISC non-radiatively, resulting in a decrease of fluorescence intensity. The energy split between the sublevels of the ground state is in the microwave region ($D_{gs} = 2.87$ GHz), meaning that spin transitions can be driven by an external microwave field. This is the process, schematized in 2.4(b), over which ODMR is based. Under continuous laser pumping (meaning that the NV are prepared in the $m_s = 0$), a microwave field is applied while measuring the fluorescence intensity. ODMR is obtained by sweeping the microwave frequency: when this frequency matches D_{gs} , the $m_s = \pm 1$ are populated and a decrease in the fluorescence is observed. If the $m_s = \pm 1$ is removed, there will be two distinct microwave frequencies causing fluorescence reduction, one for $m_s = -1$ and one for $m_s = +1$. These two resonances are the eigenvalues of the $m_s = \pm 1$ states, that allows to measure the perturbation that is removing the degeneracy. 2.4(c) finally shows a typical ODMR spectrum, where the reduction of fluorescence is evident at $D_{gs} = 2.87$ GHz, and the strain-related E splitting is also observed.

2.6 NV applications in quantum technology

The motivation that pushed the interest and research on nitrogen-vacancy centers in diamond in the past decade is their potential applications in quantum technologies, mainly quantum sensing and quantum computing. Regarding quantum sensing, NV centers represents an ideal candidate for this particular applications as they present the following key features:

- they can operate in a wide range of temperatures and pressures, as well as in harsh chemical environment;
- they can be brought close to the sample with a nanometric scale precision;
- they show a high sensitivity to magnetic or electric fields.

In recent years, relevant results were obtained with NV centers used as magnetic field sensors. A possible configuration is represented by the use of a thin layer of NV centers a few nanometers below the diamond surface, to form a 2D NV ensemble [25]. Magnetic materials are then deposited on diamond surface to be studied. The main advantage of this configuration is that it allows magnetic field imaging of the sample with a CCD (charge-coupled device) camera [26], where each pixel correspond to a position on the diamond. Magnetic imaging of biological, electronic circuit and superconducting phase transitions have been performed [27], with a demonstrated magnetic sensitivity up to 30 nT Hz^{-1/2} [28]. To perform nanoscale magnetic field sensing, a short separation between the NV centers and the sample is crucial. For this reason, another configuration is represented by a single NV center hosted in a diamond nanocrystal attached to an atomic force microscope (AFM) tip [29]. The sample is then imaged by scanning the tip while monitoring the NV fluorescence, and its dependence on the local magnetic field of the sample. The nanometric size of the diamond (usually < 50 nm) hosting the NV guarantees to obtain a spatial resolution of a few tens of nanometers, due to the proximity of the NV probe to the sample. NV scanning magnetometry was used [30] to study magnetic excitations such as spin waves and static magnetic textures (such as skyrmions or domain walls), as well as static current distributions. Magnetic field sensitivity of 56 nT Hz^{-1/2} has been demonstrated [31]. The same configurations are used to measure electric fields. Initial demonstration reported electric-field sensitivity of 202 ± 6 V cm⁻¹ Hz^{-1/2} [13], that corresponds to an electric field generated by a single electron located ~150 nm away from the NV probe, averaged for one second.

Recently this limit has been improved by three order of magnitude, to reach an electric field sensitivity of $0.1 \text{ V cm}^{-1} \text{ Hz}^{-1/2}$ [32].

Furthermore, the biocompatibility [33] of (nano)diamond structure opens a wide range of possibilities in biological applications of NV centers. First proof-of-principle demonstrations of NV imaging with biological materials have been obtained by tracking the NV fluorescence in human HeLa cells [34] or during the *in vivo* studies performed on the *C. elegans* nematode (roundworm) [35]. These observations confirmed the biological inertness of nanodiamonds and the absence of any stress response or irregularity in cells activity, paving the way to more interesting bio-nanomagnetometry applications. Among the many, two interesting bio-sensing uses of NV are membrane potential measurements [37] and neuronal imaging [36]. The first one require to attach nanodiamonds enriched with NV centers in the membrane of a cell [38], where the membrane potential can be measured. Indeed, in the membrane, having thickness of 5-10 nm, potential of 40-80 mV are present, leading to electric fields in the order of 10^7 V/m , that can be easily detected by ODMR [4]. This should provide a tool to study cell membrane activity to test new drugs or drug delivery mechanisms, that indeed are usually made to target the cell membrane [39]. Another proposed application for NV center is in neuroscience. Neurons can be directly grown on top of a 2D ensemble of NV centers in diamond [40] changes in the magnetic fields due to neurons activity are measured at submillisecond timescale. This system can be scaled-up to large network, and it should allow to get new information on neural network activity on a microsecond timescale resolution. In addition, important results were obtained in nanothermometry with NV centers. As an example [41], temperature variations of 1.8 mK (a sensitivity of $9 \text{ mK Hz}^{1/2}$) with a bulk diamond sample were observed. Moreover, using NV centers in nanodiamonds, the local thermal environment of a human embryonic fibroblast was mapped on a scale of 200 nanometers.

NV centers have also emerged as a strong candidate for quantum information technologies. The reason relies in the fact that this particular color center of diamond meets the two contrasting requirements needed by a quantum information system. On one hand, it has to be well-isolated (such as single trapped ions) and be precisely controlled; on the other hand, the system needs to be scalable, thus favoring solid state systems [42]. NV center matches these two requirements, combining its atom-like properties - well defined optical transitions and quantum states with long coherence

time - with the the robust solid-state host - the diamond structure. Moreover, NV centers provide, also at room temperature, the two quantum mechanical features that are the keys for quantum information science, namely superposition and entanglement. These two properties are not unique to the NV, but the difference with other spin-state systems relies in the NV optical properties. Indeed, as explained previously in this chapter, with a single optical measurements - 532 nm laser pulse - it is possible to prepare the electronic spin in a specific level - $m_s = 0$ - and simultaneously "read" the quantum state of the NV electronic spin. The *qubit* in NV centers is represented by the two electronic spin sublevels $m_s = 0$ and $m_s = +1$ (or $m_s = -1$): superposition between the two qubit states is easily obtained by a resonant MW pulse, leading to the state $\psi = a|0\rangle + b|+\rangle$, with $a^2 + b^2 = 1$. One approach to obtain a quantum register, which is a system made by multiple qubits that are manipulated to perform calculations in a quantum computer, made by a network of NV, is based on magnetic interactions between the electronic spins of the NV centers. The coupling strength due to magnetic dipole-dipole interactions between two NV electronic spins 10 nm from each other was measured to be 43 kHz [43]. With this interaction, entanglement operations between two NV centers was demonstrated [44]. The main progress achieved is that such a device could operate at ambient conditions and room temperature. The main limitation is the coherence lifetime of the superposition state ψ , that gives the time interval in which coherent manipulations (so calculations) between qubits can be performed. As this device is based on magnetic interaction, any other magnetic moment (mainly ^{13}C nuclear spin) in the proximity of the NVs is a source of noise and decoherence. Typical lifetimes are a few microseconds for standard diamond [42] and up to milliseconds for isotopically purified diamonds [45]. An interesting possibility to increase the lifetime is to use the nearby nuclear spin as a resource. As a matter of fact, magnetic interactions between ^{13}C nuclear spin and NV electronic spin allows to store NV information in the nuclear spin sublevels of the nearby ^{13}C . Exploiting the much longer coherence time of nuclear spin, as long as a few seconds [46], long-term quantum memory was demonstrated [47]. Despite NV based quantum information technology exceeded expectations when compared to other systems, such as trapped ions, especially for the room-temperature-operational mode, several challenges remain. For instance, process for deterministic production of NV centers with high spatial control are required, in order to fabricate a quantum network with entangled NV electronic spins having nuclear spin associated quantum memory.

References for chapter 2

- [1] Gruber, A., Drabenstedt, A., Tietz, C., Fleury, L., Wrachtrup, J., & Von Borczyskowski, C. (1997). Scanning confocal optical microscopy and magnetic resonance on single defect centers. *Science*, 276(5321), 2012-2014.
- [2] Felton, S., Edmonds, A. M., Newton, M. E., Martineau, P. M., Fisher, D., & Twitchen, D. J. (2008). Electron paramagnetic resonance studies of the neutral nitrogen vacancy in diamond. *Physical Review B*, 77(8), 081201.
- [3] Gali, A. (2009). Theory of the neutral nitrogen-vacancy center in diamond and its application to the realization of a qubit. *Physical Review B*, 79(23), 235210.
- [4] Schirhagl, R., Chang, K., Loretz, M., & Degen, C. L. (2014). Nitrogen-vacancy centers in diamond: nanoscale sensors for physics and biology. *Annual review of physical chemistry*, 65, 83-105.
- [5] Liu, G. Q., & Pan, X. Y. (2018). Quantum information processing with nitrogen-vacancy centers in diamond. *Chinese Physics B*, 27(2), 020304.
- [6] Rondin, L., Tetienne, J. P., Hingant, T., Roch, J. F., Maletinsky, P., & Jacques, V. (2014). Magnetometry with nitrogen-vacancy defects in diamond. *Reports on progress in physics*, 77(5), 056503.
- [7] Loubser, J. H. N., & Van Wyk, J. A. (1977). Optical spin-polarisation in a triplet state in irradiated and annealed type 1b diamonds. *Diamond Research*, 11-14.
- [8] Condon, E. U. (1928). Nuclear motions associated with electron transitions in diatomic molecules. *Physical Review*, 32(6), 858.
- [9] Maze, J. R., Gali, A., Togan, E., Chu, Y., Trifonov, A., Kaxiras, E., & Lukin, M. D. (2011). Properties of nitrogen-vacancy centers in diamond: the group theoretic approach. *New Journal of Physics*, 13(2), 025025.
- [10] Doherty, M. W., Manson, N. B., Delaney, P., Jelezko, F., Wrachtrup, J., & Hollenberg, L. C. (2013). The nitrogen-vacancy colour centre in diamond. *Physics Reports*, 528(1), 1-45.
- [11] Felton, S., Edmonds, A. M., Newton, M. E., Martineau, P. M., Fisher, D., Twitchen, D. J., & Baker, J. M. (2009). Hyperfine interaction in the ground state of the negatively charged nitrogen vacancy center in diamond. *Physical Review B*, 79(7), 075203.
- [12] Manson, N. B., Harrison, J. P., & Sellars, M. J. (2006). Nitrogen-vacancy center in diamond: Model of the electronic structure and associated dynamics. *Physical Review B*, 74(10), 104303.
- [13] Dolde, F., Fedder, H., Doherty, M. W., Nöbauer, T., Rempp, F., Balasubramanian, G., et al. (2011). Electric-field sensing using single diamond spins. *Nature Physics*, 7(6), 459.

- [14] Laraoui, A., Hodges, J. S., & Meriles, C. A. (2012). Nitrogen-vacancy-assisted magnetometry of paramagnetic centers in an individual diamond nanocrystal. *Nano letters*, 12(7), 3477-3482.
- [15] Lenef, A., & Rand, S. C. (1996). Electronic structure of the N-V center in diamond: Theory. *Physical Review B*, 53(20), 13441.
- [16] Shin, C. S., Avalos, C. E., Butler, M. C., Wang, H. J., Seltzer, S. J., Liu, R. B., et al. (2013). Suppression of electron spin decoherence of the diamond NV center by a transverse magnetic field. *Physical Review B*, 88(16), 161412.
- [17] Acosta, V. M., Bauch, E., Ledbetter, M. P., Waxman, A., Bouchard, L. S., & Budker, D. (2010). Temperature dependence of the nitrogen-vacancy magnetic resonance in diamond. *Physical review letters*, 104(7), 070801.
- [18] Neumann, P., Jakobi, I., Dolde, F., Burk, C., Reuter, R., Waldherr, G., et al. (2013). High-precision nanoscale temperature sensing using single defects in diamond. *Nano letters*, 13(6), 2738-2742.
- [19] Doherty, M. W., Struzhkin, V. V., Simpson, D. A., McGuinness, L. P., Meng, Y., Stacey, A., et al. (2014). Electronic properties and metrology applications of the diamond NV⁻ center under pressure. *Physical review letters*, 112(4), 047601.
- [20] Heremans, F. J., Yale, C. G., & Awschalom, D. D. (2016). Control of spin defects in wide-bandgap semiconductors for quantum technologies. *Proceedings of the IEEE*, 104(10), 2009-2023.
- [21] Waldherr, G., Beck, J., Steiner, M., Neumann, P., Gali, A., Frauenheim, T., et al. (2011). Dark states of single nitrogen-vacancy centers in diamond unraveled by single shot NMR. *Physical review letters*, 106(15), 157601.
- [22] King, J. P., Coles, P. J., & Reimer, J. A. (2010). Optical polarization of C 13 nuclei in diamond through nitrogen vacancy centers. *Physical Review B*, 81(7), 073201.
- [23] Staudacher, T., Shi, F., Pezzagna, S., Meijer, J., Du, J., Meriles, C. A., et al. (2013). Nuclear magnetic resonance spectroscopy on a (5-nanometer) 3 sample volume. *Science*, 339(6119), 561-563.
- [24] Wu, Y., Wang, Y., Qin, X., Rong, X., & Du, J. (2019). A programmable two-qubit solid-state quantum processor under ambient conditions. *npj Quantum Information*, 5(1), 9.
- [25] Pham, L. M., Le Sage, D., Stanwix, P. L., Yeung, T. K., Glenn, D., Trifonov, A., et al. (2011). Magnetic field imaging with nitrogen-vacancy ensembles. *New Journal of Physics*, 13(4), 045021.
- [26] Steinert, S., Dolde, F., Neumann, P., Aird, A., Naydenov, B., Balasubramanian, G., et al. (2010). High sensitivity magnetic imaging using an array of spins in diamond. *Review of scientific instruments*, 81(4), 043705.

BIBLIOGRAPHY

- [27] Acosta, V., & Hemmer, P. (2013). Nitrogen-vacancy centers: physics and applications. *MRS bulletin*, 38(2), 127-130.
- [28] Maze, J. R., Stanwix, P. L., Hodges, J. S., Hong, S., Taylor, J. M., Cappellaro, P., et al. (2008). Nanoscale magnetic sensing with an individual electronic spin in diamond. *Nature*, 455(7213), 644.
- [29] Balasubramanian, G., Chan, I. Y., Kolesov, R., Al-Hmoud, M., Tisler, J., Shin, C., et al. (2008). Nanoscale imaging magnetometry with diamond spins under ambient conditions. *Nature*, 455(7213), 648.
- [30] Casola, F., van der Sar, T., & Yacoby, A. (2018). Probing condensed matter physics with magnetometry based on nitrogen-vacancy centres in diamond. *Nature Reviews Materials*, 3(1), 17088.
- [31] Maletinsky, P., Hong, S., Grinolds, M. S., Hausmann, B., Lukin, M. D., Walsworth, R. L., et al. (2012). A robust scanning diamond sensor for nanoscale imaging with single nitrogen-vacancy centres. *Nature nanotechnology*, 7(5), 320.
- [32] J. Michl et al. Robust and Accurate Electric Field Sensing with Solid State Spin Ensembles, *Nano Lett.* 2019, 19, 4904-4910
- [33] Zhu, Y., Li, J., Li, W., Zhang, Y., Yang, X., Chen, N., et al. (2012). The biocompatibility of nanodiamonds and their application in drug delivery systems. *Theranostics*, 2(3), 302.
- [34] Faklaris, O., Joshi, V., Irinopoulou, T., Tauc, P., Sennour, M., Girard, H., et al. (2009). Photoluminescent diamond nanoparticles for cell labeling: study of the uptake mechanism in mammalian cells. *ACS nano*, 3(12), 3955-3962.
- [35] Mohan, N., Chen, C. S., Hsieh, H. H., Wu, Y. C., & Chang, H. C. (2010). In vivo imaging and toxicity assessments of fluorescent nanodiamonds in *Caenorhabditis elegans*. *Nano letters*, 10(9), 3692-3699.
- [36] Hall, L. T., Beart, G. C. G., Thomas, E. A., Simpson, D. A., McGuinness, L. P., Cole, J. H., et al. (2012). High spatial and temporal resolution wide-field imaging of neuron activity using quantum NV-diamond. *Scientific reports*, 2, 401.
- [37] Hall, L. T., Simpson, D. A., & Hollenberg, L. C. L. (2013). Nanoscale sensing and imaging in biology using the nitrogen-vacancy center in diamond. *Mrs Bulletin*, 38(2), 162-167.
- [38] Kaufmann, S., Simpson, D. A., Hall, L. T., Perunicic, V., Senn, P., Steinert, S., et al. (2013). Detection of atomic spin labels in a lipid bilayer using a single-spin nanodiamond probe. *Proceedings of the National Academy of Sciences*, 110(27), 10894-10898.
- [39] Reimhult, E., & Kumar, K. (2008). Membrane biosensor platforms using nano-and microporous supports. *Trends in biotechnology*, 26(2), 82-89.

- [40] Specht, C. G., Williams, O. A., Jackman, R. B., & Schoepfer, R. (2004). Ordered growth of neurons on diamond. *Biomaterials*, 25(18), 4073-4078.
- [41] Kucsko, G., Maurer, P. C., Yao, N. Y., Kubo, M. I. C. H. A. E. L., Noh, H. J., Lo, P. K., et al. (2013). Nanometre-scale thermometry in a living cell. *Nature*, 500(7460), 54.
- [42] Childress, L., & Hanson, R. (2013). Diamond NV centers for quantum computing and quantum networks. *MRS bulletin*, 38(2), 134-138.
- [43] Neumann, P., Kolesov, R., Naydenov, B., Beck, J., Rempp, F., Steiner, M., et al. (2010). Quantum register based on coupled electron spins in a room-temperature solid. *Nature Physics*, 6(4), 249.
- [44] Dolde, F., Jakobi, I., Naydenov, B., Zhao, N., Pezzagna, S., Trautmann, C., et al. (2013). Room-temperature entanglement between single defect spins in diamond. *Nature Physics*, 9(3), 139.
- [45] Balasubramanian, G., Neumann, P., Twitchen, D., Markham, M., Kolesov, R., Mizuochi, N., et al. (2009). Ultralong spin coherence time in isotopically engineered diamond. *Nature materials*, 8(5), 383.
- [46] Maurer, P. C., Kucsko, G., Latta, C., Jiang, L., Yao, N. Y., Bennett, S. D., et al. (2012). Room-temperature quantum bit memory exceeding one second. *Science*, 336(6086), 1283-1286.
- [47] Jelezko, F., Gaebel, T., Popa, I., Domhan, M., Gruber, A., & Wrachtrup, J. (2004). Observation of coherent oscillation of a single nuclear spin and realization of a two-qubit conditional quantum gate. *Physical Review Letters*, 93(13), 130501.

BIBLIOGRAPHY

Chapter 3

Nanodiamonds properties and synthesis

The first proof of nanodiamonds (NDs) successful production was obtained in 1963 [1] in the USSR, when it was observed that the temperature and pressure in the shock wave induced by an explosion is enough to squeeze the carbon atoms from the residual explosive into diamond nanoparticles. However, this result reached the rest of the world only by the end of the 1980s [2]. From that moment, NDs attracted the interest of scientists for their unique and exceptional properties. Indeed, NDs maintain most of the superior properties of bulk diamond, such as the hardness or the high thermal conductivity, and transfer them at the nanoscale. Moreover, NDs present other unique peculiarities, like biocompatibility [3] and tunable surface structure [4], that allowed this kind of nanoparticle to find many applications in different fields, from tribology [5] to drug delivery [6,7]. NDs properties, with consequential current or possible applications, are reported in the following section 3.1. In the last decades, different synthesis techniques have been developed: the most relevant for commercial productions of NDs are presented in section 3.2. Finally, the particular technique used in this thesis for NDs production, namely pulsed laser ablation, is detailed in section 3.3.

3.1 Nanodiamond properties and applications

NDs are diamond nanoparticles having dimension in the nanometer range ($< 1 \mu\text{m}$). As for bulk diamond, carbon atoms in NDs are sp^3 hybridized and organized in a

tetrahedral structure. Each carbon atoms have four nearest neighbors, forming bond angles of 109.5° to minimize orbitals repulsion. The carbon atoms in diamond structure are linked with strong covalent $C - C$ bonds (711 kJ/mol [8]), resulting in a short distance between two atoms of 1.53 \AA [9]. This brings to the highest density observed in solids of $1.76 \cdot 10^{23} \text{ atoms cm}^{-3}$ [10], responsible for the unique mechanical properties of diamond, such as the extreme hardness and incompressibility. The interest in NDs arises both from the inheritance of the bulk diamond superior properties, combined with the peculiarities of this particular nanoparticle. NDs main features are the resistance to harsh environment, the biocompatibility and a relative ease in surface functionalization. The latter is directly related to the carbon sp^3 hybridization: atoms at the surface sites are lacking one of the four bonds of diamond structure. For this reason NDs surface are highly reactive, and termination with many different functional groups was demonstrated (as shown in Fig. 3.1). The possibility of having many properties in a single nanoparticles made NDs interesting for a wide range of applications.

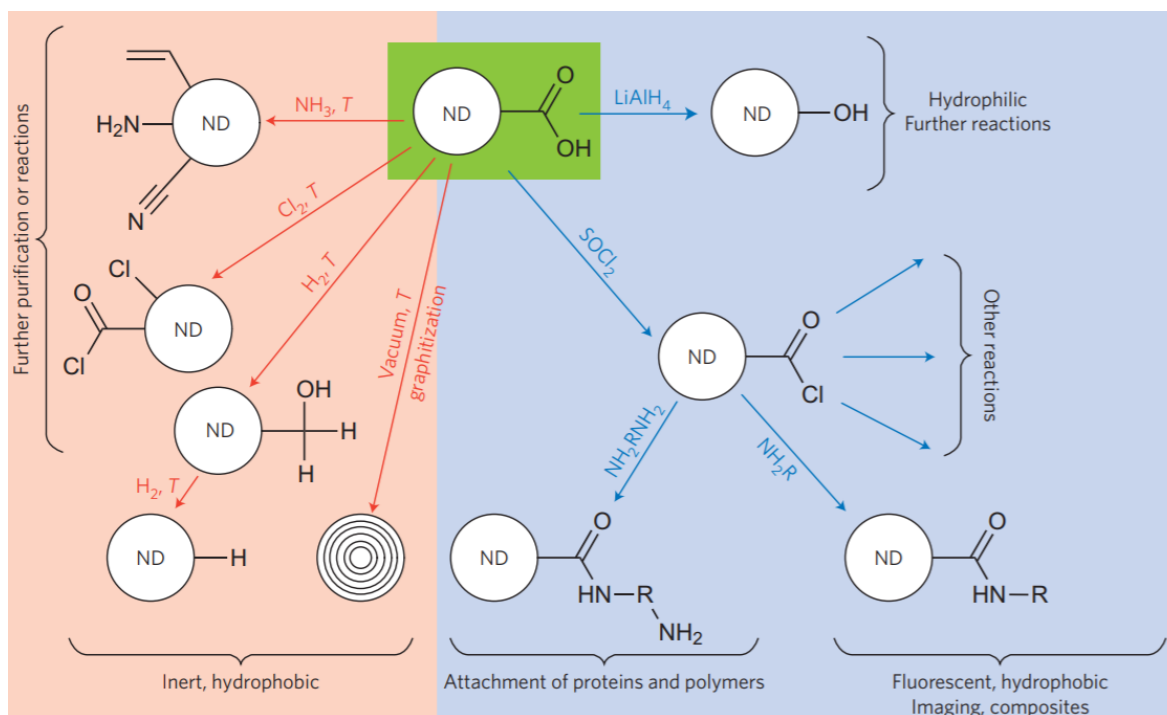


Fig. 3.1: Surface modification of NDs surface structure. The usual standard material (green box) are NDs terminated with carboxylic groups (COOH). This termination is obtained through air oxidation or HCl washing of the synthesized NDs. The red region of the picture represents surface modification through high temperature gas treatments, whereas the blue part gives the room-temperature wet chemistry functionalization processes. Reproduced from [14].

Tribology

The most known property of NDs is the extreme hardness, so they have been used in tribology for a long time [11]. NDs are useful for polishing applications, due to the small size. As an example [12], NDs with average size of 55 nm were used to polish glass ceramics with a final surface roughness of 0.208 nm. After synthesis, NDs are usually made by a diamond core with the surface layers being in graphite phase [14]. This unique feature was exploited for lubrication [13]: surface graphite acts as lubrication agent, while the incompressible diamond core reduces friction by smoothing the surface roughness. The rich surface chemistry of NDs means that the nanoparticles can be made hydrophilic or hydrophobic, allowing dispersion in different system, such as water or oil [15].

Nanocomposites

The thermal properties of NDs (high thermal conductivity of $2200 \text{ W m}^{-1} \text{ K}^{-1}$), combined with mechanical properties and versatile surface chemistry, made NDs a valuable filler for composites material. Proof of improvements in mechanical strength [16], thermal conductivity [17], wear resistance [18] and electromagnetic shielding [19] of polymers with NDs dispersed in their matrix was demonstrated. This nanocomposite materials are useful for biomedical applications, given diamond phase biocompatibility, in particular for the reinforcement of polymers used as scaffolds for tissue engineering [20]. An example of NDs-polymer composite is the ND-ODA-PLLA [21], that is studied for biomedical application as multifunctional bone scaffold materials. It is obtained by dispersion of octadecylamine-functionalized nanodiamond (ND-ODA) in PLLA polymer. An increase of one order of magnitude respect to pure PLLA was observed, together with a Young's modulus value close to the one of human cortical bone.

Fluorescence imaging

The fluorescence in NDs is provided by the presence of color centers in diamond structure. Anyways, the most studied one for applications is the nitrogen-vacancy (NV) centers. Quantum properties of NV centers combined with NDs biocompatibility, chemical stability, non toxicity and versatile surface structure, made fluorescent NDs perfect candidate for bioimaging [22]. Indeed, fluorescent NDs provides a tool allowing good sensitivity together with a resolution in the nanometer scale. Moreover, biocompatibility of diamond phase allows *in vivo* imaging [22, 23]. Quantum sensing with fluorescent

NDs has been already demonstrated in magnetometry [24] and nanothermometry [25]. A detailed description of NV centers properties and applications is given in the previous chapter.

Drug delivery

Another class of biomedical applications in which NDs are starting to play an important role is drug delivery. NDs possess all the specific properties that a system for drug delivery requires: biocompatibility, scalability, dispersability in water and a tunable surface structure to have the ability of carrying a wide range of therapeutics. The combination of such properties with imaging (provided by NV centers) makes NDs an excellent platform for drug delivery. Initial studies were performed with delivery of doxorubicin [26] (used for the treatment of various cancers), to treat drug-resistant breast and liver cancer. The efficiency and safety of this NDs-doxorubicin complex was proved in mice [27]. Many other combinations have been tested, all for potential use as injectable therapeutics. Furthermore, a different system made by a film of parylene-NDs composite was used to a steady drug release over a two days to one month period [28].

3.2 Synthesis techniques

It is well known that the stable allotrope of carbon at ambient pressure and room temperature is graphite. As it can be seen in the carbon phase diagram of Fig. 3.2, diamond requires extreme conditions of temperature and pressure to be formed. For instance, natural diamond formed in the Earth mantle, 140 – 200 km below Earth surface [29], where the temperature and pressure are in the range of 900 – 1400 °C and 4.5 – 6 GPa [30]. Once diamond phase is formed, the transition back to graphite at ambient condition is avoided by the high energy barrier between the two phases. Indeed, even if graphite is thermodynamically favored (energy difference of 0.02 eV per atom between diamond and graphite), the two phases are separated by a 0.4 eV per atom energy barrier, due to the strong covalent sp^3 bonds between the carbon atoms. This makes diamond a metastable phase, as it is thermodynamically unstable but kinetically stable. Nowadays, many different methods for artificial synthesis of NDs are available [14]. In the following, the three main techniques commercially available are described: detonation, chemical vapor deposition (CVD) and milling of high-pressure-high-temperature (HPHT) micro-sized diamonds. Finally, the standard technique used

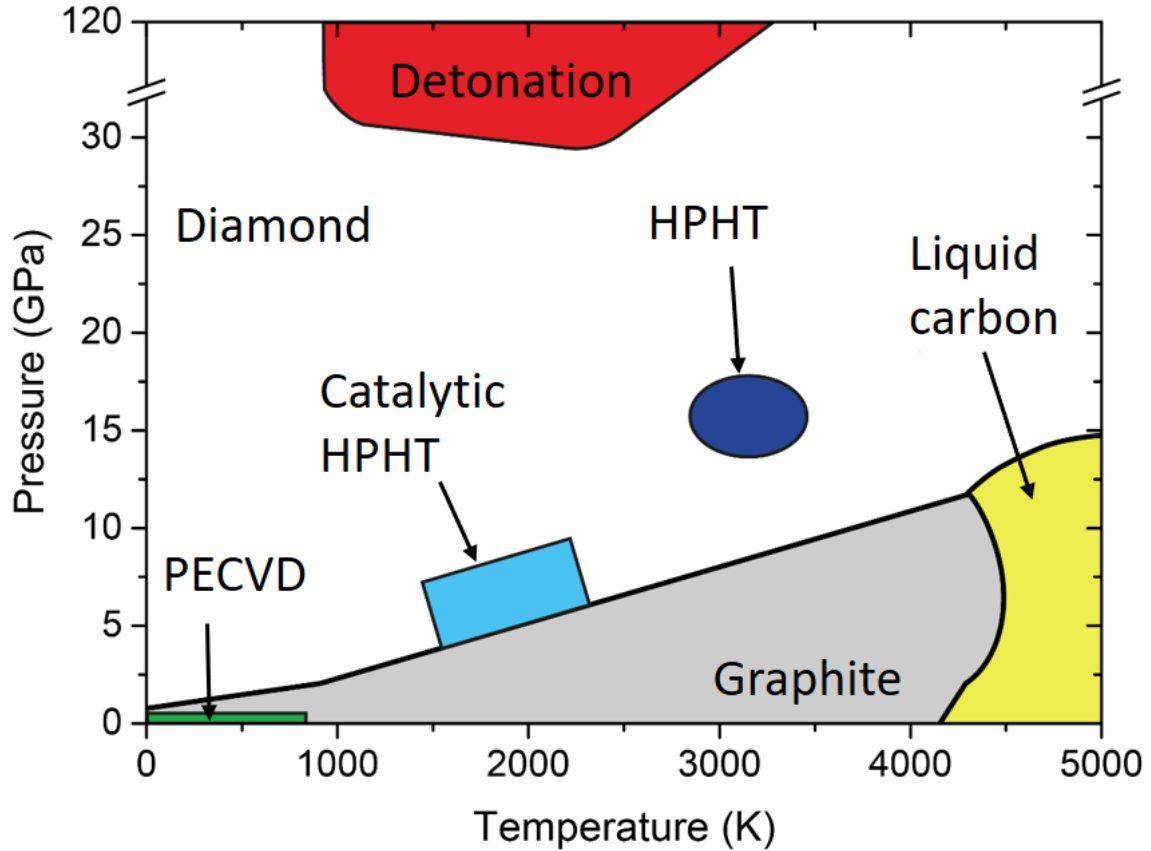


Fig. 3.2: Carbon phase diagram. The regions where the stable form of carbon are graphite, diamond and liquid carbon are labeled by the grey, white and yellow colors respectively. In addition, thermodynamic conditions reached during the different synthesis technique are indicated.

for the production of NV-centers containing NDs is reported.

Detonation synthesis

During detonation synthesis, the energy of an explosion is used to drive diamond phase formation [31]. In a closed metallic chamber explosives with a negative oxygen balance are detonated: usually a mixture of 60% TNT ($C_6H_2(NO_2)CH_3$) and 40% hexogen ($C_3H_6N_6O_6$) is employed (Fig. 3.3) [14]. The carbon atoms that eventually form the NDs are provided by the molecules of the explosives or either by precursor graphite put inside the detonation chamber. The synthesis is called "dry" or "wet" when the chamber is filled with an inter gas (N_2 , argon, CO_2) or with water (ice), that act as a coolant. The cooling media plays an important role in the carbon yield, which is usually between 4-10% of the explosive weight [13]. The process leading to NDs

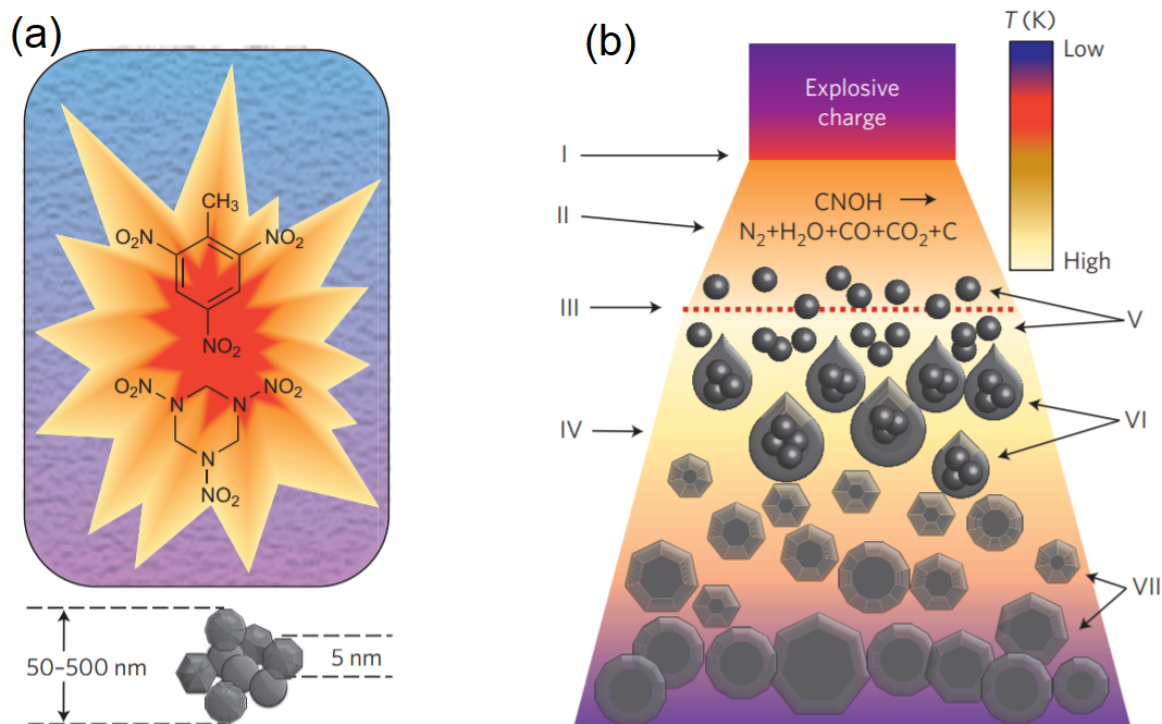


Fig. 3.3: (a) Detonation process. A mixture of 60% TNT ($C_6H_2(NO_2)_3CH_3$) and 40% hexogen ($C_3H_6N_6O_6$) is detonated inside a metallic chamber filled either with water or ice or with an atmosphere of N_2 , argon or CO_2 . 4 – 5 nm sized NDs agglomerated in sub-micrometer clusters are obtained. (b) Schematics of NDs synthesis upon shock wave propagation. The detonation (I) brings to chemical dissociation of the carbon precursor (II) that can be the explosive molecules or graphite. The dashed line (III) represents the region where pressure required to form diamond phase is reached. The detonation products expand (IV) and the carbon atoms condense and crystallize (V) to form nanoclusters (VI). Finally NDs crystallize starting from carbon nanoclusters, grow and agglomerate (VII). Reproduced from Ref. [14]

formation is schematized in Fig. 3.3. After detonation, the carbon atoms released during explosive molecules dissociation condense and crystallize into nanoclusters [32]. The thermodynamic condition (Fig. 3.2) reached in the chamber during the detonation-induced increase in the pressure leads to crystallization of the carbon nanoclusters into diamond phase. Finally, the formed NDs grow and agglomerate, resulting in NDs with size of 4 – 5 nm. The main drawback of this technique is that the resulting sample, called detonation soot, must be purified to remove contaminants. Indeed, detonation soot is not only made of diamond phase, but also of non-diamond carbon (25 – 85 wt%) and metals coming from the wall of the chamber (1 – 8 wt%) [33]. To remove the impurities, cleaning of the detonation soot in a strong acid environment (usually

a mixture of $\text{HNO}_3/\text{H}_2\text{SO}_4/\text{HClO}_4$) is required [31], with a dangerous and expensive process. Another problem is NDs agglomeration occurring during synthesis, where NDs clusters reaching the several hundreds of nanometers are obtained. To isolate the single 4 – 5 nm sized NDs, milling with ceramic microbeads (that introduces contaminants) or ultrasonic disintegration are the standard de-aggregation methods [34].

Chemical vapor deposition (CVD)

Chemical vapor deposition is one of the most popular method for the deposition of thin film, and it has been used for the synthesis of nanocrystalline diamond film [35]. In details, the deposition of carbon atoms occurs during decomposition of a gas mixture with a carbon containing species, usually methane CH_4 , in excess of hydrogen. The gas phase is decomposed by using a hot filament or a microwave plasma, to form radicals such as H^\bullet and CH_3^\bullet , that are essential for diamond growth. The NDs film form on a substrate, typically a silicon wafer, coated with a micrometer sized diamond powder acting as a seed for NDs nucleation [35], that finally grow to form a continuous film. The typical set-up [36] for CVD synthesis is reported in Fig. 3.4(a). The size

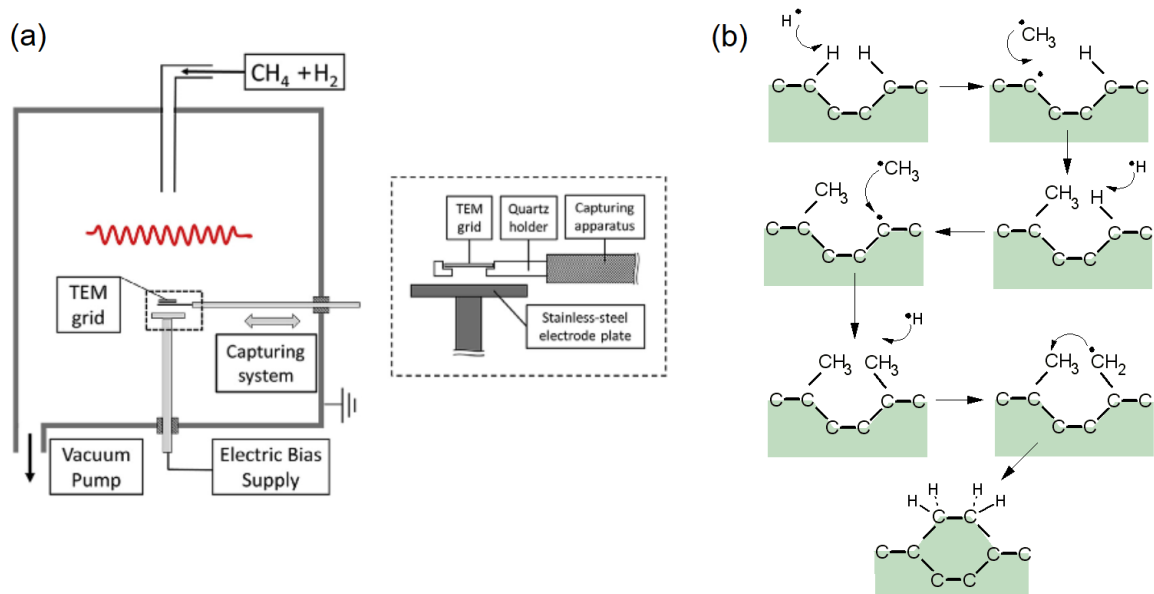


Fig. 3.4: (a) Experimental setup for CVD synthesis. The hot filament is required to dissociate the gas phase (CH_4/H_2 mixture) into radicals, whereas the electrode plate is used to attract those radicals (mainly H^\bullet and CH_3^\bullet) toward the substrate. Reproduced from Ref. [36] (b) Nanocrystalline diamond film growth mechanism during CVD synthesis. Reproduced from Ref. [37].

of the grain composing the film ranges to tens of micron down to a few nanometers, depending on CH_4/H_2 relative concentration [37]. Small concentration of CH_4 brings to microcrystalline diamonds, whereas a high value of CH_4/H_2 ratio decreases grain size, that becomes in the order of tens of nanometers for 1 – 5% CH_4/H_2 . The diamond growth mechanism [37] is schematized in Fig. 3.4(b). Carbon atoms at the surface of diamond seeds are left with dangling bonds after hydrogen abstraction by H^\bullet radicals. These bonds are then filled by CH_3^\bullet molecules: when this process takes place in two adjacent sites, the new carbons can bond together, and finally be locked into the diamond lattice.

Milling of high-pressure-high-temperature (HPHT) microdiamonds

HPHT synthesis technique resembles the natural process of diamond formation, where a carbon precursor, usually graphite, is brought to a state of high pressure and high temperature. Inside a chamber, the temperature is brought to $\sim 2000^\circ\text{C}$ and a set of anvils increase the pressure up to several GPa [38]. This technique allows the formation of bulk or microdiamonds, that required to be milled to obtain NDs [39]. The milling process does not allow a good control in nanoparticle size and shape [40], so additional processes are required. For instance, acid treatment to remove the contaminants coming from the milling process or centrifugation and filtration to isolate NDs with narrower size distribution.

Synthesis of NV-centers enriched NDs

Recently, reports on direct synthesis of fluorescent NDs through detonation synthesis of nitrogen-doped carbon precursors have been reported [41]. Despite that, the standard way to commercially produce NV-centers enriched NDs is a complex, multi-step and expensive process. Synthetic HPHT diamonds typically contain 100 ppm of nitrogen atoms as an impurity in the diamond structure [42]. To form NV centers starting from these atoms, vacancies are created in the lattice by high-energy particle irradiation (electrons, protons, He^+) followed by an vacuum annealing at $700 - 1000^\circ\text{C}$ [43]. The role of the annealing is to increase the mobility of the nitrogen atoms inside the lattice, that are then trapped by the carbon vacancies to form NVs. One could directly irradiate NDs to increase the NV-fluorescence, but it has been proven by density functional theory [44] and Monte Carlo simulations [45], that NV concentration increase non-linearly with crystal size. In particular, the probability of forming NV centers in 5 nm sized NDs is 4.5 and 25 times lower compared to 20 and 55 nm NDs [45]. Thus, it is more efficient to

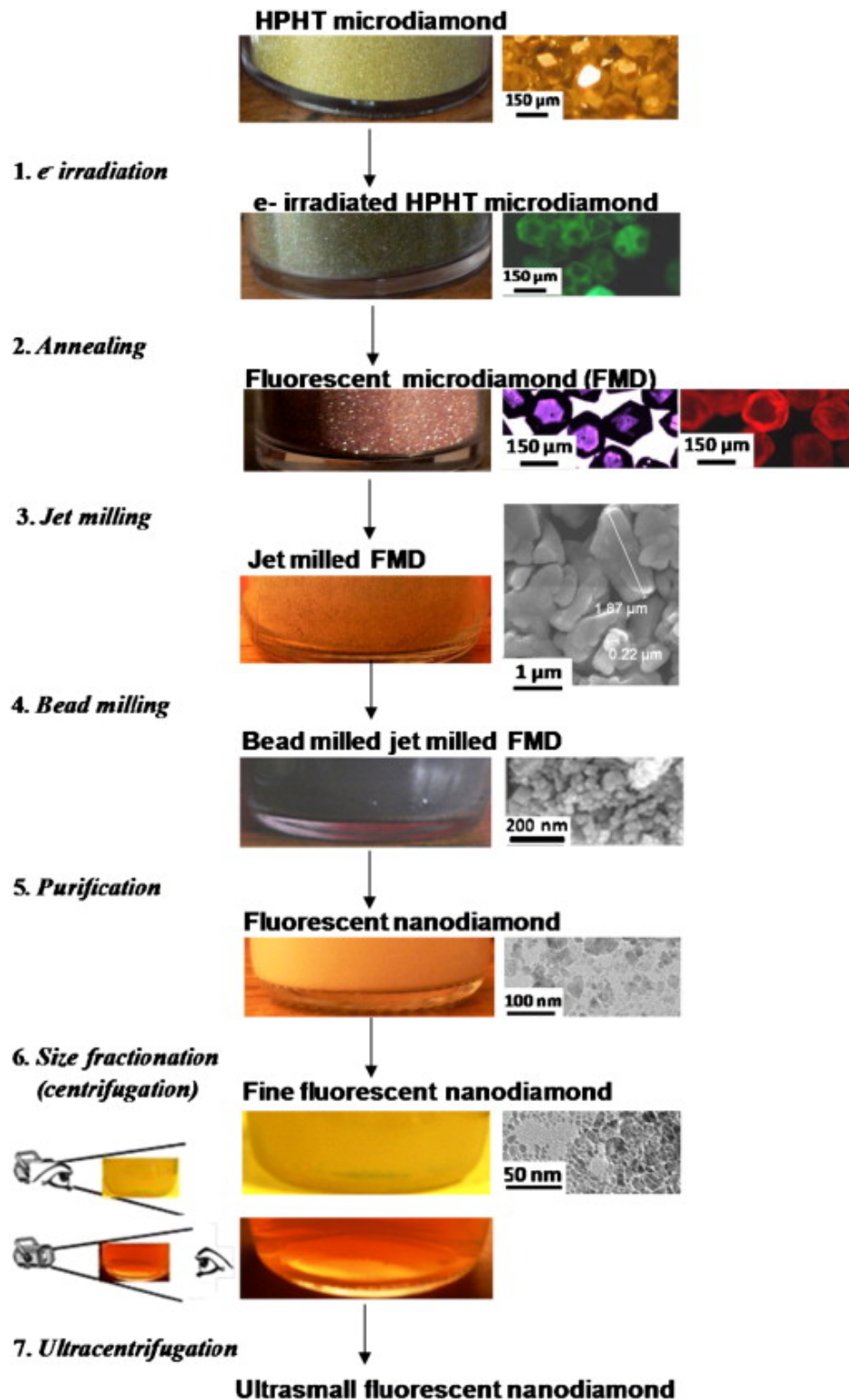


Fig. 3.5: NV-enriched NDs preparation. Reproduced from Ref. [46].

increase NV concentration in micro-sized diamonds and then reduce their size to obtain fluorescent NDs. This was done by Boudou et al. [46], in what has become the standard fluorescent NDs synthesis technique. The procedure is shown in Fig. 3.5. The starting material is HPHT-synthesized microdiamonds, that are then irradiated with a 10 MeV electron beam to form vacancies. The following step is the annealing at 750°C to form fluorescent microdiamonds. The next step is the reduction of diamond size, achieved by nitrogen jet milling and ball milling to obtain NDs with a crystal size smaller than 10 nm. For bioimaging, which is the main field of applications for fluorescent NDs, the number of NV centers should be as high as possible. For this reason, only HPHT diamonds, that contain a relevant amount of nitrogen impurities, are used. On the opposite, CVD diamonds films contain a very small number of nitrogen atoms [47]. Consequently, highly fluorescent NDs are not produced by this mechanisms, that is rather used to produce nanocrystalline diamond film with single NV centers, suitable for quantum information technologies.

3.3 Pulsed laser ablation for nanodiamonds synthesis

Among the many technique for NDs synthesis, laser ablation is acquiring an increasing interest. Pulsed laser ablation (PLA), that has become a standard method for synthesis of nanoparticles [48], consists in the irradiation of the surface of a solid target with intense and short laser pulses. In our particular case of NDs synthesis, a graphite target is irradiated with laser pulses of 20 ns duration with laser fluence ranging from 1 to tens J cm^{-2} . The ablation can be performed in a vacuum chamber [49], so that the nanoparticles deposit on a substrate in front of the target, or in a liquid [50], where nanoparticles are dispersed. In this section, the physical process leading to nanoparticles formation through this technique is described, as it will be used to explain NDs production in the following chapters of this thesis. This process is known as phase explosion [51]. It occurs when a superheated liquid temperature reaches a value of about 90% of the critical temperature T_c . This process is the most efficient mechanism for short laser pulses, leading to the ejection of liquid nanodroplets, that eventually turn into nanoparticles after solidification.

3.3.1 Phase explosion

The first consequence of laser irradiation of a solid target is the melting of its surface. Moreover, typical laser fluences used for PLA (in the order of $\sim \text{J cm}^{-2}$) brings the surface temperature to the boiling temperature T_b . But, if the laser energy is deposited on a timescale smaller respect to the time needed for the nucleation of vapour bubbles, the target surface becomes a superheated liquid. This takes place when the laser pulses duration is $< 100 \text{ ns}$ [51], as in our case. Phase explosion takes place when the laser fluence is high enough that the temperature of this superheated liquid lies sufficiently close the thermodynamic critical temperature T_c [52]. The consequence is the formation of vapour bubbles through homogeneous nucleation. To understand phase explosion mechanism, the main aspect of nucleation theory are here reviewed. Fig. 3.6 shows the typical $p - T$ phase diagram in the neighborhood of T_c . The binodal line (green curve

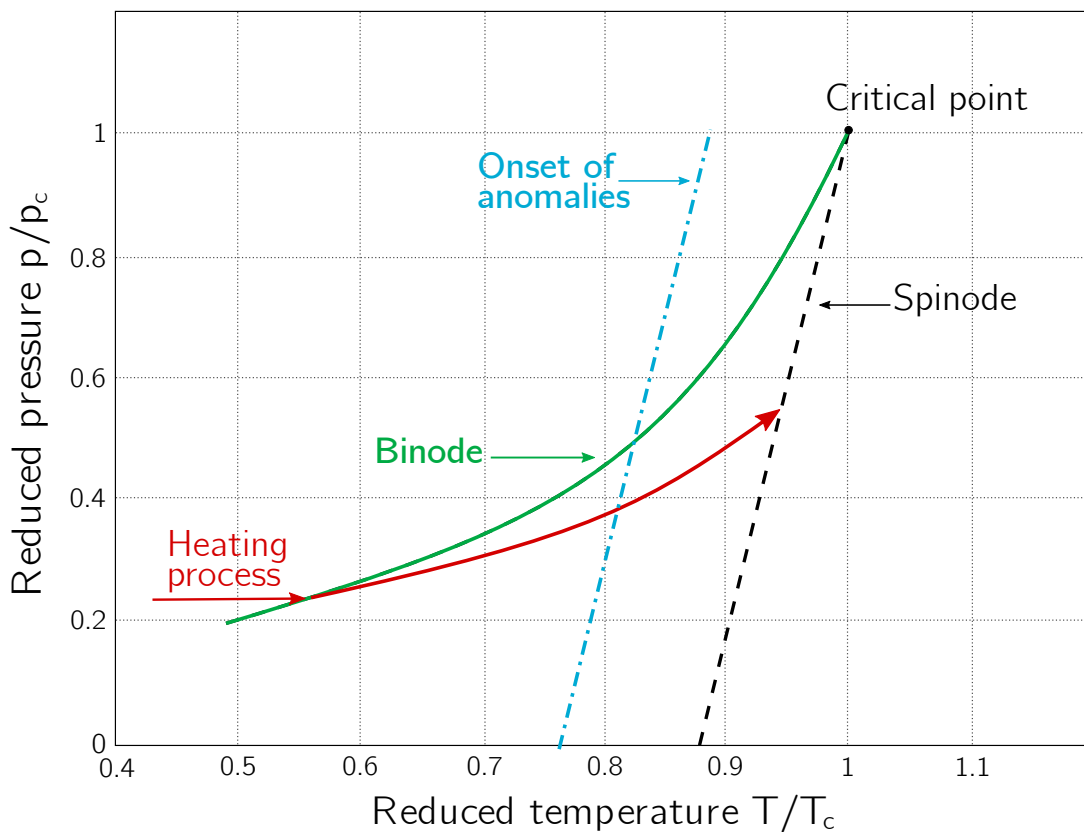


Fig. 3.6: $p - T$ phase diagram in the neighborhood of T_c .

in Fig. 3.6) is defined by the state of pressure and temperature in which the vapor and liquid phase coexist in thermodynamic equilibrium. Namely, the binode represents the normal boiling. However, during the fast heating caused by laser irradiation (red

arrow in Fig. 3.6), the temperature of the liquid becomes higher than T_b without the formation of vapour bubbles, leading to a superheated liquid. This metastable phase can be heated up to the spinodal line (black dashed line in Fig. 3.6). When the temperature of the liquid is close to the critical temperature ($T \gtrsim 0.80 T_c$), its properties, such as density and enthalpy, undergo strong fluctuations. This range of the temperatures is indicated on the picture with the blue line "onset of anomalies". These fluctuations in the density of the liquid brings to homogeneous nucleation of vapor bubbles. In details, the behavior of the liquid density ρ_l and that of the coexisting vapor phase ρ_v is given in Fig. 3.7. When approaching the critical point, homogeneous nucleation of vapor bubbles leads to a strong increase of vapor density. More quantitatively, the rate of

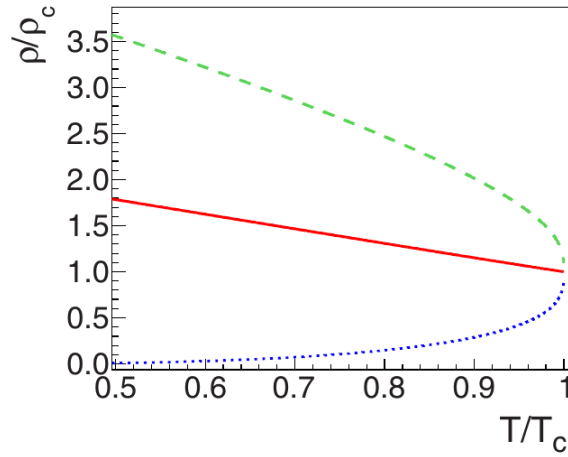


Fig. 3.7: Coexistence curve: ρ_l/ρ_c (dashed green curve), ρ_v/ρ_c (dotted blue curve), and average density (solid red curve). ρ_l , and ρ_v are the density of the liquid phase and of the vapour phase, while ρ_c is the density at T_c . Reproduced from [53].

homogeneous nucleation of critical vapor bubbles per unit volume J_s has an exponential dependence on temperature [53]

$$J_s = n_l \sqrt{\frac{6\sigma}{(3-b)\pi m}} \exp\left(-\frac{\Delta h_v}{RT}\right) \exp\left(-\frac{W_c}{k_B T}\right), \quad (3.1)$$

where σ is the surface tension, Δh_v is the enthalpy of vaporization, m is the mass of one molecule or atom and n_l is the number density of the liquid. The coefficient b is given by $b = 1 - p_l/p_v$, where p_l is the pressure of the liquid phase and p_v is the vapour pressure inside vapor bubble, which is given by [54]

$$p_v = p_s \exp\left(\left(p_l - p_s\right) \frac{v_l}{k_B T}\right), \quad (3.2)$$

3.3. PULSED LASER ABLATION FOR NANODIAMONDS SYNTHESIS

where v_l is the molar volume of the liquid phase and p_s is the saturated vapour pressure, obtained by the Clausius-Clapeyron equation. A vapor bubble nucleating in the liquid, to be stable, has to reach the critical radius r_c . This parameter is defined as $\partial G(r)/\partial r < 0$ for $r > r_c$, where $G(r)$ is the Gibbs free energy. Namely, it is the radius for which the nucleus starts growing spontaneously. The expression for r_c is:

$$r_c = \frac{2\sigma}{p_v - p_l}, \quad (3.3)$$

The coefficient W_c in Eq. (3.1) is the energy barrier to reach the critical radius r_c , and it is given by:

$$W_c = \frac{4}{3}\pi r_c^2 \sigma = \frac{16\pi\sigma^3}{3(p_v - p_l)^2}. \quad (3.4)$$

The result obtained are shown in Fig. 3.8, which shows the critical radius r_c and the nucleation rate J_s temperature behavior. By approaching T_c , the critical radius decreases and the rate of nucleation increases dramatically (several orders of magnitude), resulting in a large number of bubbles. As it can be observed, J_s becomes relevant only when the laser fluence is high enough so that the target surface temperature reaches $\sim 0.9T_c$. For this reason, phase explosion is a threshold process: below a certain laser fluence (depending of the target material) the process does not occur. Summarizing,

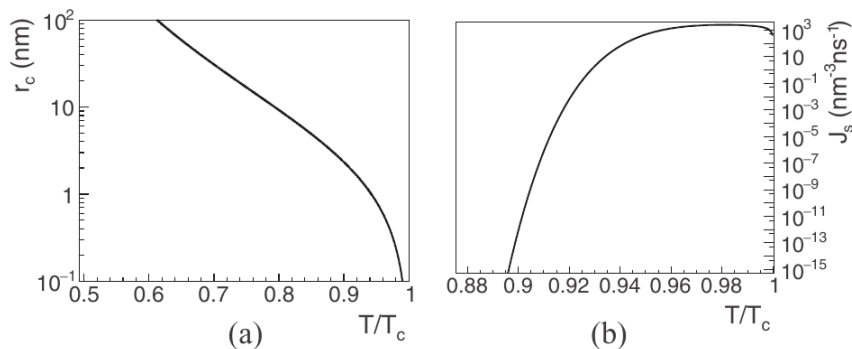


Fig. 3.8: (a) Critical radius of vapour bubbles inside the metastable liquid in function of the temperature. (b) Nucleation rate of vapour bubbles (in the case of iron). Reproduced from [53].

upon pulsed laser irradiation, the target becomes a superheated liquid. If the laser fluence is high enough - between 1 and 10 J cm^{-2} for most materials [53] - the surface layers of the target becomes a mixture of liquid droplets surrounded by vapour bubbles. The growth of the vapor bubbles eventually leads to an explosive boiling, resulting in the ejection of the trapped liquid droplets [55]. The expelled material forms the so called ablation plume. The liquid nanodroplets finally solidify into nanoparticles on the

substrate over which they are deposited. The size of the emitted liquid nanodroplets, in the case of PLA of graphite, is estimated from homogeneous nucleation theory in the experimental chapters of this thesis.

3.3.2 Pulsed laser ablation in liquid

As already mentioned in the beginning of this section, PLA can be performed with the target in vacuum (or in a low pressure gas) or immersed in a liquid. Both these methods are used in the experimental part of this thesis. However, the presence of a liquid layer in front of the irradiated target leads to peculiar physical processes, that

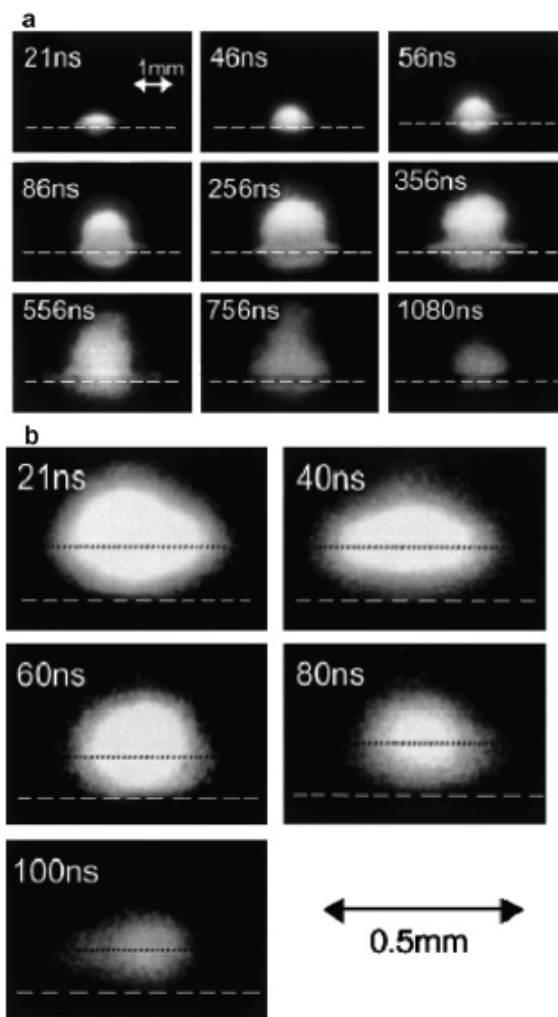


Fig. 3.9: Ablation plume expansion at different time intervals after graphite laser irradiation. The ablation is performed in air (a) and in water (b), with a Nd:YAG laser (wavelength 1064 nm, pulses duration 20 ns, fluence 10 J/cm²). Reproduced from [56].

will be used to explain the higher NDs formation efficiency. The two processes are: an high pressure inside the ablation plume and an high cooling rate of the emitted particles. Both are a direct consequence of the expansion of the ablation plume in a dense environment, with consequent strong confinement exerted by the liquid layer. The consequences of the plume confined expansion can be seen in Fig. 3.9 (b), for ablation of graphite in water. Firstly, one can observe that the lifetime of the plume in water is around 100 ns, much smaller respect to the 1000 ns of the ablation in air (Fig. 3.9 (a)). Due to the confinement effect, the ablation plume dissipates excess heat very efficiently through collisional cooling with the liquid molecules, resulting in a short quenching time of the plume. This is the most peculiar characteristic of laser ablation in liquid: the very high cooling rate, that can be in the order of 10^{10} - 10^{11} K s⁻¹ [57], favors the formation of metastable phases, such as diamond. Another important observation of Fig. 3.9 (b) is the size of the plume. Indeed, it reaches a maximum lateral size of 150 μm , an order of magnitude smaller compared to the 1.5 mm diameter of the plume forming in air under the same irradiation conditions. This brings to an higher pressure inside the ablation plume. Regarding the increase in the pressure in the ablation plume, another peculiar process arising from the presence of a confining liquid layer must be considered: the emission of a shock wave [57]. Indeed, laser absorption and subsequent material expulsion from the target induces a mechanical impulse to this solid [58] by emission of a shock wave, that in turn brings to an increase in the pressure inside the plume. Direct measurements of this shock-induced pressure for graphite ablation are lacking, but interesting results are obtained for different targets. For instance, irradiation of an aluminum target in water with a 20 ns laser pulse having power density of 10 GW cm^{-2} leads to a pressure of 5.5 GPa [59]. For the graphite case, a theoretical estimation of this value is reported in Chapter 4 and Chapter 6. Summarizing, the main feature of PLA is the extreme condition reached inside the laser-induced plume. The pressure reaches values in the order of 10^9 Pa and cooling rates of $> 10^{10}$ K s⁻¹. This thermodynamic condition leads to the transition of the expelled liquid nanodroplets into unusual metastable phases. Finally, another possibility offered by PLA, both in liquid or in a vapor environment, is represented by chemical reactions between the species contained in the plume and the molecules/atoms of the medium, taking place in the plume/confining-medium boundary [57]. With this technique doping of nanoparticles was demonstrated [60], for different combination of solid target and medium in which ablation is performed.

References for chapter 3

- [1] Danilenko, V. V. (2004). On the history of the discovery of nanodiamond synthesis.
- [2] Greiner, N. R., Phillips, D. S., Johnson, J. D., & Volk, F. (1988). Diamonds in detonation soot. *Nature*, 333(6172), 440.
- [3] Zhu, Y., Li, J., Li, W., Zhang, Y., Yang, X., Chen, N., et al. (2012). The biocompatibility of nanodiamonds and their application in drug delivery systems. *Theranostics*, 2(3), 302.
- [4] Meinhardt, T., Lang, D., Dill, H., & Krueger, A. (2011). Pushing the functionality of diamond nanoparticles to new horizons: orthogonally functionalized nanodiamond using click chemistry. *Advanced Functional Materials*, 21(3), 494-500.
- [5] Behler, K. D., Stravato, A., Mochalin, V., Korneva, G., Yushin, G., & Gogotsi, Y. (2009). Nanodiamond-polymer composite fibers and coatings. *ACS nano*, 3(2), 363-369.
- [6] Shimkunas, R. A., Robinson, E., Lam, R., Lu, S., Xu, X., Zhang, X. Q., et al. (2009). Nanodiamond-insulin complexes as pH-dependent protein delivery vehicles. *Biomaterials*, 30(29), 5720-5728.
- [7] Alhaddad, A., Adam, M. P., Botsoa, J., Dantelle, G., Perruchas, S., Gacoin, T., et al. (2011). Nanodiamond as a vector for siRNA delivery to Ewing sarcoma cells. *Small*, 7(21), 3087-3095.
- [8] Krueger, A. (2008). The structure and reactivity of nanoscale diamond. *Journal of Materials Chemistry*, 18(13), 1485-1492.
- [9] Pierson, H. O. (2012). *Handbook of carbon, graphite, diamonds and fullerenes: processing, properties and applications*. William Andrew.
- [10] Narayan, R. J., Boehm, R. D., & Sumant, A. V. (2011). Medical applications of diamond particles & surfaces. *Materials today*, 14(4), 154-163.
- [11] Khan, M. B., & Khan, Z. H. (2018). *Nanodiamonds: synthesis and applications*. In *Nanomaterials and their applications* (pp. 1-26). Springer, Singapore.
- [12] Liu, X., & Xu, X. (2017). Ultra-fine polishing of glass-ceramics by disaggregated and fractionated detonation nanodiamond. *Ceramics International*, 43(8), 6063-6068.
- [13] Dolmatov, V. Y. (2001). Detonation synthesis ultradispersed diamonds: properties and applications. *Russian Chemical Reviews*, 70(7), 607-626.
- [14] Mochalin, V. N., Shenderova, O., Ho, D., & Gogotsi, Y. (2012). The properties and applications of nanodiamonds. *Nature nanotechnology*, 7(1), 11.
- [15] Kato, T. (2009). Lubrication property of single-digit-nano diamond in an aqueous colloid. *J. Jpn. Soc. of Trib.*, 54(2), 122.

- [16] Mochalin, V. N., Neitzel, I., Etzold, B. J., Peterson, A., Palmese, G., & Gogotsi, Y. (2011). Covalent incorporation of aminated nanodiamond into an epoxy polymer network. *ACS nano*, 5(9), 7494-7502.
- [17] Neitzel, I., Mochalin, V., Knoke, I., Palmese, G. R., & Gogotsi, Y. (2011). Mechanical properties of epoxy composites with high contents of nanodiamond. *Composites science and technology*, 71(5), 710-716.
- [18] Lee, J. Y., Lim, D. P., & Lim, D. S. (2007). Tribological behavior of PTFE nanocomposite films reinforced with carbon nanoparticles. *Composites Part B: Engineering*, 38(7-8), 810-816.
- [19] Shenderova, O., Jones, C., Borjanovic, V., Hens, S., Cunningham, G., Moseenkov, S., et al. (2008). Detonation nanodiamond and onion-like carbon: applications in composites. *physica status solidi (a)*, 205(9), 2245-2251.
- [20] Fox, K., Tran, P. A., Lau, D. W., Ohshima, T., Greentree, A. D., & Gibson, B. C. (2016). Nanodiamond-polycaprolactone composite: A new material for tissue engineering with sub-dermal imaging capabilities. *Materials Letters*, 185, 185-188.
- [21] Zhang, Q., Mochalin, V. N., Neitzel, I., Knoke, I. Y., Han, J., Klug, C. A., et al. (2011). Fluorescent PLLA-nanodiamond composites for bone tissue engineering. *Biomaterials*, 32(1), 87-94.
- [22] Chang, Y. R., Lee, H. Y., Chen, K., Chang, C. C., Tsai, D. S., Fu, C. C., et al. (2008). Mass production and dynamic imaging of fluorescent nanodiamonds. *Nature nanotechnology*, 3(5), 284.
- [23] Faklaris, O., Joshi, V., Irinopoulou, T., Tauc, P., Sennour, M., Girard, H., et al. (2009). Photoluminescent diamond nanoparticles for cell labeling: study of the uptake mechanism in mammalian cells. *ACS nano*, 3(12), 3955-3962.
- [24] Horowitz, V. R., Alemán, B. J., Christle, D. J., Cleland, A. N., & Awschalom, D. D. (2012). Electron spin resonance of nitrogen-vacancy centers in optically trapped nanodiamonds. *Proceedings of the National Academy of Sciences*, 109(34), 13493-13497.
- [25] Baffou, G., Rigneault, H., Marguet, D., & Jullien, L. (2014). A critique of methods for temperature imaging in single cells. *Nature methods*, 11(9), 899.
- [26] Huang, H., Pierstorff, E., Osawa, E., & Ho, D. (2007). Active nanodiamond hydrogels for chemotherapeutic delivery. *Nano letters*, 7(11), 3305-3314.
- [27] Chow, E. K., Zhang, X. Q., Chen, M., Lam, R., Robinson, E., Huang, H., et al. (2011). Nanodiamond therapeutic delivery agents mediate enhanced chemoresistant tumor treatment. *Science translational medicine*, 3(73), 73ra21-73ra21.
- [28] Huang, H., Pierstorff, E., Osawa, E., & Ho, D. (2008). Protein-mediated assembly of nanodiamond hydrogels into a biocompatible and biofunctional multilayer nanofilm. *ACS nano*, 2(2), 203-212.

BIBLIOGRAPHY

- [29] Dundek, M. (2010). *Diamonds*. Marijan Dundek.
- [30] Gordon Davies, I. N. S. P. E. C. (1994). *Properties and growth of diamond*. INSPEC publication, Institution of Electrical Engineers.
- [31] Shenderova, O. A. Gruen, D. M. *Ultrananocrystalline Diamond: Synthesis, Properties, and Applications* (William Andrew, 2006)
- [32] Danilenko, V. V. in *Synthesis, Properties and Applications of Ultrananocrystalline Diamond* (Proceedings of NATO Advanced Research Workshop) (eds Gruen, D. Shenderova O. & Vul', A.) 181–198 (Springer, 2005).
- [33] Osswald, S., Yushin, G., Mochalin, V., Kucheyev, S. O., & Gogotsi, Y. (2006). Control of sp²/sp³ carbon ratio and surface chemistry of nanodiamond powders by selective oxidation in air. *Journal of the American Chemical Society*, 128(35), 11635-11642.
- [34] Ōsawa, E. (2007). Recent progress and perspectives in single-digit nanodiamond. *Diamond and Related Materials*, 16(12), 2018-2022.
- [35] Butler, J. E., & Sumant, A. V. (2008). The CVD of nanodiamond materials. *Chemical Vapor Deposition*, 14(7-8), 145-160.
- [36] Park, J. W., Kim, K. S., & Hwang, N. M. (2016). Gas phase generation of diamond nanoparticles in the hot filament chemical vapor deposition reactor. *Carbon*, 106, 289-294.
- [37] May, P. W., Ashfold, M. N. R., & Mankelevich, Y. A. (2007). Microcrystalline, nanocrystalline, and ultrananocrystalline diamond chemical vapor deposition: Experiment and modeling of the factors controlling growth rate, nucleation, and crystal size. *Journal of Applied Physics*, 101(5), 053115.
- [38] Akaishi, M., Kanda, H., & Yamaoka, S. (1990). Synthesis of diamond from graphite-carbonate system under very high temperature and pressure. *Journal of Crystal Growth*, 104(2), 578-581.
- [39] Boudou, J. P., Curmi, P. A., Jelezko, F., Wrachtrup, J., Aubert, P., Sennour, M., et al. (2009). High yield fabrication of fluorescent nanodiamonds. *Nanotechnology*, 20(23), 235602.
- [40] Rehor, I., & Cigler, P. (2014). Precise estimation of HPHT nanodiamond size distribution based on transmission electron microscopy image analysis. *Diamond and Related Materials*, 46, 21-24.
- [41] Reineck, P., Capelli, M., Lau, D. W. M., Jeske, J., Field, M. R., Ohshima, T., et al. (2017). Bright and photostable nitrogen-vacancy fluorescence from unprocessed detonation nanodiamond. *Nanoscale*, 9(2), 497-502.
- [42] Hui, Y. Y., Cheng, C. A., Chen, O. Y., & Chang, H. C. (2016). Bioimaging and quantum sensing using NV centers in diamond nanoparticles. In *Carbon Nanoparticles and Nanostructures* (pp. 109-137). Springer, Cham.

- [43] Orwa, J. O., Santori, C., Fu, K. M. C., Gibson, B., Simpson, D., Aharonovich, I., et al. (2011). Engineering of nitrogen-vacancy color centers in high purity diamond by ion implantation and annealing. *Journal of applied physics*, 109(8), 083530.
- [44] Bradac, C., Gaebel, T., Naidoo, N., Rabeau, J. R., & Barnard, A. S. (2009). Prediction and measurement of the size-dependent stability of fluorescence in diamond over the entire nanoscale. *Nano letters*, 9(10), 3555-3564.
- [45] Smith, B. R., Inglis, D. W., Sandnes, B., Rabeau, J. R., Zvyagin, A. V., Gruber, D., et al. (2009). Five-nanometer diamond with luminescent nitrogen-vacancy defect centers. *Small*, 5(14), 1649-1653.
- [46] Boudou, J. P., Tisler, J., Reuter, R., Thorel, A., Curmi, P. A., Jelezko, F., & Wrachtrup, J. (2013). Fluorescent nanodiamonds derived from HPHT with a size of less than 10 nm. *Diamond and Related Materials*, 37, 80-86.
- [47] Abe, E., & Sasaki, K. (2018). Tutorial: Magnetic resonance with nitrogen-vacancy centers in diamond—microwave engineering, materials science, and magnetometry. *Journal of Applied Physics*, 123(16), 161101.
- [48] Kim, M., Osone, S., Kim, T., Higashi, H., & Seto, T. (2017). Synthesis of nanoparticles by laser ablation: A review. *KONA Powder and Particle Journal*, 2017009.
- [49] Singh, S. C., & Zeng, H. (2012). Nanomaterials and nanopatterns based on laser processing: A brief review on current state of art. *Science of Advanced Materials*, 4(3-4), 368-390.
- [50] Amendola, V., & Meneghetti, M. (2009). Laser ablation synthesis in solution and size manipulation of noble metal nanoparticles. *Physical chemistry chemical physics*, 11(20), 3805-3821.
- [51] Miotello, A., & Kelly, R. (1999). Laser-induced phase explosion: new physical problems when a condensed phase approaches the thermodynamic critical temperature. *Applied Physics A*, 69(1), S67-S73.
- [52] Mazzi, A., & Miotello, A. (2017). Simulation of phase explosion in the nanosecond laser ablation of aluminum. *Journal of colloid and interface science*, 489, 126-130.
- [53] Mazzi, A., Gorrini, F., & Miotello, A. (2015). Liquid nanodroplet formation through phase explosion mechanism in laser-irradiated metal targets. *Physical Review E*, 92(3), 031301.
- [54] P.G. Debenedetti, *Metastable Liquids: Concepts and Principles* (Princeton University Press, Princeton, NJ, 1996) p. 179;
- [55] Mazzi, A., Gorrini, F., Miotello, A. (2017). Dynamics of liquid nanodroplet formation in nanosecond laser ablation of metals. *Applied Surface Science*, 418, 601-606.
- [56] Saito, K., Takatani, K., Sakka, T., & Ogata, Y. H. (2002). Observation of the light emitting region produced by pulsed laser irradiation to a solid-liquid interface. *Applied surface science*, 197, 56-60.

BIBLIOGRAPHY

- [57] Yan, Z., Chrisey, D. B. (2012). *Journal of Photochemistry and Photobiology C: Photochemistry Reviews*, 13(3), 204-223.
- [58] Fabbro, R., Fournier, J., Ballard, P., Devaux, D., & Virmont, J. (1990). Physical study of laser-produced plasma in confined geometry. *Journal of applied physics*, 68(2), 775-784.
- [59] Berthe, L., Fabbro, R., Peyre, P., Tollier, L., & Bartnicki, E. (1997). Shock waves from a water-confined laser-generated plasma. *Journal of Applied Physics*, 82(6), 2826-2832.
- [60] Chemin, A., Lam, J., Laurens, G., Trichard, F., Motto-Ros, V., Ledoux, G., et al. (2019). Doping nanoparticles using pulsed laser ablation in a liquid containing the doping agent. *Nanoscale Advances*, 1(10), 3963-3972.

Chapter 4

Nanodiamonds synthesis through pulsed laser ablation

In this chapter, the production of nanodiamonds (NDs) by pulsed laser ablation of a carbon precursor in water is demonstrated. The target materials are graphite and diamond-like carbon (DLC). Moreover, a cleaning methods of NDs from non-diamond carbon phases that do not require the use of strong acids is described. Finally, a thermodynamic model explaining the formation of NDs upon pulsed laser ablation of graphite is provided. We show that synthesis of the crystalline phase is driven by a graphite–liquid–diamond transition process that occurs at the extreme thermodynamic conditions reached inside the ablation plume. In this model, the physical processes occurring during laser irradiation of a solid target described in Chapter 3.3, in particular for ablation in a liquid environment, are directly used.

The content of this chapter is adapted from:

L. Basso, F. Gorrini, N. Bazzanella, M. Cazzanelli, C. Dorigoni, A. Bifone and A. Miotello, The modeling and synthesis of nanodiamonds by laser ablation of graphite and diamond-like carbon in liquid-confined ambient, *Appl. Phys. A* **124** (2018) 72

DOI: <https://doi.org/10.1007/s00339-017-1491-3>

© Springer-Verlag GmbH Germany, part of Springer Nature 2017

4.1 Introduction

NDs attracted a great interest and consequent active research as they are promising for a variety of applications in different fields [1–3]. The reason is that NDs maintain most of the superior properties of bulk diamond and transfer them at the nanoscale. The main limitation of NDs is the synthesis process: as a matter of fact, diamond phase requires very high pressures and temperatures, respectively, of the order of GPa and thousands of Kelvin, for its formation [4]. A number of techniques have been used for the NDs production, as discussed in Chapter 3.2. Here, we propose a method that enables NDs synthesis at room temperature and standard pressure conditions, a great advantage respect to the usually implemented expensive and complicated processes. The technique is pulsed laser ablation (PLA) of carbon targets immersed in water. Two different carbon target materials are used: graphite and DLC. The latter is an amorphous carbon material, characterized by having a strong portion of its carbon atoms (80%) in the sp^3 hybridization. In the first section 4.2 the results regarding NDs synthesis through PLA of graphite in water are reported. Firstly, the details of the experimental apparatus for laser ablation in liquid are provided. The water plays a double role: a medium where nanoparticles are suspended and collected during ablation and for confinement of the ablation plume, that favors diamond-phase formation. Furthermore, the description of a simple physico-chemical NDs purification method, needed for the removal of sp^2 -byproducts of the synthesis process, is given. It consists on the dispersion of the powder obtain during ablation in H_2O_2 and simultaneous irradiation with UV light. Then, the experimental results of NDs synthesis are presented and fully discussed. In particular, NDs are characterized through scanning electron microscopy (SEM) and Raman spectroscopy. In section 4.3, NDs production by ablation of DLC is reported. DLC is produced in the form of a thin film by standard pulsed laser deposition of graphite in vacuum. This film is then used as a target for laser ablation in water: DLC properties allows to produce NDs directly on the film by using a lower laser fluence compared to the graphite case. Finally, in section 4.4 we propose a thermodynamic model explaining the formation mechanism of NDs under the transient physical conditions in the ablation plume. The differences of ablation of graphite and DLC are taken into account.

4.2 NDs obtained through ablation of graphite in water

4.2.1 Experimental setup for PLA in water

The experimental setup used for pulsed laser ablation of the carbon target is shown schematically in Fig. 4.1. The target was put inside a glass vial filled with water. The ablation was performed by using a KrF excimer laser (Lambda Physik LPX220i) with pulse duration of 20 ns and wavelength of 248 nm. The laser beam was focused on the target surface, to a spot of $0.73 \pm 0.05 \text{ mm}^2$ (obtained by measuring the spot size on the target surface by scanning electron microscopy after one pulse irradiation). The laser energy used was in the range between 500 mJ and 600 mJ per pulse, with a repetition rate of 10 Hz. The final laser fluence reaching the target surface was in the between ~ 50 and $\sim 60 \text{ J cm}^{-2}$, where a $\sim 25\%$ energy loss at the focusing optics is considered. To focus the laser beam, a lens with a relatively long focal length (400 mm) was used to increase the distance between the objective and the water, to avoid deposition of water on the lenses during irradiation. To reduce the splashing of water outside the

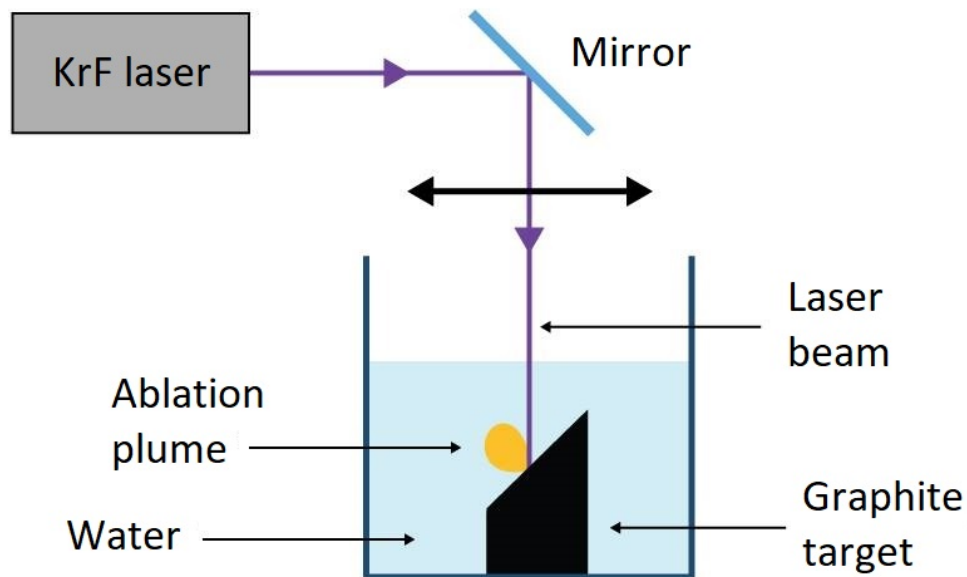


Fig. 4.1: Pulsed laser ablation in liquid experimental setup.

glass vial containing the target, as it brings also to the loss of the ablated particles dispersed in the liquid, a cylindrical graphite target with the top surface tilted by an angle of 45° was used, as schematically shown in Fig. 4.1. This expedient was used to reduce the spillage of water drops during irradiation, given that the ablation plume expansion is perpendicular to the graphite surface. The water in which the target is contained was ultrapure (conductivity of $0.055 \mu\text{S cm}^{-1}$) to avoid contamination of the forming nanoparticles. The thickness of the water layer above the laser focal spot was of 2-3 mm. The target was moved every ~ 1000 pulses to avoid the formation of a deep crater on the surface. The irradiation was performed for 1 h, in order to collect a relevant amount of ablated powder. At the end of the synthesis process, the graphite target was removed from the vial, and the water-suspended powder was slowly dried in an oven at 90°C , until complete evaporation of water.

4.2.2 Purification method

After PLA process, a purification step of the ablated powder from residual graphitic byproduct was necessary, in order to isolate the NDs. Indeed, as it will be detailed in section 4.4, NDs synthesized through PLA in water are embedded in a sp^2 -carbon shell that does not allow NDs characterization. To clean NDs from non-diamond phase, selective oxidation of sp^2 carbons is required. To do that, many different purification methods, with the oxidant agent being in gas- or liquid-phase, were reported [5]. Here, to isolate NDs from the graphitic byproducts, the following cleaning technique was implemented. The powder resulting from ablation was sonicated in 2-propanol for 3 h. Then, after 2-propanol complete evaporation, the powders were dispersed in a solution of concentrated hydrogen peroxide H_2O_2 in water (50% in weight), and irradiated by a UV lamp (power intensity of 140 mW cm^{-2} and wavelength of 365 nm) for 6 h. In the solution, hydroxyl groups $\cdot\text{OH}$ are formed upon ultraviolet-photons driven dissociation of hydrogen peroxide. This free radical removes graphitic residues from the surface of NDs, because $\cdot\text{OH}$ etches sp^2 carbons more efficiently than sp^3 carbons, due to the lower bond strength. After the irradiation, the water and residual H_2O_2 was evaporated, and the cleaned powders were deposited on a silicon substrate for characterization.

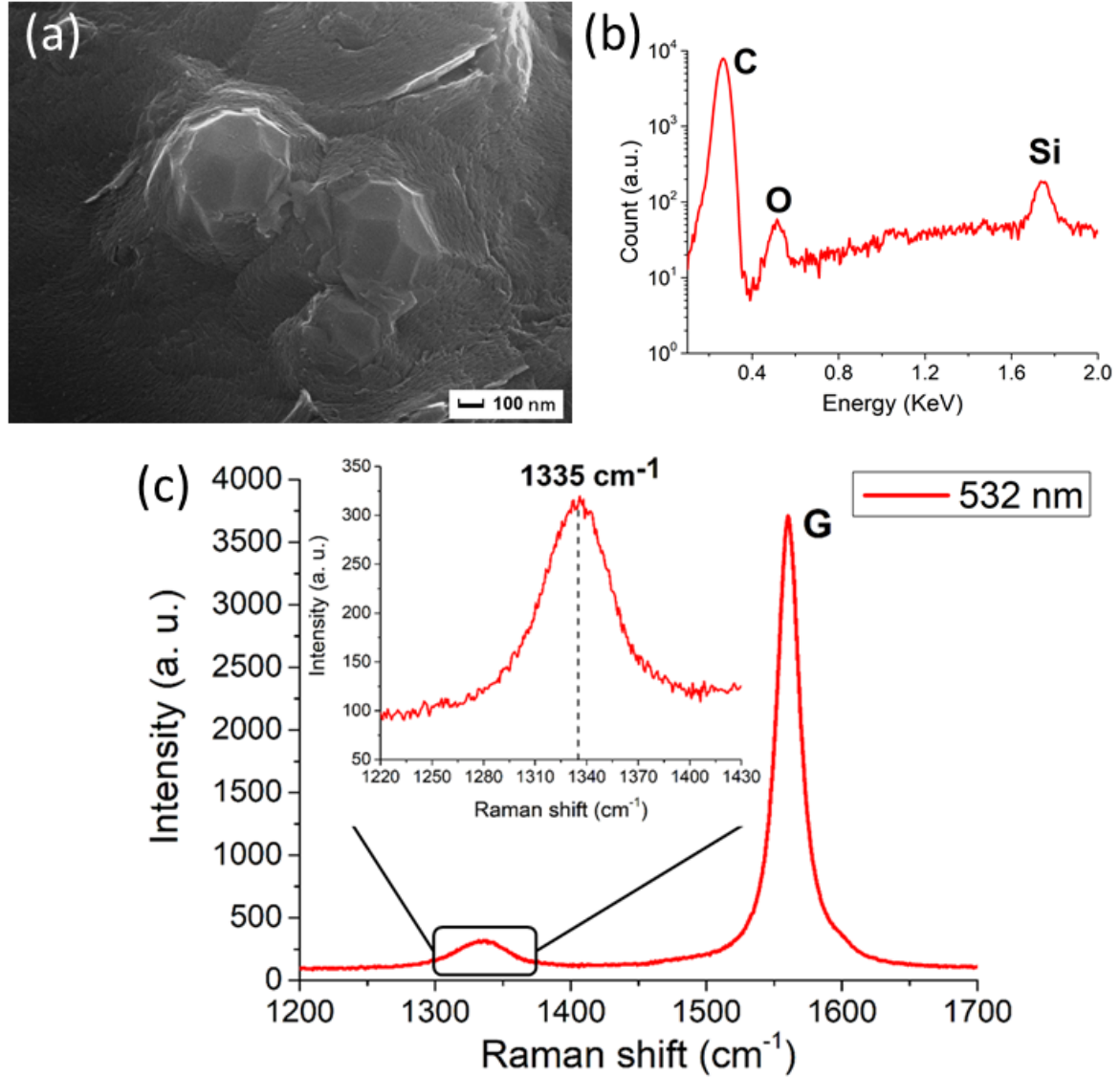


Fig. 4.2: Characterization of the NDs from graphite ablation in water (a) Typical SEM image, after removal of non-diamond phase of carbon, showing a multicrystalline particle of dimension less than 1 μm. (b) EDXS spectrum of the nanoparticles. Carbon peak is detected at 0.27 keV. Moreover, the peaks of silicon at 1.74 keV and of oxygen at 0.52 keV are observed. They come from the substrate on which the particles are deposited and from the oxidized surface layers of the ablated powders, respectively. (c) Raman spectrum (obtained under 532 nm excitation wavelength) of purified particles. The main peak at 1580 cm⁻¹ is the graphite G peak, while the peak at 1335 cm⁻¹ (shown in detail in the inset) is attributed to compressively-strained NDs

4.2.3 NDs characterization

The external morphology of the samples was studied by scanning electron microscopy (SEM), using a JSM- 7001F FEG-SEM, while the chemical composition of the nanoparticles was investigated by energy dispersive X-ray spectroscopy (EDXS). Moreover, microRaman spectroscopy was performed to get insight in the hybridization state of the carbon atoms, using a Jobin Yvon LabRAM ARAMIS spectrometer with a 532 nm as exciting wavelength. Fig. 4.2(a) shows a typical SEM image of the ablated particles after purification. Clustered crystallites having size in the order of hundreds of nanometers were obtained. The relative EDXS spectrum is reported in Fig. 4.2(b) and it confirms that the nanoparticles observed with SEM (Fig. 4.2(a)) are made of carbon, without contamination. The silicon signal in EDXS spectrum arises from the substrate on which the powders were deposited, whereas the oxygen peak comes from the oxidation of the surface layers of the samples. To prove that the nanoparticles observed in 4.2(b) are NDs, the purified samples were analyzed with Raman spectroscopy. Indeed with this technique, the different vibration frequencies of sp^3 carbon bonds respect to the sp^2 can be observed. The spectrum is reported in Fig. 4.2(c), showing the ND peak at 1335 cm^{-1} . Compared to bulk diamond, whose Raman peak is at 1332 cm^{-1} [6], NDs peak is shifted to higher wavenumbers: this can be attributed to the presence of stress in the NDs. In particular, compression exerted by the external graphitic matrix leads to an increase in the vibrational frequency of the carbon atoms [7]. The peak presents a full-width-half-maximum (FWHM) of 45 cm^{-1} that can be explained by the compressive strain [8] or by small size of the single diamond crystallites (ultrananocrystalline range) [9]. Nevertheless, the spectrum is still dominated by the graphite peak 1580 cm^{-1} , the so called G-peak. It means that a residual sp^2 carbon atom matrix embedding the NDs is still present. The graphite D-peak, usually at 1350 cm^{-1} , is not detected: this is most likely related to the small numbers of sixfold sp^2 carbon aromatic rings after laser irradiation and cleaning process [10]. On the opposite, organized sixfold aromatic rings are not required for the observation of the G peak. Indeed, the atomic vibrations giving rise to the G peak are present also when the carbons are organized in chain structures. Moreover, the strong intensity of the G peak, compared to the NDs peak, can be explained by considering that we are using visible Raman spectroscopy, which has a higher sensitivity to sp^2 carbons. The explanation is that visible photons have a higher cross section with the π bonds between sp^2 carbon atoms compared with the σ bonds between carbon atoms in the sp^3 hybridization [10].

4.3 NDs obtained through ablation of DLC in water

4.3.1 DLC synthesis

Standard pulsed laser deposition (PLD) of a graphite target in vacuum was used to produce diamond-like carbon (DLC) films. Graphite ablation was performed with the same KrF excimer laser already described, with the laser beam impinging on the target with a 45° incident angle focused to a spot diameter of 1 mm^2 . To avoid formation of a deep crater in the irradiation spot, the graphite target was rotating during ablation. Ablation was performed in high vacuum conditions, with a residual pressure of $1.1 \cdot 10^{-5}$ mbar inside the vacuum chamber. The laser fluence used was of $22 \pm 1 \text{ J cm}^{-2}$. This particular value was chosen on the basis of previous literature findings: Bonelli et al. [11] reported an increase in the fraction of sp^3 carbon atoms inside the deposited DLC film for large fluences. The total number of pulses was 5000 with a repetition rate of 10 Hz. The graphite target was placed at a distance of 7 cm from a silicon substrate, where the ablated material deposits. The silicon substrate cleaning procedure included three subsequent ultrasonic bath (10 min each) in acetone, ethanol, and deionized water, followed by a drying under a nitrogen flux. After deposition, an annealing was necessary to relax internal stress [12], which otherwise would lead to film delamination from the target. To this end, the substrate was mounted on a heated holder, that was brought, after deposition, to the temperature of 300°C (heating ramp $0.1\text{-}0.2^\circ\text{C s}^{-1}$) for 1 h. Before moving to NDs synthesis, the DLC film used as target for PLA is characterized. The microRaman spectrum (Fig. 4.3(c)), made by a broad peak at 1550 cm^{-1} , is typically observed for DLC made by a high fraction of its carbon atoms being in the sp^3 hybridization. By measuring the intensity ratio $I(\text{D})/I(\text{G})$ of the D peak and the G peak, Raman spectroscopy provides a qualitative means to estimate the sp^3/sp^2 ratio. As reported in Ref. [11], the $I(\text{D})/I(\text{G})$ ratio drops to zero when the sp^3 carbon atoms fraction becomes larger than $\sim 20\%$. In our case, the D peak is not visible: we can conclude that the sp^3 fraction of carbon atoms in the DLC film is above 20%. For DLC film deposition, the procedure reported in [11] was followed, where more qualitative analysis about the sp^3/sp^2 ratio (such as electron energy loss spectroscopy) was performed. In that work, sp^3 content of 80% was measured for the synthesized DLC films. Here, the same experimental conditions were used for DLC film deposition,

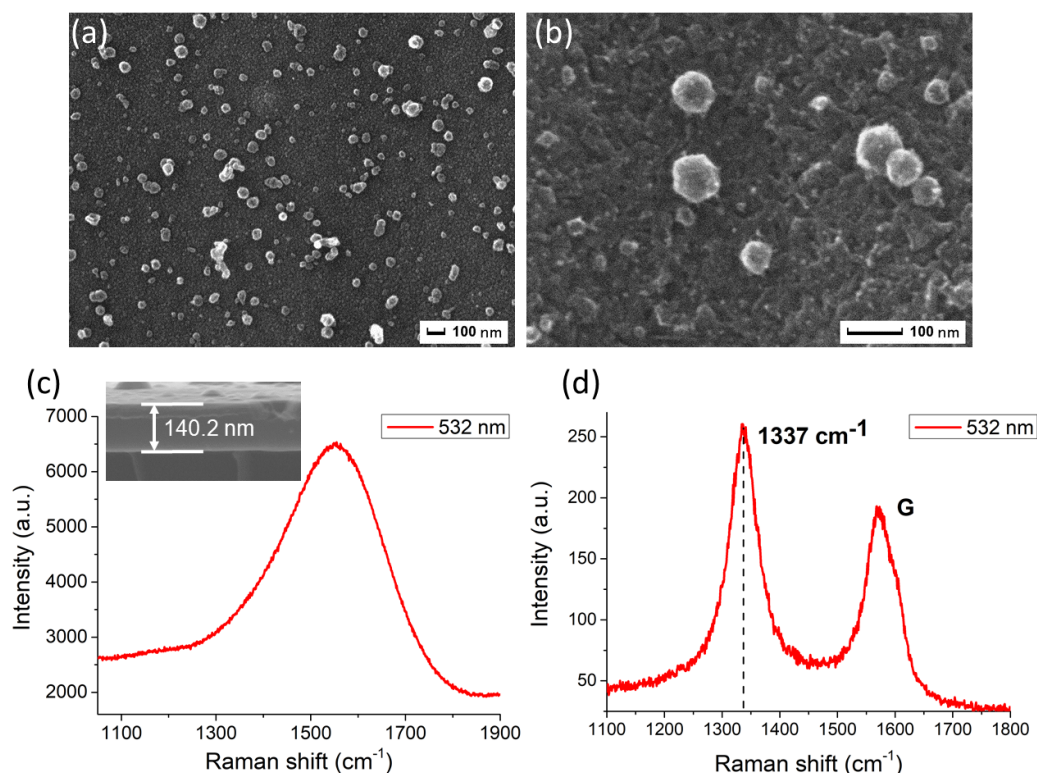


Fig. 4.3: Characterization of the NDs from laser irradiation of DLC in water. (a) and (b) show two SEM images of the irradiated DLC film with a fluence of 0.76 J cm^{-2} at different magnifications: nanoparticles below 100 nm size are dispersed on the carbon film. (c) Raman spectrum of the initial DLC film, with a 532 nm excitation wavelength. Only a broad peak at 1550 cm^{-1} is detected, a typical feature of DLC with high content of sp^3 carbon atoms [11]. The inset gives a cross-sectional SEM image of the deposited DLC, showing the 140 nm thickness of the film. (d) Raman spectrum of the irradiated film, under same excitation condition, showing the G peak at 1572 cm^{-1} , and the peak of compressively- strained NDs at 1337 cm^{-1} .

so we can safely assume that the sp^3 fraction is the same of [11]. As shown in the SEM image in the inset of Fig. 4.3(c), the film had a thickness 140 nm.

4.3.2 NDs synthesis and characterization

To produce NDs, the DLC films were used as target for laser irradiation. A DLC film was immersed in 2–3 mm of deionized water and irradiated with a single low-fluence shot of the KrF laser. To reach a small laser fluence of $0.76 \pm 0.05 \text{ J cm}^{-2}$, the laser beam was focused with a large spot size of $13.3 \pm 0.7 \text{ mm}^2$. This low laser fluence was used because the process leading to NDs formation is different respect to the ablation

of graphite, as it will be widely discussed in the following section. In the DLC case, we want to exploit the presence of sp^3 carbon atoms in the irradiated target. We are not interested in the removal of material, but rather in a reorganization in the structure of the atoms in the film. Indeed, this process may be referred more properly as laser annealing. Fig. 4.3(a) and (b) present the SEM images of the irradiated film at different magnification: nanoparticles with size below 100 nm are directly synthesized on the film by the laser annealing process. These carbon nanostructures were then characterized with Raman spectroscopy. The result is shown in Fig. 4.3(d): the G peak is detected at 1572 cm^{-1} , while the more relevant peak at 1337 cm^{-1} is attributed to compressed-strained NDs. An important remark to be made is that with laser irradiation of DLC a NDs purification process is non required.

4.4 Thermodynamic model

In this section, the thermodynamic model that was conceived to understand and explaining NDs production during pulsed laser ablation is described, starting for the case of graphite ablation in water. The development of this model is based on the two peculiarities of laser ablation in liquid ambient (already described in Chapter 3.3). These are the extreme thermodynamic conditions of pressure and temperature that can be obtained under pulsed laser ablation and the high cooling rate sustained by the ablation plume. In particular, the strong increase in the pressure is the consequence of the shockwave emission following laser ablation. However, this shock-induced pressure is not enough to reach the so-called high-temperature high-pressure (HPHT) conditions for diamond growth, namely to enter in diamond stable region of carbon phase diagram (Fig. 4.4). This statement is supported by the detailed analysis of the thermodynamic state of the plume reported by Amans et al. [13]. Moreover, Vicelli et al. [14] suggests that when carbon nanoparticles are considered, a shift of the triple point of carbon phase diagram toward higher pressure is observed, making HPHT growth unlikely. Furthermore, Kraus et al. [15] observed diamond formation through in situ X-ray diffraction after shock compression of graphite (both pyrolytic and polycrystalline) upon nanosecond laser ablation. The carbon phase diagram is reported in Fig. 4.4. As it can be noted, with the particular thermodynamic conditions of pressure ($2 - 4\text{ GPa}$ [16, 17]) and of temperature (5000 K [18]), the system is in the liquid carbon area (green region). Thus, the material is expelled from the target - trough laser-induced phase explosion

process - in the form of liquid carbon nanodroplets [19, 20]. The presence of the liquid phase is an essential step of this model, because, as it will be explained, diamond phase forms starting from undercooled liquid carbon. A comment regarding the temperature of the plasma must be introduced. The reported temperature of 5000 K [18] refers to the rotational temperature of C_2 diatomic molecules, mainly related to rigid movement of the molecule [13]. Despite thermodynamic equilibrium is not reached inside the plume, collisions between ablated molecules [21] allows to correlate the rotational temperature to the kinetic temperature of heavy species. Eventually the temperature of the plume will decrease, and the liquid carbon nanodroplets returns to the solid state. The phase in which it solidifies - graphite or diamond - is determined by the cooling rate: as explained in chapter 3.3, cooling rates of 10^{10} - 10^{11} K s^{-1} are reached for a plume expanding inside a liquid. This strong and fast reduction in the temperature is enough to bring the liquid carbons in an undercooling regime in a few nanoseconds. In this condition, with the system out of thermodynamic equilibrium, the coexistence curve line between the graphite-phase and the diamond-phase in the carbon phase diagram is no longer well defined, as the one described by the equilibrium phase diagram in Fig. 4.4. Then, the system is brought into a region, schematized by the enlarged dashed red arrow in Fig. 4.4, in which diamond phase is formed as metastable phase. The synthesis of NDs through a rapid quenching of liquid carbon was also observed in other works. Narayan et al. [22] reported NDs synthesis upon quenching of melted DLC and Yu et al. [23] observed a similar result at a relatively low pressure (12 MPa) and temperature (4160 K). In both cases, the undercooled liquid crossed the melting line of graphite without a phase transition, acquiring ~ 1000 K of undercooling. In this condition of undercooling, NDs form as a metastable phase starting from the liquid nanodroplets expelled by phase explosion. The transition to the thermodynamic stable allotrope of carbon, namely graphite, is prevented by the rapid quenching: the metastable phase is literally frozen under the undercooling action. The time interval in which diamond phase forms is set by the duration of the shockwave-induced high-pressure state. This value is estimated to be twice the duration of the laser pulse [17, 24]. Finally, when pressure drops, only graphite phase is formed, and sp^2 structures forms around NDs, thus requiring purification of the samples. Summarizing, the most important parameter to explain NDs synthesis is undercooling state. Even if the system does not enter in the diamond stable region of carbon phase diagram, the undercooling process leads to diamond phase formation. This peculiar characteristic of the ablation in liquid

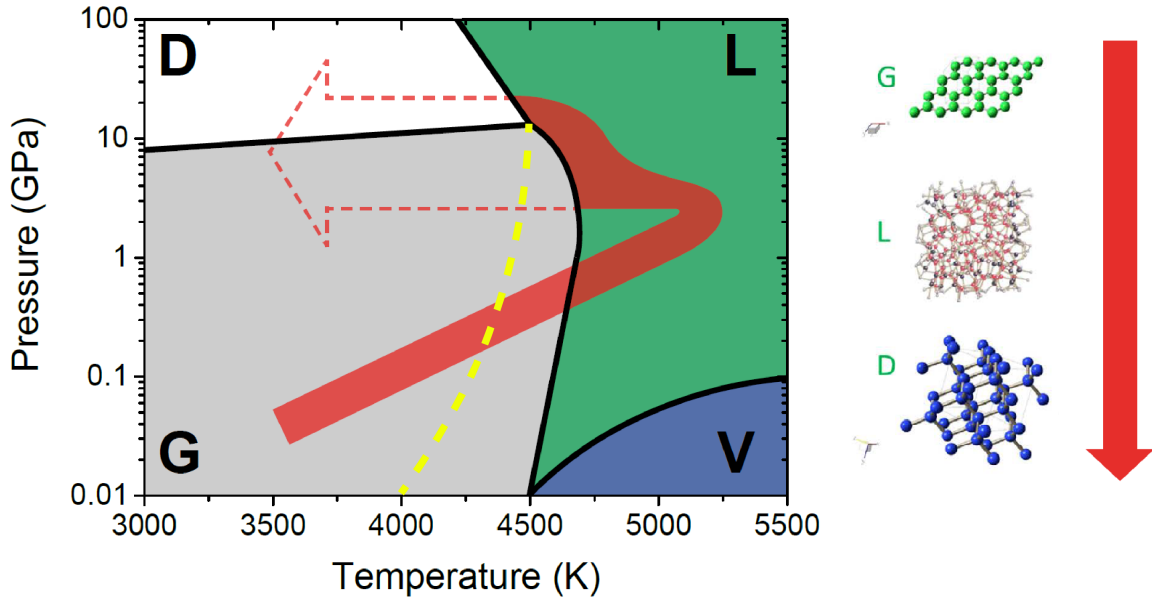


Fig. 4.4: Carbon phase diagram. Regions of thermodynamical stability of the different carbon phases are labeled with different colors. Grey for graphite (G), green for liquid carbon (L), white for diamond (D) and blue for gaseous carbon (V). The yellow dashed curve represents the melting point of DLC as a function of pressure [22]. The red arrow indicates the path for the formation of NDs during ablation of graphite in water. In the first step, the system is brought into the liquid carbon region. Subsequently, the liquid carbon is undercooled, a regime that enables formation and crystallization of metastable diamond phase. The dotted red arrow stresses the fact that the system is out of equilibrium, and that the graphite and the diamond regions are no longer well defined as in thermodynamic equilibrium conditions. The right side of the image represents a schematization of the multi-step graphite-liquid-diamond process that yields the NDs.

is strongly exploited in the synthesis of NDs by ablation of DLC in water. In this case, laser irradiation is performed with a smaller laser fluence, resulting in a weaker confinement exerted by the liquid layer. Indeed, as the shock-wave induced pressure represents the recoil pressure acting on the target, its value is proportional to the energy deposited by the laser pulse [15]. In this case, the increase of the pressure is then smaller. Moreover, the ablation is not relevant with this low laser fluence; therefore, the process can be referred as laser annealing. The explanation of ND formation upon laser irradiation of DLC is based on two evidences. Firstly, in the DLC film there are already sp^3 clusters [25], given the large amount of sp^3 carbon atoms (80% in our case), without a crystalline order. Secondly, DLC melts at much lower temperature compared to crystalline carbon [22]. As indicated by the yellow curve of Fig. 4.4, showing DLC melting temperature, DLC melts at lower temperature compared to graphite. As a

consequence, by using a low fluence laser pulse that would not be able to melt a graphite target, the irradiated DLC film is melted by laser annealing. When the amorphous carbon becomes liquid, it enters in an undercooled regime. Indeed, according to carbon phase diagram, the system is in the region in which carbon atoms are in solid phase. In this undercooled state, NDs form in the surface of the DLC target using as nucleation seeds the sp^3 carbon clusters already present. Summarizing, respect to graphite, the choice of DLC as a target provides a double advantage. It allows the liquid carbon to enter in an undercooling regime after irradiation with a less energetic laser pulse (0.76 J cm^{-2} vs more than 50 J cm^{-2}). This enables ND formation just by laser melting of the target, rather than by explosive ablation. The second is that a cleaning procedure for the removal of graphitic byproducts is not required, because NDs form on the surface and are not embedded in a graphite matrix, as in the graphite ablation case.

4.5 Conclusions

In this chapter, we have provided the experimental confirmation that NDs can be synthesized through pulsed laser ablation of a non-diamond carbon material in water. In particular, both graphite and DLC were used. Diamond phase usually requires extreme values of temperature and pressure to be formed: the technique used here is very convenient, as it enables formation of diamond phase performing the process at room temperature and standard pressure conditions. Moreover, a non-hazardous liquid-phase purification process for removal of non-diamond carbons atoms embedding the NDs is described. Usual NDs cleaning process involve the use of harsh chemical conditions and dangerous acidic environment. In our case, the cleaning procedure is more viable, but maintaining the advantages of the liquid-phase purification techniques, namely the high density of the oxidizer. Then, NDs production by laser irradiation of DLC film is demonstrated. The advantages of using this particular material as target are described. In particular, the ND formation occurs by laser melting of the target, rather than by explosive ablation. In addition, a cleaning procedure for the removal of graphitic byproducts is not required, as NDs form on the surface and are not embedded in a graphite matrix - as in the graphite ablation case. Finally, a thermodynamic model explaining the formation process of NDs upon ablation of graphite is provided. The differences in the thermodynamic path leading to NDs by using DLC instead of graphite are also highlighted. This thermodynamic model is of great important for this

thesis, as it will be adapted in the following chapters to describe NDs formation during laser ablation of graphite in different environment. Summarizing, in this chapter we have demonstrated that pulsed laser ablation is a suitable method for NDs synthesis. Moreover, this technique allows to overcome the main drawbacks of standard NDs production methods, namely HPHT and detonation. Indeed, as extensively described in Chapter 3.2, high-quality NDs (in term of shape and size distribution) produced through those techniques require severe post-synthesis treatments such as milling, to narrow the size distribution of the nanoparticles, and consequent cleaning in strong acidic environment. In the following part of this thesis we applied PLA of graphite for the production of NDs enriched with nitrogen-vacancy centers.

References for chapter 4

- [1] V.Y. Dolmatov, *Russ. Chem. Rev.* 70, 607 (2001)
- [2] Q. Zhang, V.N. Mochalin, I. Neitzel, I.Y. Knoke, J. Han, C.A. Klug, J.G. Zhou, P.I. Lelkes, Y. Gogotsi, *Biomaterials* 32, 87 (2011)
- [3] E.K. Chow, X.Q. Zhang, M. Chen, R. Lam, E. Robinson, H. Huang, D. Schaffer, E. Osawa, A. Goga, D. Ho, *Sci. Transl. Med.* 3, 73ra21 (2011)
- [4] X.D. Ren, R. Liu, L.M. Zheng, Y.P. Ren, Z.Z. Hu, H. He, *Appl. Phys. Lett.* 107, 141907 (2015)
- [5] A.M. Schrand, S.A.C. Hens, O.A. Shenderova, *Crit. Rev. Solid State Mater. Sci.* 34, 18 (2009)
- [6] D.S. Knight, W.B. White, *J. Mater. Res.* 4, 385 (1989)
- [7] S.K. Sharma, H.K. Mao, P.M. Bell, J.A. Xu, *J. Raman Spectrosc.* 16, 350 (1985)
- [8] E.D. Obraztsova, M. Fujii, S. Hayashi, V.L. Kuznetsov, Y.V. Butenko, A.L. Chuvilin, *Carbon* 36, 821 (1998)
- [9] X.D. Ren, H.M. Yang, L.M. Zheng, S.Q. Yuan, S.X. Tang, N.F. Ren, S.D. Xu, *Appl. Phys. Lett.* 105, 021908 (2014)
- [10] A.C. Ferrari, J. Robertson, *Phys. Rev. B* 61, 14095 (2000)
- [11] M. Bonelli, A.C. Ferrari, A. Fioravanti, A. Li Bassi, A. Miotello, P.M. Ossi, *Eur. Phys. J. B* 25, 269 (2002)
- [12] P. Mosaner, M. Bonelli, A. Miotello, *Appl. Surf. Sci.* 208, 561 (2003)
- [13] D. Amans, M. Diouf, J. Lam, G. Ledoux, C. Dujardin, *J. Colloid Interface Sci* 489, 114 (2017)

BIBLIOGRAPHY

- [14] J.A. Viecelli, S. Bastea, J.N. Glosli, F.H. Ree, *J. Chem. Phys.* 115, 2730 (2001)
- [15] D. Kraus, A. Ravasio, M. Gauthier, D.O. Gericke, J. Vorberger, S. Frydrych, J. Helfrich, L.B. Fletcher, G. Schaumann, B. Nagler, B. Barbrel, B. Bachmann, E.J. Gamboa, S. Goede, E. Granados, G. Gregori, H.J. Lee, P. Neumayer, W. Schumaker, T. Doeppner, R.W. Falcone, S.H. Glenzer, M. Roth, *Nat. Commun.* 7, 10970 (2016)
- [16] F. Gorrini, M. Cazzanelli, N. Bazzanella, R. Edla, M. Gemmi, V. Cappello, J. David, C. Dorigoni, A. Bifone, A. Miotello, *Sci. Rep.* 6, 35244 (2016)
- [17] R. Fabbro, J. Fournier, P. Ballard, D. Devaux, J. Virmont, *J. Appl. Phys.* 68, 775 (1990)
- [18] T. Sakka, K. Saito, Y.H. Ogata, *Appl. Surf. Sci.* 197, 246 (2002)
- [19] A. Mazzi, F. Gorrini, A. Miotello, *Phys. Rev. E* 92, 031301 (2015)
- [20] A.A. Ionin, S.I. Kudryashov, L.V. Seleznev, *Phys. Rev. E* 82, 016404 (2010)
- [21] J. Lam, V. Motto-Ros, D. Misiak, C. Dujardin, G. Ledoux, D. Amans, *Spectrochim. Acta Part B Atom. Spectrosc.* 101, 86 (2014)
- [22] J. Narayan, A. Bhaumik, *APL Mater.* 3, 100702 (2015)
- [23] A. Yu. Basharin, V. S. Dozhdikov, A. V. Kirillin, M. A. Turchaninov, L. R. Fokin, *Tech. Phys. Lett.* 36, 559 (2010)
- [24] L. Berthe, R. Fabbro, P. Peyre, L. Tollier, E. Bartnicki, *J. Appl. Phys.* 82, 2826 (1997)
- [25] A.C. Ferrari, J. Robertson, *Philos. Trans. R. Soc. Lond. A* 362, 2477 (2004)

Chapter 5

Pulsed laser deposition of NV-fluorescent nanodiamonds

In this chapter, we describe the synthesis of fluorescent nanodiamonds (NDs) through pulsed laser ablation of graphite in a controlled nitrogen atmosphere, to obtain nitrogen vacancy (NV) centers in the forming NDs. We demonstrate that by adjusting the experimental ablation conditions, this synthesis route yields fluorescent NDs with a controlled concentration of native NV centers. Compared to standard NV-enriched synthesis methods - widely described in Chapter 3 - the main advantage provided by laser-synthesis is being a single-step, all-optical and low-temperature ($< 100^{\circ}\text{C}$) process. Strong evidence of negatively charged NV centers presence in as-grown NDs is provided by observation of the spin-dependent optical-transitions through Optically Detected Magnetic Resonance (ODMR) spectroscopy. Finally, the thermodynamic model developed in Chapter 4, is adapted to describe NDs formation in nitrogen atmosphere and to explain NV centers presence in the NDs.

The content of this chapter is adapted from:

L. Basso, F. Gorrini, M. Cazzanelli, N. Bazzanella, A. Bifone and A. Miotello, An all optical single-step process for production of nanometric-sized fluorescent diamonds, *Nanoscale* **10** (2018) 5738-5744

DOI: [10.1039/c7nr08791h](https://doi.org/10.1039/c7nr08791h)

© The Royal Society of Chemistry 2018. All rights reserved.

5.1 Introduction

For the development of the many fluorescent NDs applications (see Chapter 3), an efficient synthesis of NDs allowing control in the size distribution and in the concentration of NV^- centers is critical. As demonstrated in chapter 4, pulsed-laser ablation of carbon target is a suitable technique for NDs synthesis [1], enabling tailoring of the NDs' size [2]. Furthermore, fluorescent nanodiamonds (FNDs) were also obtained recently [3] by synthesis of NV^- doped NDs by pulsed-laser irradiation of carbon target. In details, nanosecond-pulsed laser irradiation of a nitrogen-doped carbon substrate at ambient conditions was used to obtain fluorescent NDs. The process leading to nucleation of a variety of micro- and nano-structures is supposed to be the melting of the substrate and rapid quenching. In any case, a number of important challenges still remain with current production methods, including control of NDs shape and size and control of NV^- centers concentration and charge state, etc. In this chapter our findings on a single-step, all-optical FNDs production method are reported. The synthesis process is based on the laser ablation of a pyrolytic graphite target in nitrogen atmosphere. The laser-irradiation performed in a nitrogen-containing medium allows nitrogen incorporation during the very same ablation process. The resulting sample is made by diamonds with nanometric size distribution (10-100 nm), embedded in a biocompatible [4] diamond-like carbon (DLC) matrix, showing intense native photoluminescence (PL) without the need of post-synthesis thermal activation or additional procedures. In the first section 5.2 the description of the experimental setup used for laser ablation is reported. It consists on the standard pulsed laser deposition (PLD) apparatus, where ablation occurs in a vacuum chamber filled with a controlled atmosphere. Then, the characterization techniques used are listed, both regarding NDs and NV^- centers optical properties. For the latter in particular, PL spectroscopy, PL imaging and Optically Detected Magnetic Resonance (ODMR) spectroscopy are used. In section 5.2, the experimental results are discussed. The sample is fully characterized and the presence of negatively charged NV^- centers in the as-grown NDs is unambiguously proven by ODMR. Then, in section 5.4, ODMR spectroscopy is used to study the effects of native strain field acting on the NDs. This measurements is used to obtain an estimation on NDs crystal size. Finally, to explain the graphite-liquid-diamond route enabling the formation of NDs and lattice NV^- point defects under laser ablation of graphite substrate in nitrogen atmosphere, we also provide an extension of the thermodynamic model developed in Chapter 4.

5.2 Experimental methods

5.2.1 Pulsed laser deposition

The experimental apparatus used for NDs synthesis is presented in Fig. 5.1(a). It is the usual setup for PLD experiments, where the target of laser ablation is inside a vacuum chamber. In our case, the target is pyrolytic graphite and the vacuum chamber is operated under high vacuum conditions, to a residual pressure in the order of 10^{-4} Pa. The ablation of graphite is then performed either in a controlled N_2 atmosphere or in vacuum. N_2 is fluxed to the chamber through a fluxmeter to attain a specific partial pressure. Different conditions were tested, of $1.6 \cdot 10^{-4}$, $1.1 \cdot 10^{-2}$, 1.1 and 12 Pa of nitrogen. The vacuum chamber is equipped with a quartz UV-transparent window, to allow the laser beam to reach the target: the ablation is then performed with the KrF excimer laser described in Chapter 4. The laser beam impinges on the target surface with an incident angle of 45° , and it is focused (with a 40cm-focal UV-lens) to a spot size of $\sim 1 \text{ mm}^2$. Power density of the laser beam is $1.1 \pm 0.2 \text{ GW/cm}^2$ per pulse. A silicon substrate, over which the ablated material gets deposited, is positioned in front of the graphite target at a distance of 10 cm. The cleaning procedure of the silicon substrates includes three subsequent ultrasonic baths in ultrapure acetone, ethanol and deionized water, for 10 min each. The substrate is then dried with gaseous nitrogen flux. The silicon substrate is mounted on a heated holder, whose temperature is kept at $\sim 100^\circ\text{C}$ during deposition. After that, the film is annealed in vacuum at 300°C for 1 h, in order to reduce the internal stress of the film and avoid delamination.

5.2.2 Sample characterization

Scanning electron microscopy (SEM) analysis is performed with the microscope described in the previous chapter in the same configuration (20 keV energy beam and 10 mm of Working Distance). The Raman analysis is performed with a Jobin-Yvon Horiba LabRam Aramis confocal micro-Raman system. Two excitation sources are used: a He-Ne laser (633 nm) and a DPSS laser (532 nm). The instrument is operated with the following conditions: confocal hole dimension of $1000 \mu\text{m}$, slit width of $100 \mu\text{m}$ and a 1800 lines/mm grating. The signal is collected with an air-cooled multichannel CCD in the range between 450 nm and 850 nm, with a wavenumber accuracy of $\pm 1 \text{ cm}^{-1}$. The PL spectrum is measured with the same instrument in the same configuration.

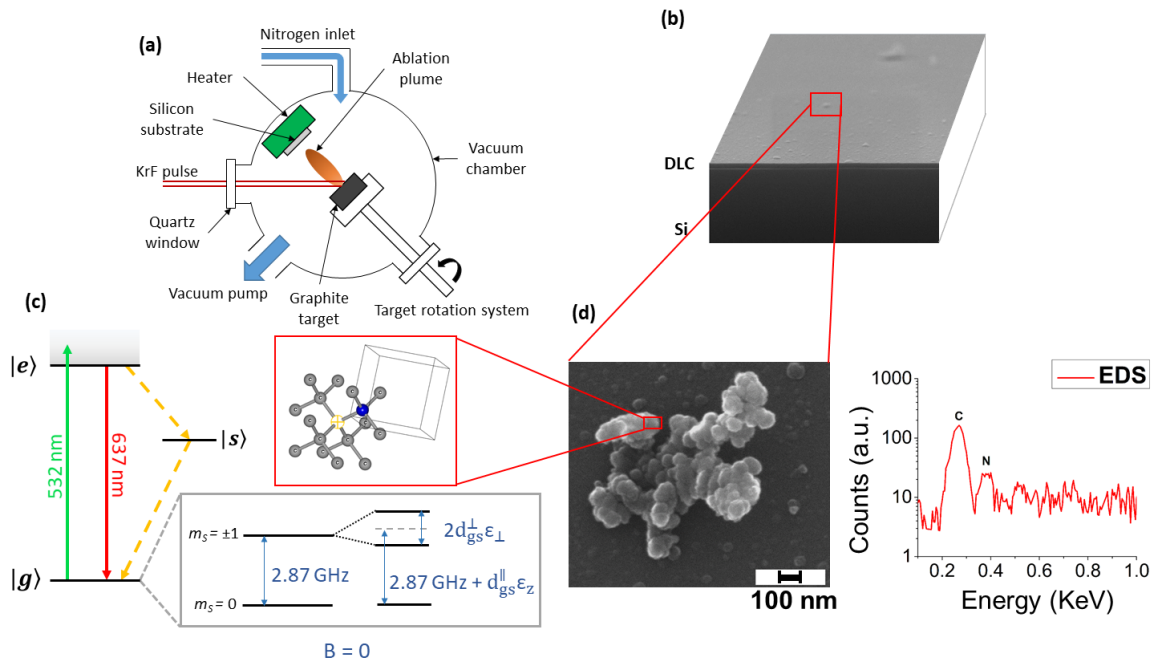


Fig. 5.1: **NDs production technique and N-doping.** (a) PLD experimental setup. (b) SEM image of the synthesized sample: on the Si substrate a thin DLC film is deposited over which NDs are dispersed. (c) NV⁻ center energy levels. When the NV is excited by using a green laser (green arrow), it can relax either radiatively (red arrow) or non-radiative (yellow dotted arrow). The effect of the lattice strain, both its parallel and perpendicular component respect to the NV axis, on the degenerate $m_s = \pm 1$ spin states is represented (see text for details). In the red box: scheme of diamond crystal structure with a NV center, consisting in nitrogen atom (blue sphere) and a nearest-neighbor carbon-vacancy (yellow circle) along the [111] direction. (d) Left-hand side: SEM image of one microparticle deposited on the DLC film, consisting of clustered C-nanoparticles with sizes below 50 nm. Right-hand side: corresponding EDXS spectrum. The carbon and nitrogen peaks are detected at respectively 0.27 and 0.38 KeV, indicating that the nitrogen is contained inside the nanoparticles' cluster. In addition, the silicon peak from the Si substrate was detected at 1.74 KeV (not shown).

ODMR spectra are obtained with a ODMR wide-field microscope, that was developed by modifying an existing Nikon Ti-E inverted wide-field microscope. Wide-field imaging is performed with a 40X (working distance = 0.66 mm and NA = 0.75) refractive objective. The excitation source is a 532 nm CW laser (CNI laser mod. MGL-III-532/50mW), delivering on the sample a power of 20 mW. To avoid that the backscattered light reaches the CMOS detector (ORCA-Flash4.0 V2), the microscope is equipped a modified TRITC (Tetramethylrhodamine) dichroic beamsplitter, that is adapted to the relatively high power delivered by the laser. The microwave (MW) field source is a WindFreak RF generator (SynthHD v1.4 54MHz-13.6GHz) followed by a Mini-Circuits ZVE-3W-83+2W RF amplifier. The MW irradiation is delivered on the sample with a homemade Au-coated copper loop terminated with a high power MW dumper. The MW field is swept in the 2.85-2.90 GHz with constant power of 500 mW. The temporal sequence of the experiment is obtained suitably programming a SpinCore 100 MHz TTL generator (Mod. TTL: PB12-100-4K). Image acquisition is done with the Nikon NIS-Elements Advanced Research software.

5.3 Results and discussion

5.3.1 NDs synthesis and characterization

A DLC film deposited on the silicon substrate following laser irradiation of the pyrolytic graphite target, as it can be seen in Fig. 5.1(b). For laser energy densities around 7 J/cm², the DLC thin film (tens of nm thick) has an high amount of sp³ carbon atoms [6]. No major differences in the content of sp³ bonded carbon atoms were observed above this laser fluence [6]. The building blocks of NDs formation are the liquid carbon nanodroplets expelled from the target during the laser induced phase explosion process that are rapidly cooled down on the silicon target (see discussion below). The micrometer-sized clusters of NDs are shown in the SEM image on Fig. 5.1(d). EDXS analysis shows a prominent nitrogen peak (Fig. 5.1(d)), confirming the presence of nitrogen inside the nanoparticles' clusters. To understand if nitrogen doping of the NDs (the involved atomic processes for nitrogen incorporation are discussed below) brings to the formation of the NV⁻ centers, their fluorescence properties are studied. The PL spectra of the films under 532 nm laser irradiation are presented in Fig. 5.2(b). A broad and bright red emission is observed under continuous-wave (CW)

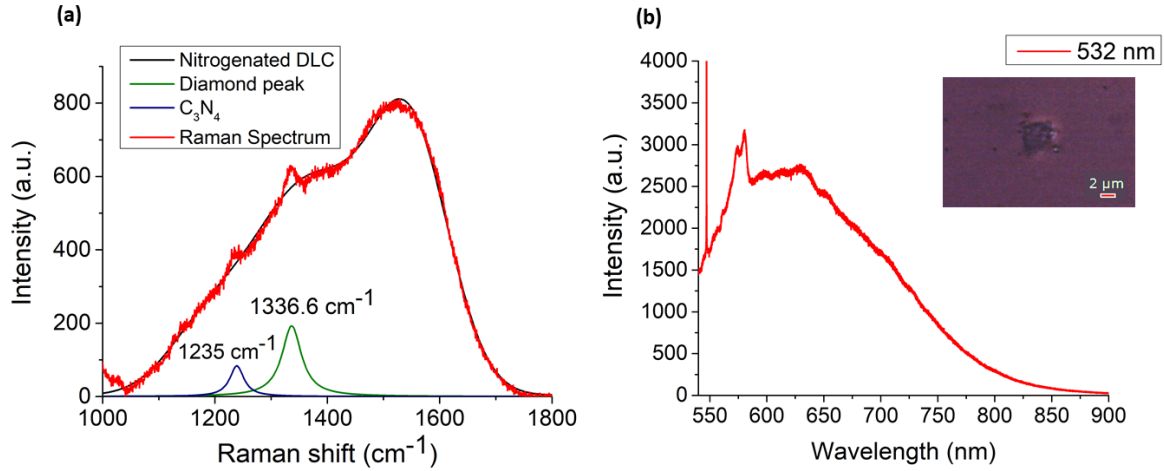


Fig. 5.2: **Micro-Raman and micro-photoluminescence spectra of the nanodiamonds.** (a) Raman spectrum of a NDs cluster obtained with a 633 nm excitation wavelength. The broad band is the typical spectrum of the nitrogenated DLC film (black curve) [8] whereas the peak at about 1235 cm^{-1} (blue Lorentzian) is related to presence of graphitic carbon nitride $g\text{-C}_3\text{N}_3$. Presence of diamond phase is confirmed by the Raman peak at 1336.6 cm^{-1} (green Lorentzian) is attributed to compressively-strained NDs [5]. (b) PL spectrum of a NDs cluster, under 532 nm laser pumping. The narrow peak at 547 nm (corresponding to a Raman shift of $\sim 520\text{ cm}^{-1}$) is the first order Raman of silicon while the couple of peaks at 574 and 580 nm (corresponding to 1375 and 1555 cm^{-1} respectively) are the Raman signals from the DLC film. More interestingly, the bell-shaped PL centered at around 615 nm arises from the presence of NV^- centers in NDs embedded in a sp^2 -carbon shell. The inset shows the bright-field image of the NDs' cluster where the PL is measured. Both spectra (a) and (b) refer to the sample prepared at 1 Pa nitrogen pressure.

532 nm laser pumping. This particular emission is compatible with NV^- fluorescence where the slightly unusual spectral tails can be explained with residual sp^2 hybridized optically-active states [7]. This observation suggests the presence of a graphite layer on the surface of deposited NDs, as already observed in HPHT NDs [9] and detonation NDs [7]. The sharp peak in the micro-PL spectrum at $< 550\text{ nm}$ is the Raman signal of the silicon substrate, while the other two peaks, at around 575 nm, are the Raman peaks of the DLC surrounding matrix. The microRaman spectrum of the same NDs cluster is reported in Fig. 5.2(a). This spectrum is obtained with a 633 nm laser pump, to reduce the strong PL emission and obtain a better measure of the Raman signal. Superimposed to the typical broad feature of nitrogenated DLC (black curve), the NDs peak arises at 1336 cm^{-1} . Its position is blue-shifted from the usual bulk diamond 1332.5 cm^{-1} Raman shift, due to the compressive strain acting of the NDs. The Raman peak width

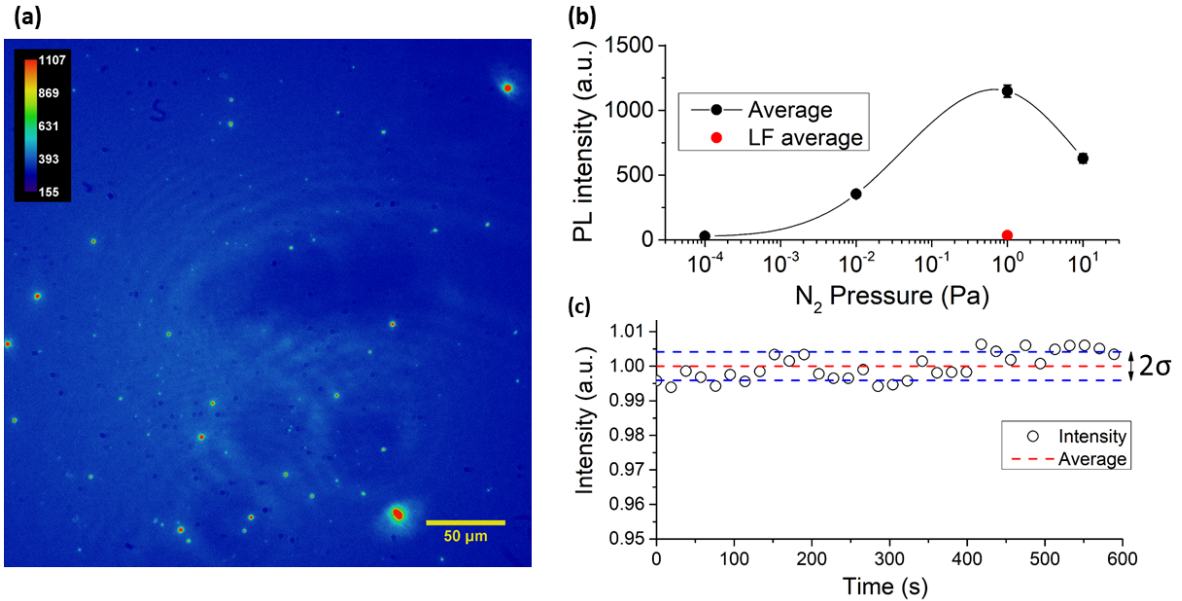


Fig. 5.3: **Wide field imaging and N₂ pressure-dependence of the PL signal.** (a) PL image of the sample deposited with a nitrogen pressure of 1 Pa, presented in pseudo-colors proportional to the PL intensity. The blue background is the optically inert DLC film, while the bright spots correspond to the NV-centers emissions. (b) PL intensity as function of nitrogen pressure inside the vacuum chamber during deposition. The black circles are the experimental values whereas the black line is a guide for the eye. The red circle is the PL intensity to the sample deposited at low laser fluence of 1.6 J/cm², used to prove our model for NDs formation. (c) PL stability measurement, showing the PL level as function of time (empty circles). The mean value (dashed red lines) and the 2σ interval (dashed blue lines) are also plotted.

(FWHM = 22 ± 1 cm⁻¹) indicates that the NDs have a low degree of amorphization [5]. The results concerning PL imaging are reported in Fig. 5.3(a), where a typical PL image - with sub-micron spatial resolution - of the emission from NDs dispersed on the DLC film is observed. PL imaging is used to study the effect of nitrogen pressure in the chamber during deposition on the final PL intensity of the sample, or in other words on the FNDs production efficiency. Indeed, NDs produced under different pressures of N₂ atmosphere ($1.6 \cdot 10^{-4}$, $1.1 \cdot 10^{-2}$, 1.1, and 12 Pa) show different level of PL. This is observed in Fig. 5.3(b), where total PL intensity of each sample is reported as function of the N₂ pressure. As one can observe, the PL increases with increasing the N₂ pressure, but non monotonically: above a certain pressure, the PL signal drops. This is likely due to the influence of nitrogen on the NDs chemical composition, no longer behaving as a dilute dopant. The PL level reported in Fig. 5.3(b) is obtained by averaging the total intensity (obtained by integration of the whole picture) of a series

of PL images (as the one of Fig. 5.3(a)). Furthermore a PL stability measurement has been performed to check the quality of the emission. Under continuous 532 nm laser excitation, the PL emission is collected over a ten min timescale. The result is reported in Fig. 5.3(c), where the normalized PL intensity is shown together with its mean value (dashed red line), and the relative 2σ interval (dashed blue lines), with $\sigma = 0.004$ being the standard deviation. The sample present excellent PL emission stability: on a 10 min timescale, all data points are within a $\pm 1\%$ range from the mean value, testimony of the optical quality of the FNDs. Finally, the unequivocal proof of NV-centers formation in the NDs is obtained through spatially-resolved optically detected magnetic resonance (ODMR), a technique widely described in Chapter 2 of this thesis. When NV^- centers are irradiated with a MW field resonant with the 2.87 GHz ground-state energetic sublevels separation, an inter-system crossing process appears (see Fig. 5.1(c)) providing an additional non-radiative recombination channel, resulting in a significant decrease of the fluorescence signal. The observation of this resonance, characterized by a PL decrease, is a fingerprint of NV^- centers presence in the NDs. Specifically, we use a wide-field inverted fluorescence microscope (Fig. 5.4(a)) operated in continuous wave electron spin resonance (CW-ESR) mode [10]. The temporal scheme of a CW-ESR experiment is reported in Fig. 5.4(b). This instrument detects the spatially-resolved fluorescence signal, with sub-micrometric lateral resolution, while simultaneously irradiating the sample with a microwave field whose frequency is swept in the range 2.85-2.90 GHz (see the Experimental paragraph for additional details). For each discrete value of MW frequencies a spatially-resolved PL image is collected (Fig. 5.4(c)). Then, ODMR curves are extracted from regions of interest (ROIs) containing the bright spots. The experimental curves, labelled d1, d2 and d3 in Fig. 5.4(d), show the ODMR dips of strained-NDs NV^- centers at 2.87 GHz, corresponding to the transition between the $|0\rangle$ and $|\pm 1\rangle$ spin states in the 3A_1 ground state $|g\rangle$ of NV^- centers (see Fig. 5.1(c)). These spectra demonstrate that the fluorescence originates from negatively charged NV^- defects in the NDs [11]. The different splitting between the two dips in the ODMR spectra is a consequence of different native strain fields acting on the crystal structure hosting the NV centers. Thus, the ODMR spectra can provide information about such fields. This native strain field is likely related to surface-compressive strain effects emerging at such small particle size. In the following section ODMR is used to measure this strain field, which in turn is used to estimate NDs dimension.

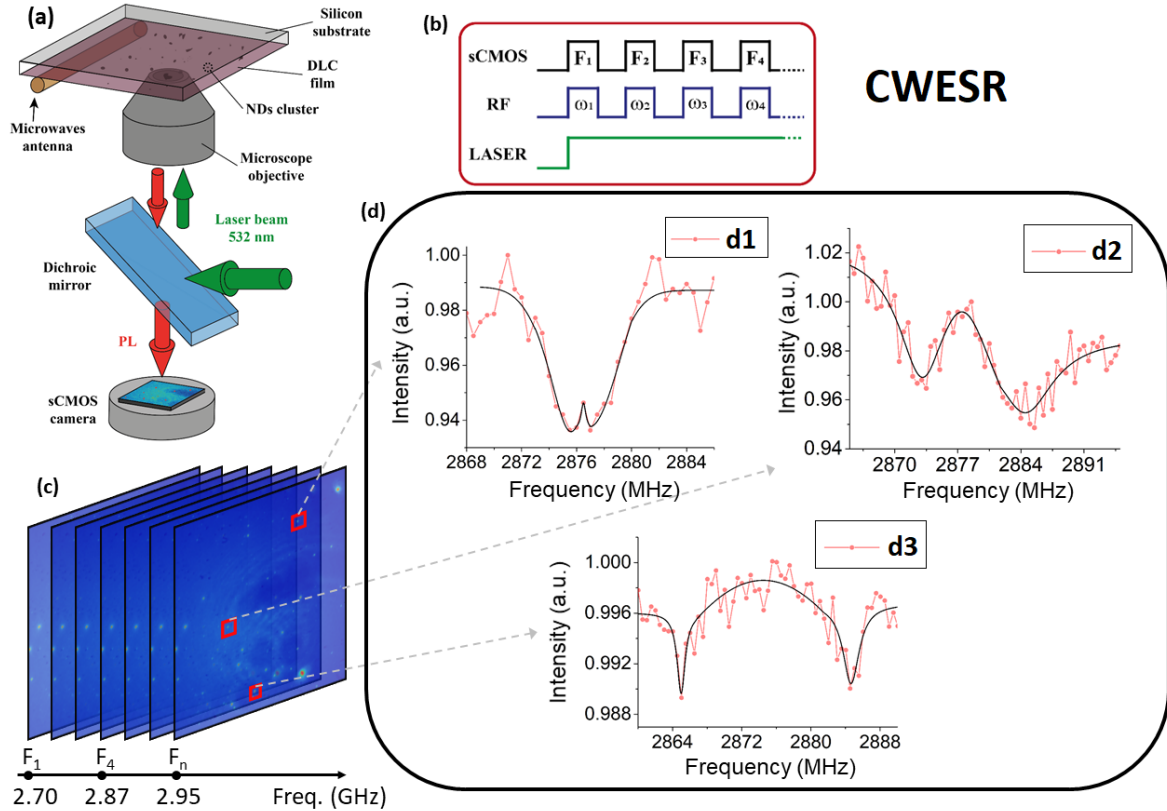


Fig. 5.4: **Spatially resolved ODMR wide field imaging and strain field dependence.** Panel (a): Schematics of the inverted wide-field ODMR microscope. The green laser is reflected onto the sample and focused through the 40X objective through a dichroic mirror. The same mirror then allows only the transmission of the red PL to the CMOS detector. The RF irradiation is obtained with an Au-coated copper loop, here represented by the yellow wire below the sample's surface. Panel (b): temporal diagram of the continuous wave electron spin resonance (CW-ESR) experiment. The laser is kept ON all along the measurement, while the camera detects the PL image synchronously with the RF irradiation. Panel (c) PL images as the RF frequency sweeps in the 2.85-2.90 GHz range. A ROI (red square) containing a bright spot is selected and the average intensity inside that very ROI is plotted as a function of the RF frequency to generate an ODMR spectrum. Panel (d) reports three typical examples of NDs signal showing different strain effects (curves d1, d2, and d3).

5.4 Sensing of nanodiamonds native strain field with NV centers

To study the effect of the strain field on the NV^- energy levels, the Hamiltonian of the system must be studied. The NV-center ground state fine structure is described by the spin-Hamiltonian [12]:

$$H_{gs} = D_{gs}[S_z^2 - S(S+1)/3] + V_{gs} \quad (5.1)$$

where $D_{gs} = 2.87$ GHz is the zero field-splitting between $m_s = 0$ and $m_s = \pm 1$ states, S_z is the component of the spin operator S along the z-axis parallel to the NV^- axis and $S = 1$ is the modulus of \vec{S} . The interaction of the NV center with a bi-axial strain field $\vec{\varepsilon}$, that is given by the in-plane compressive surface stresses, is accounted in the term V_{gs} :

$$V_{gs} = d_{gs}^{\parallel} \varepsilon_z [S_z^2 - S(S+1)/3] + d_{gs}^{\perp} \varepsilon_x (S_y^2 - S_x^2) + d_{gs}^{\perp} \varepsilon_y (S_x S_y + S_y S_x) \quad (5.2)$$

Here, S_x (ε_x) and S_y (ε_y) are, respectively, the x and y components, i.e. perpendicular to S_z (ε_z) and to the NV axis, of \vec{S} ($\vec{\varepsilon}$). The terms $d_{gs}^{\parallel} = 5.5 \pm 0.3$ GHz and $d_{gs}^{\perp} = 19.6 \pm 0.4$ GHz [13] are the parallel and perpendicular components, with respect to the NV^- axis of the so-called ground-state strain-coupling constants. Eq. 5.2 is valid in the absence of external electric or magnetic fields: this assumption in our case is justified as we worked at Earth Field conditions. The positions of the two minima of the ODMR spectrum are then given by [14]:

$$\nu_{\pm} = D_{gs} + d_{gs}^{\parallel} \varepsilon_z \pm d_{gs}^{\perp} \varepsilon_{\perp} \quad (5.3)$$

from which the non-axial $\varepsilon_{\perp} = \sqrt{\varepsilon_x^2 + \varepsilon_y^2}$ and the axial ε_z components of the strain field $\vec{\varepsilon}$ can be calculated. As apparent from Eq. 5.3 and from Fig. 5.1(c), the non-axial component of the strain ε_{\perp} brings to the removal of the degeneracy between the $m_s = \pm 1$ states, leading to a linear split of the two dips in the ODMR spectra, whereas the presence of a z-component of the strain ε_z affects equally the $m_s = \pm 1$ states, causing a shift with respect to D_{gs} . Finally, the hydrostatic strain ε_H^{ODMR} , defined as the mean value of the two components, can be calculated. The results are reported in Table 5.1. As expected, the sample having the shorter frequency-difference between the two ODMR

	Fig. 5.1(d1)	Fig. 5.1(d2)	Fig. 5.1(d3)
ODMR			
ε_z	$(1.2 \pm 0.1) \cdot 10^{-3}$	$(2.8 \pm 0.2) \cdot 10^{-3}$	$(8.2 \pm 0.8) \cdot 10^{-4}$
ε_{\perp}	$(3.8 \pm 0.9) \cdot 10^{-5}$	$(3.2 \pm 0.1) \cdot 10^{-4}$	$(5.0 \pm 0.1) \cdot 10^{-4}$
ε_H^{ODMR}	$(6.1 \pm 0.5) \cdot 10^{-4}$	$(1.6 \pm 0.1) \cdot 10^{-3}$	$(6.6 \pm 0.4) \cdot 10^{-4}$
D (nm)	30 ± 3	11 ± 1	27 ± 2
Raman			
ε_H^R	Fig. 5.2(a)		
ε_H^R	$(9.1 \pm 0.5) \cdot 10^{-4}$		
D (nm)	20 ± 2		

Table 5.1: **Strain measurement and NDs size estimation.** Top part of the Table: **ODMR.** Strain and size obtained from the ODMR spectra. The columns indicate the sample of Fig. 5.4(d): for each one the strain was calculated. The rows labelled as ε_z and ε_{\perp} refer to the strain components parallel and perpendicular to the NV axis, and are extracted from Eq. 5.3. The error bars are given by conveniently propagating the uncertainties of the d_{gs}^{\parallel} and d_{gs}^{\perp} parameters (tabulated in reference [13]). The row ε_H^{ODMR} reports the hydrostatic strain, that is the average of the two components ε_z and ε_{\perp} , which uncertainties are obtained through error propagation. The last row gives the diameter D of the NDs calculated through Eq. 5.5 starting from the strain values ε_H^{ODMR} . In this case the error bars are obtained by usual propagation of ε_H^{ODMR} and κ uncertainties. Bottom part of the Table: **Raman.** The result for the hydrostatic strain ε_H^R obtained via Raman spectroscopy (Fig. 5.2(a)) is reported, together with the estimation of NDs diameter D. The error bar of the strain value is obtained after standard propagation of the errors of the parameters in Eq. 5.4. α is taken from the literature [16], and the error in the position of the Raman peak at $\Delta\omega_H$ is given by the best fit of its Lorentzian lineshape.

dips (Fig. 5.4(d3)) presents the smaller non-axial ε_{\perp} strain component. This value increases together with the ODMR resonances splitting. On the other hand, the axial ε_z component depends on the orientation of the NV^- axis with respect to the plane identified by the DLC film surface. The strain values reported in Table 5.1 are obtained considering only the fine structure of the ground state (Equation 5.1), while in some works also the hyperfine structure - given by the interaction with the ^{14}N nuclear spin - is used [14]. For comparison, the total hydrostatic strain can also be extracted from the microRaman spectrum (Fig. 5.2(a)) through [15]:

$$\Delta\omega_H = -3\omega_0\alpha\varepsilon_H^R \quad (5.4)$$

where $\Delta\omega_H = 4.1 \pm 0.2 \text{ cm}^{-1}$ is the shift of the Raman peak of diamond with respect to the first order Raman line at $\omega_0 = 1332.5 \text{ cm}^{-1}$, ε_H^R is the compressive hydrostatic strain and $\alpha = 1.12$ is the Grüneisen parameter [16]. The minus sign in Eq. 5.4 leads to negative strain values, namely compressive strain according to convention. Here only the modulus is reported for the sake of simplicity. The value of ε_H^R , given in Table 5.1, is comparable to the set of hydrostatic strain values extracted from ODMR spectra. Finally, the measured native strain fields ε can be used to estimate NDs size. Indeed, due to a high surface to volume ratio, NDs surface tension brings to size-dependent compressive surface stress. This in turn leads to a reduction of the effective lattice parameter, namely to a shrink of the NDs' shape. Quantitatively, considering a spherical nanoparticle and starting from the Young-Laplace equation, the relation between particle size and lattice contraction is given by [17]:

$$\varepsilon = \frac{a - a_0}{a} = -\frac{2\gamma}{3\kappa R} \quad (5.5)$$

where a and a_0 are the nanoparticle and bulk lattice parameter, γ is the surface tension, κ is the bulk compression modulus and R is the radius of the strained nanoparticle. Again, the minus sign indicates the compressive nature of the strain. For simplicity, the surface tension is supposed to be size-independent (which is true for $R > 1 \text{ nm}$ [17]), and the value of bulk diamond $\gamma = 3.7 \text{ J m}^{-2}$ [18] is used. The compression modulus κ for nanocrystalline diamond used here is $\kappa = 271 \pm 15 \text{ GPa}$ [19]. The results for NDs size, calculated through Eq. 5.5, are listed in Table 5.1. Both the ODMR- and Raman-calculated hydrodynamic strain values are used to estimate NDs size: the results obtained are self-consistent. Remarkably, NDs size estimation is comparable with SEM observation (see Fig. 5.1(d)). The minor differences with SEM analysis can be explained as follows. The ODMR and Raman signals originate from crystalline NDs, while the SEM images refer to the overall NDs cluster, also including the non-crystalline portion of the nanostructures, such as the residual graphitic shell around the NDs.

5.5 Modeling of nanodiamond formation mechanism

In this section, to explain FNDs formation, we adapt the thermodynamic model, used for NDs synthesis upon laser ablation of graphite in water, developed in Chapter 4. In addition, NDs size is estimated through the equations of classical nucleation theory.

As we will see, theoretical estimation of NDs dimension matches the experimental observations. Concerning NDs synthesis, we have to consider the aspects of the laser ablation related to the phase explosion [20–22]. Firstly, the state of the ablated material must be addressed. This is done to check whether liquid phase, which is an essential step for NDs formation in our model, is obtained. The pressure on the target reached upon pulsed laser irradiation in a low-pressure vapor can be estimated following the works of Knight [23] and Anisimov [24]. The recoil pressure exerted by the fast ablated material on the vaporizing surface is given by $p_{rec} \approx \rho_v v_v^2$, where ρ_v is the vapor density and v_v the flow velocity. For a sonic flow, $\rho_v = 0.31\rho_s$, with ρ_s being the saturated vapor density, while $v_v = \sqrt{\frac{\gamma RT_v}{M}}$, where $M = 12$ g/mol is the molar mass, $\gamma = 5/3$ for a monoatomic gas and the vapor temperature T_v is 0.67 times the surface temperature T_s . When the phase explosion threshold is reached, the surface temperature is close to the critical value (T_c), $T_s = 0.9 T_c \approx 6300$ K [25]. In this condition, the density of the vapor phase is a fraction of 0.12-0.15 the liquid density [22], which is assumed to be ≈ 1.37 g/cm³ for liquid carbon [26]. Thus, $p_{rec} > 200$ MPa, enough to overcome the GLV (Graphite-Liquid-Vapor) triple point pressure at 11 MPa [26, 27]: the system is in the stability region of the liquid phase. This value is in good agreement with the previous observation [28] of $p_{rec} \approx 280$ MPa obtained at a laser intensity of 1 GW/cm². The phase explosion is thought to be the process driving the nanoparticles synthesis [22]. As fully explained in Chapter 3, when the temperature of super-heated liquid lies sufficiently near T_c , the rate of homogeneous nucleation increases dramatically. Then, phase explosion occurs by homogeneous nucleation, resulting in dissociation of the hot region into vapor plus liquid droplets [20]. The radii of the ejected droplets are of the order of magnitude of the critical vapor radius [22] $r_c \approx 2\sigma/\Delta p$, where σ is the surface tension of liquid carbon and Δp the difference between the vapor pressure inside the bubble and the liquid pressure outside. This difference is given by $\Delta p \approx 0.45p_s(T)$, with p_s being the saturated vapor pressure at temperature T . An experimental value for the surface tension of liquid carbon is not available, but it can be estimated with the help of the Guggenheim–Katayama equation [29]:

$$\sigma(T) = K(T_c p_c^2)^{1/3} \left(1 - \frac{T}{T_c}\right)^{11/9} \quad (5.6)$$

where $T_c = 7000$ K and $p_c = 220$ MPa are, respectively, the critical temperature and critical pressure of liquid carbon, and $K \approx 2 \cdot 10^{-7}$ m Pa^(1/3) K^(-1/3) is a universal

constant. At $T = 6300$ K we have $p_s \approx 150$ MPa and $\sigma = 0.084$ N/m. Correspondingly, the critical diameter is $d_c = 5$ nm. At $T = 5500$ K, $p_s \approx 50$ MPa and d_c rises to almost 30 nm. Thus, the calculated size of expelled liquid droplets matches that of the observed particles. This analytical estimate is in good agreement with experimental observation of NDs size, considering both SEM analysis and NDs dimension extracted from ODMR data. The final observed NDs clusters are due to surface agglomeration on the substrate in which nanoparticles deposit, occurring to minimize their Gibbs free energy. Depending on the thermodynamic conditions of solidification, liquid carbon can turn into nano-crystalline graphite, amorphous carbon, and diamond. In this case, due to small size of the deposited liquid nanodroplets compared to the substrate, the cooling rates are very high. Thus an undercooled liquid is obtained: in these conditions the system is brought in the region of diamond stability [5], where the liquid rearranges into a ND structure due to the smaller chemical potential of the diamond phase, with the size playing a relevant role in this phase transition [32, 33]. The last piece of the model is the presence of atomic nitrogen, required for NV centers formation, in the final synthesized NDs. The energy of the atoms, ions (from C^+ to C^{4+}) and electrons leaving the laser ablated target can be higher than 100 eV for the typical laser fluence used [28]. This energy is enough to break the N_2 molecules, having a bond dissociation energy at room temperature of 9.79 eV. Thus, the ablated energetic species can easily break N_2 molecules and single N atoms may be trapped inside the nanodroplets flying from the target to the substrate. The presence of nitrogen was detected in the NDs clusters by inspection with EDXS (Fig. 5.1(d)). The rapid cooling of liquid carbon towards the solid phase favors the NV^- centers formation, as well as, likely, other N-based color centers into the NDs. Summarizing, according to this model, FNDs formation occurs during phase explosion process upon laser ablation of graphite. To prove the formation mechanism of the NDs here proposed, a sample is prepared in a N_2 pressure of 1.1 Pa, but with a low laser fluence, below phase explosion threshold. To avoid liquid nanodroplets emission, the fluence is set to 1.6 J/cm² [28]. The low-fluence sample displays two orders of magnitude decrease in the PL intensity, as shown in Fig. 5.3(b). As the same nitrogen partial pressure is present in the chamber during deposition, the absence of a significant number of NV^- emitters is related to the lack of the NDs, confirming that phase explosion - and consequent liquid carbon nanodroplets emission - is the process responsible for diamond-phase formation.

5.6 Conclusions

In conclusion, in this chapter direct production of NV^- -fluorescent NDs through an all-optical, facile, single-step process is demonstrated. It is based on the pulsed laser ablation of a graphite target in a controlled nitrogen atmosphere. With this technique, diamond phase formation and nitrogen atom incorporation in the nanostructures are obtained in the same process. The produced NDs present a photoluminescence, which does not require any post-synthesis activation process and it is sufficiently bright to be detected and spatially resolved with a wide-field fluorescence microscope. This instrument is also equipped with a MW channel for performing ODMR analysis. The presence of the typical resonances in the zero-field ODMR spectrum at 2.87 GHz, unambiguously demonstrates the negatively charged NV^- centers origin of the red emission from the NDs. Moreover, wide-field ODMR is used to measure the strain field distribution of NDs clusters, giving results in good agreement with the Raman data. Finally, we extended the thermodynamic model, that provides insights into the formation mechanism of the NDs, for the case of ablation of graphite in nitrogen vapor. Moreover, nitrogen atoms incorporation in the NDs, suitably forming optically active NV^- centers, is taken into account. The cheap and easily scalable process we have presented here should provide a facile means for the production of NV^- -doped fluorescent NDs for a number of applications, including quantum-computing, bioimaging and photonics.

References for chapter 5

- [1] G. W. Yang, J. B. Wang, and Q. X. Liu, *J. Phys.: Condens. Matter*, 1998, 10, 7923.
- [2] D. Tan, S. Zhou, B. Xu, P. Chen, Y. Shimotsuma, K. Miura, and J. Qiu, *Carbon*, 2013, 62, 374.
- [3] J. Narayan, and A. Bhaumik, *Mater. Res. Lett.*, 2016, 5, 242.
- [4] G. Dearnaley, and J. H. Arps, *Surf. Coat. Technol.*, 2005, 200, 2518
- [5] F. Gorrini, M. Cazzanelli, N. Bazzanella, R. Edla, M. Gemmi, V. Cappello, J. David, C. Dorigoni, A. Bifone and A. Miotello, *Sci. Rep.*, 2016, 6, 35244.
- [6] M. Bonelli, A. C. Ferrari, A. Fioravanti, A. Li Bassi, A. Miotello and P. M. Ossi, *Eur. Phys. Journ. B*, 2002, 25, 269 .
- [7] C. Bradac, T. Gaebel, N. Naidoo, M.J. Sellars, J. Twamley, L.J. Brown, A.S. Barnard, T. Plakhotnik, A.V. Zvyagin, J.R. Rabeau, *Nature Nanotech.*, 2010, 5, 345.

BIBLIOGRAPHY

- [8] J.R. Shi, X. Shi, Z. Sun, E. Liu, B.K. Tay, and S.P. Lau, *Thin Solid Films*, 2000, 366, 169.
- [9] X. Song, G. Wang, X. Liu, F. Feng, J. Wang, L. Lou, and W. Zhu, *Appl. Phys. Lett.*, 2013, 102, 133109.
- [10] S. Steinert, F. Dolde, P. Neumann, A. Aird, B. Naydenov, G. Balasubramanian, F. Jelezko, and J. Wrachtrup, *Rev. Sci. Inst.*, 2010, 81, 043705.
- [11] N. D. Lai, D. Zheng, F. Jelezko, F. Treussart, and J. F. Roch, *Proc. of Lasers and Electro-Optics 2009 and the European Quantum Electronics Conference. CLEO Europe - EQEC 2009*. doi: 10.1109/CLEOE-EQEC.2009.5191672
- [12] M. W. Doherty, N. B. Manson, P. Delaney, F. Jelezko, J. Wrachtrup, L. C. L. Hollenberg, *Phys. Rep.*, 2013, 528, 1.
- [13] J. Teissier, A. Barfuss, P. Appel, E. Neu, and P. Maletinsky, *Phys. Rev. Lett.*, 2014, 113, 020503.
- [14] A. O. Levchenko, V. V. Vasil'ev, S. A. Zibrov, A. S. Zibrov, A. V. Sivak and I. V. Fedotov., *App. Phys. Lett.*, 2015, 106, 102402.
- [15] E. Liu, L. Li, B. Blanpain, and J. P. Celis, *J. Appl. Phys.*, 2005. 98, 073515.
- [16] M. H. Grimsditch, E. Anastassakis, and M. Cardona, *Phys. Rev. B*, 1978, 18, 901.
- [17] Z. Huang, P. Thomson, and S. Di, *J. Phys. Chem. Solids*, 2007, 68, 530.
- [18] D. Amans, A.-C. Chénus, G. Ledoux, C. Dujardin, C. Reynaud, O. Sublemontier, K. Masenelli-Varlot, O. Guillois, *Diam. Relat. Mater.*, 2009, 18, 177.
- [19] M. Mohr, A. Caron, P. Herbeck-Engel, R. Bennowitz, P. Gluche, K. Brühne, and H.-J. Fecht, *J. Appl. Phys.*, 2014, 116, 124308.
- [20] A. Miotello, and R. Kelly, *Appl. Phys. Lett.*, 1995, 67, 3535.
- [21] L. V. Zhigilei, Z. Lin, and D. S. Ivanov, *J. Phys. Chem. C*, 2009, 113, 11892.
- [22] A. Mazzi, F. Gorrini, and A. Miotello, *Phys. Rev. E*, 2015, 92, 031301.
- [23] C. J. Knight, *AIAA Journal*, 1979, 17, 519-523.
- [24] S. I. Anisimov, *Sov. Phys. JETP*, 1968, 27, 182.
- [25] F. P. Bundy, *Mater. Res. Soc. Symp. Proc.*, 1995, 383, 3.
- [26] D. M. Haaland, *Carbon*, 1976, 14, 357.
- [27] M. Musella, and C. Ronchi, *J. Appl. Phys.*, 1998, 84, 2530.
- [28] A. A. Ionin, S. I. Kudryashov, and L. V. Seleznev, *Phys. Rev. E*, 2010, 82, 016404.
- [29] K. S. Birdi, *Handbook of surface and colloid chemistry*, CRC press LLC, Boca Raton FL, 2009.

- [30] A. Yu. Basharin, V. S. Dozhdikov, A. V. Kirillin, M. A. Turchaninov, and L. R. Fokin, *Tech. Phys. Lett.*, 2010, 36, 559.
- [31] J. Narayan, and A. Bhaumik, *APL Materials*, 2015, 3, 100702.
- [32] N. M. Hwang, J. H. Hahn, and D. Y. Yoon, *J. Cryst. Growth*, 1996, 160, 87.
- [33] Q. Jiang, J. C. Li, and G. Wilde, *J. Phys.: Condens. Matter*, 2000, 12, 5623.

BIBLIOGRAPHY

Chapter 6

NV-enriched nanodiamonds through laser ablation of graphite in liquid nitrogen

In this chapter, the synthesis of nanodiamonds (NDs) containing nitrogen-vacancy (NV) center is achieved by pulsed laser ablation (PLA) of a graphite target immersed in liquid nitrogen. Compared to the standard synthesis of NV-embedded NDs, this represents a relevant development, as there is no need of any post-process activation. Strong experimental evidence of NDs formation is provided by transmission electron microscopy and selected area electron diffraction, whereas optically detected magnetic resonance spectroscopy proves the presence of NV⁻ centers in NDs. Furthermore, to explain diamond-phase formation, the thermodynamic model is adapted to ablation in liquid nitrogen. This model is also used to explain the different observation in the PL intensity between NDs obtained through graphite ablation in liquid nitrogen and in a nitrogen atmosphere (reported in the previous chapter).

The content of this chapter is adapted from:

L. Basso, N. Bazzanella, M. Cazzanelli and A. Miotello, On the route towards a facile fluorescent nanodiamonds laser-synthesis, *Carbon* **153** (2019) 148-155

DOI: <https://doi.org/10.1016/j.carbon.2019.07.025>

© 2019 Elsevier Ltd. All rights reserved.

6.1 Introduction

In Chapter 4 and 5 of this thesis we have demonstrated that physical vapor deposition techniques based on Pulsed Laser Ablation (PLA) of graphitic carbon in different environment, is a feasible route for NDs synthesis [1–4]. In particular, in Chapter 5 the direct synthesis of NV enriched NDs was demonstrated for graphite ablation in controlled nitrogen atmosphere. Herein, our results on a new liquid PLA synthesis technique based on the immersion of the graphitic-carbon precursor in cryogenic liquid nitrogen (LN_2) are reported. With this particular technique by using a simple and cheap experimental apparatus optically-active NDs are produced in a single-step process. In section 6.2 the experimental apparatus and the characterization techniques are described. After that, the experimental results are reported in section 6.3, starting with characterization of the produced NDs. Again, a strong interest is put in the analysis of NDs optical properties; Optically detected magnetic resonance (ODMR) spectroscopy is used to unequivocally prove the presence of NV^- centers formation inside NDs. In this section, the effect of the confining medium are theoretically studied: LN_2 has a double role: 1) the N-doping of the forming NDs; 2) to favor the high-pressure condition and undercooling process that is relevant in the thermodynamic path leading to graphite-liquid-diamond phase transition. Finally, in section 6.4 the fluorescent NDs synthesized through ablation in liquid nitrogen are compared with those obtained in nitrogen atmosphere. The LN_2 synthesized NDs clearly show a higher luminescence intensity and a higher surface purity, the latter assessed by using ODMR spectroscopy. This observation are explained with the thermodynamic model, taking into account the different conditions, namely plume dynamics, in which NDs form. Our theoretical description is then tested with a specific experiment, consisting into the cleaning of the NDs produced in a nitrogen gaseous environment from sp^2 -surface contaminants.

6.2 Pulsed laser ablation in liquid: experimental methods

A schematics of the experimental apparatus for the synthesis of fluorescent NDs is sketched in Fig. 6.1(c). The pyrolytic graphite target is placed in a glass vial, that is filled with liquid nitrogen till the top surface of the target is covered by a ~ 5 mm thick liquid layer. The glass while is in turn placed in a liquid nitrogen bath to limit

6.2. PULSED LASER ABLATION IN LIQUID: EXPERIMENTAL METHODS

the unavoidable liquid nitrogen evaporation. Pulsed laser ablation of the target is then performed with a KrF excimer laser (Lambda-Physik Coherent LPX220i), with the following parameters: wavelength of $\lambda = 248$ nm, pulse duration $\tau = 20$ ns, energy per pulsed of ~ 500 mJ and repetition rate of 10 Hz. The laser beam, that impinges perpendicularly on the target, is focused with a 40 cm-focal length lens to a spot size of ~ 1 mm². Once the ablation is performed, the glass vial is removed from the thermal bath. After full evaporation of liquid nitrogen, the powders are dispersed in ethanol and then deposited on a silicon substrate for characterization. Scanning electron microscopy (SEM) and Energy Dispersive X-ray Spectroscopy (EDXS) are used for morphological and compositional analysis, while Raman spectroscopy to study the crystal structure is employed. Regarding the characterization of the optical properties, PL spectroscopy, wide-field imaging and optically detected magnetic resonance (ODMR) are used. The details of the characterization techniques are reported in Chapter 4 and Chapter 5.

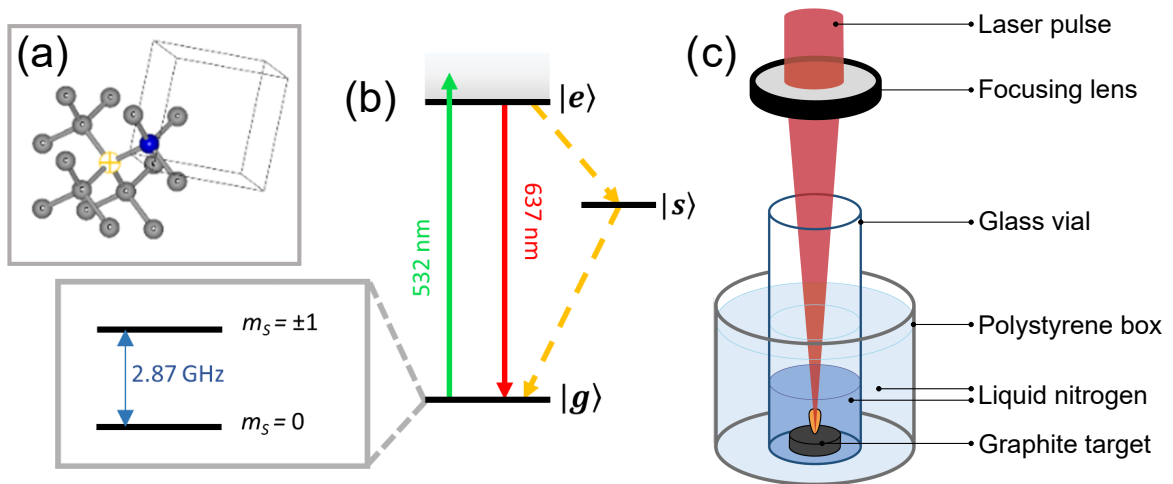


Fig. 6.1: (a) NV center crystal structure: the carbon vacancy and the substitutational nitrogen atom are labeled with the yellow circle and the blue sphere respectively. (b) NV⁻ center energy levels. The radiative (red solid line) and non-radiative relaxation paths (yellow dotted line), the latter achieved through a metastable singlet state $|s\rangle$, are indicated. The spin sublevels m_s of the spin triplet ground state are also reported, with the zero field splitting $D = 2.87$ GHz between the $m_s = 0$ and the two-degenerate $m_s = \pm 1$ (c). Experimental setup for PLA in liquid nitrogen.

6.3 Results and discussion

6.3.1 NDs synthesis and characterization

Fig. 6.2(a) reports the morphological analysis of synthesized sample, in particular showing a scanning electron microscopy (SEM) image of a typical ND nanoparticle having size in the \sim hundreds nm range. EDXS is used to check the absence of contamination in the NDs, which shows the only relevant peak of carbon (Fig. 6.2(b), peak at 0.28 keV). The other peaks arise from the oxygen present in the oxidized surface layers of the sample (0.53 keV), and from the silicon of the substrate (1.74 keV) over which the sample is deposited. Then, Raman analysis, reported in Fig. 6.2(c), is used to assess NDs crystalline quality. Two peaks are detected: the graphitic G peak at ~ 1580 cm^{-1} and the diamond-related sharp peak at 1336 cm^{-1} . With respect to the typical bulk diamond peak position at 1332.5 cm^{-1} , the ND peak is shifted towards higher wavenumbers. This can be interpreted as compressive mechanical strain acting on the NDs [5]. The ND peak also presents a quite large full width half maximum (FWHM) of ~ 62 cm^{-1} that is explained in terms of partial amorphization of the nucleated NDs [7,8]. Moreover, a shoulder is observed on the ND peak, as highlighted in the inset of Fig. 6.2(c). This shoulder at ~ 1260 cm^{-1} , together with a diamond peak [9] with FWHM > 30 cm^{-1} , is often observed in detonation NDs [10]. This feature is a consequence of the confined vibrational domains inside NDs structure [11], and it is also observed when diamonds nanocrystals are separated by defects in larger diamond particles [9]. The presence of graphite layers around/embedding the NDs is evidenced by the graphite G peak in the Raman spectrum. Furthermore, also the G peak presents a shoulder at ~ 1620 cm^{-1} , which is the so-called D' band, arising from an intravalley double resonance process in defective graphene [12] and from other sp^2 -related defects [13]. Interestingly, this shoulder was already observed in detonation NDs clusters Raman spectrum [8]. To check the incorporation of nitrogen inside the NDs and the eventual NV center formation, the photoluminescence (PL) from NDs is studied and reported in Fig. 6.2(d). Under continuous-wave 532 nm laser irradiation, a broad red emission is detected, similar to what we observed in the previous chapter regarding fluorescent NDs laser synthesized in nitrogen atmosphere. This PL emission is consistent with the well-established [6,14] NV^- radiation, along with an additional tail in the low-wavelength region due to sp^2 surface defects on the NDs hosting the NV centers. Indeed, it is well known that the surface chemistry of the NDs plays an important role in

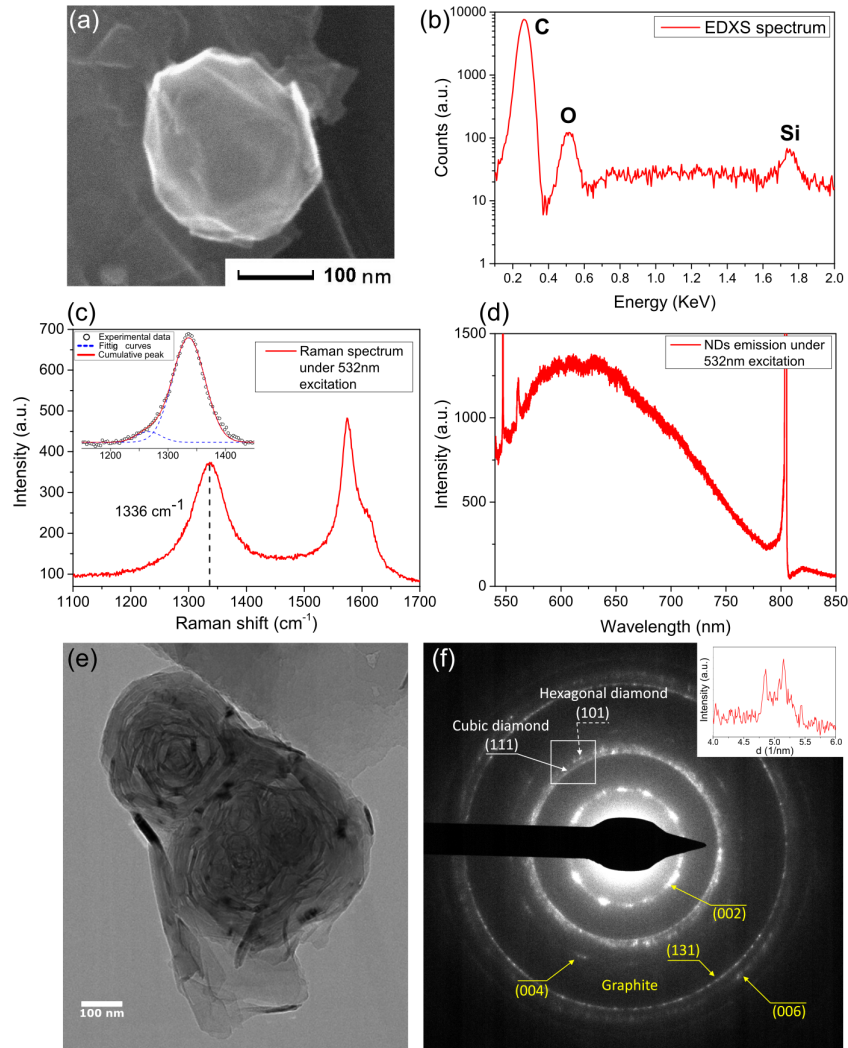


Fig. 6.2: Characterization of LN_2 -synthesized NDs. (a) SEM image of a typical nanoparticle, having dimension in the hundreds nm range. (b) Relative EDXS spectrum, showing the carbon peak at 0.27 keV, the oxygen one at 0.53 keV and silicon signal at 1.74 keV. (c) Raman spectrum under 532 nm laser excitation. Two peaks are detected, one at 1336 cm^{-1} , attributed to compressively-strained NDs, and the graphite G peak at $\sim 1580 \text{ cm}^{-1}$. The shoulder at $\sim 1620 \text{ cm}^{-1}$ is the D' peak. The inset shows the detail of the diamond peak: the shoulder at $\sim 1260 \text{ cm}^{-1}$ originates from small crystal domain size. (d) PL emission spectrum with 532 nm laser excitation. A bell-shaped PL centered at $\sim 625 \text{ nm}$ is observed, with the sharp peaks at 547 nm (520 cm^{-1}) and 561 nm (970 cm^{-1}) being the first and second order Raman scattering signals of the silicon substrate. (e) Bright field TEM image of a two graphitic-embedded crystallites whose diffraction pattern is given in (f). The rings labeled with the yellow arrows are those originating from graphite planes. The inset shows the intensity profile of the region identified by the white square, highlighting the presence of a two rings (indexed by the white arrows) associated to NDs. The inner one at $4.85 \pm 0.06 \text{ nm}^{-1}$ ($2.06 \pm 0.03 \text{ \AA}$) and the outer at $5.14 \pm 0.06 \text{ nm}^{-1}$ ($1.95 \pm 0.02 \text{ \AA}$) are indexed as the cubic diamond (111) and the hexagonal diamond (101) plane reflections, respectively.

their fluorescence properties [15]. For instance, sp^2 defects on the NDs acts as a trap for photoexcited electrons [16], resulting into different radiative recombination [17] bringing to a loss of typical NV^- spectral features and consequent quenching of the NV^- luminescence [18]. Moreover, this observation of graphitic material on the synthesized NDs in the PL spectrum of “ sp^2 -contaminated” NV^- is consistent with the graphitic peak detection in the Raman spectrum (Fig. 6.2(c)). Transmission electron microscopy (TEM) gives further structural characterization. The obtained TEM image is reported in Fig. 6.2(e), which shows the formation of graphitic-embedded crystallites. On the NDs cluster imaged in Fig. 6.2(e) selected area electron diffraction (SAED) analysis is performed. Fig. 6.2(f) reports the pattern, confirming the presence of diamond nanocrystals inside the graphitic shell. Indeed, the two rings indicated by the two white arrows have radius of $4.85 \pm 0.06 \text{ nm}^{-1}$ and $5.14 \pm 0.06 \text{ nm}^{-1}$, that correspond to $2.06 \pm 0.03 \text{ \AA}$ and to $1.95 \pm 0.02 \text{ \AA}$ lattice spacing. These two lattice parameters are attributed respectively to the (111) lattice planes of cubic diamond and to the (101) planes of hexagonal diamond [19], the latter often referred as lonsdaleite [20]. The synthesis of a combination between cubic and hexagonal NDs was already observed during PLA of graphite in both water [21] and in oxygen atmosphere [22]. The other rings in the SAED pattern, labeled by the yellow arrows, are attributed to different planes of graphite. The external rings can be indexed as the (004), (131) and (006) planes of graphite, while the inner one having 3.36 \AA periodicity matches the (002) reflections of disordered graphitic layers stacking. Fig. 6.3(b) reports the spatially-resolved PL image. Where the powders are dispersed (see Fig. 6.3(a) for comparison with the bright field image of the same sample) many fluorescent spots are detected. To prove the NV^- origin of the detected PL, ODMR spectroscopy is performed over these luminescent spots. Under continuous 532 nm optical pumping, the emitted fluorescence is measured while irradiating the sample with the MW field spanning the frequency range 2.8 – 2.9 GHz. As shown in Fig. 6.1(b), a significant reduction in the detected fluorescence is observed when the MW frequency resonates with the zero-field splitting of the ground-state spin sublevels at 2.87 GHz [23], due to competitive non-radiative relaxation path opening for the photo-excited electrons [24]. This is observed in the typical ODMR spectra shown in Fig. 6.3(c)-(d), where the ODMR fingerprint of the NV^- center at 2.87 GHz is observed. In addition, a strain field acting on the NDs hosting the NV centers removes the degeneracy [5] of the ground-state spin sublevels (Fig. 6.1(b)), as observed in the ODMR spectrum reported in Fig. 6.3(d), where two MW resonances are detected [25].

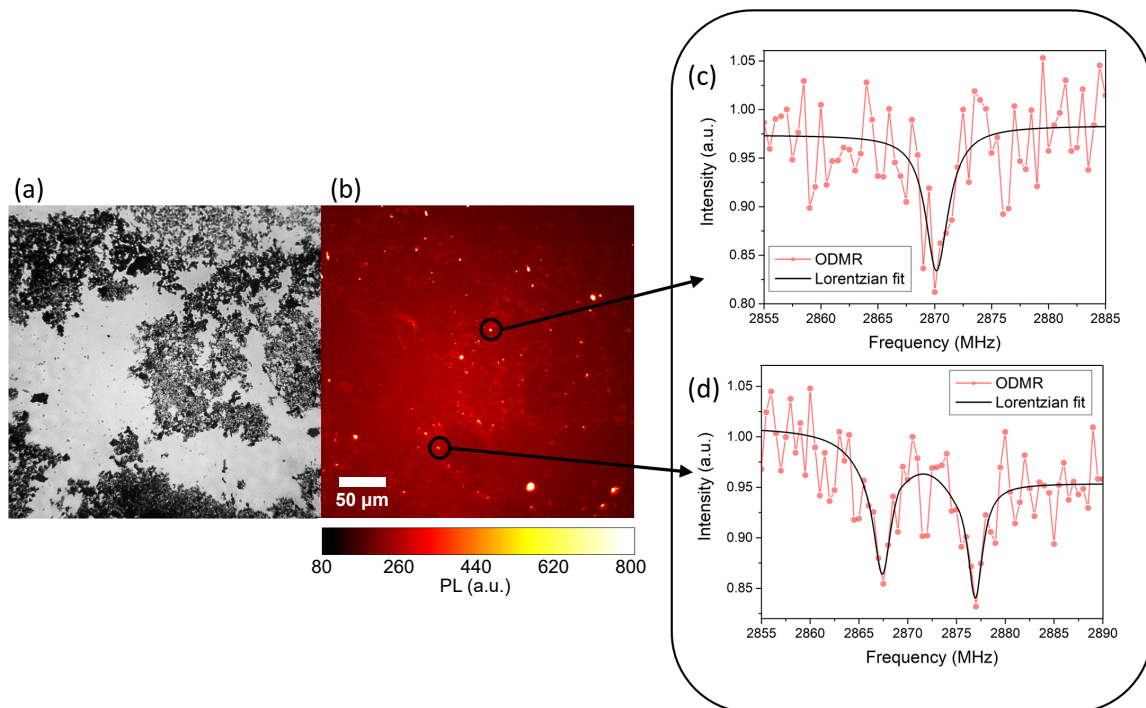


Fig. 6.3: (a) Wide field optical image and (b) relative PL image. (c)-(d) Typical ODMR spectra obtained from the bright spot of (b), confirming the NV origin of the collected PL. The intensity reduction at 2.87 GHz is evident in (c), while in (d) a double resonance is observed, due to strain of the NDs hosting the NV centers removing the degeneracy of the $m_s = \pm 1$ states.

As in the case of fluorescent NDs produced in a nitrogen atmosphere (Chapter 5), the strain is likely induced by the surface tension, which in turn is a consequence of NDs small crystal size [5]. The present ODMR measurements unequivocally prove the formation of NV^- centers inside the NDs obtained by pulsed laser ablation of graphite in liquid nitrogen [6]. Moreover, we are able to make a rough estimate of diamond production efficiency by comparing the wide field optical image (Fig. 6.3(a)) and the PL image (Fig. 6.3(b)). The total number of pixels where PL signal is detected in Fig. 6.3(b) is divided by the total area covered by graphitic powder in Fig. 6.3(a). This ratio, that is around 1 – 2%, can be used as diamond production efficiency, as it gives a rough estimate of diamond/graphite concentration in the sample. Nevertheless, as we are using PL emission to calculate NDs concentration, this is an underestimation of the diamond synthesis efficiency. Our estimation is based on the assumption that all the produced NDs contain NV centers, that is quite unlikely; moreover, some NDs might be completely covered by graphite preventing PL detection. Despite that, an

efficiency of 1 – 2% is comparable with the value of 5% reported by Yang et al. [26] for NDs production through ablation of graphite in water.

6.3.2 Thermodynamic model to explain NDs formation

In this section the model initially developed in Chapter 4 to describe NDs formation upon graphite laser ablation in water is extended to the case of PLA in LN₂, thus focusing the main difference between the two ablation conditions: room temperature water and liquid nitrogen. Firstly, the main aspects of the model are recalled. According to our model, the NDs formation occurs in strong undercooling condition of the liquid phase. Thus, to achieve graphite-diamond transformation the first step is the transition from graphite into carbon in liquid phase. Here, liquid carbon, in the form of nanodroplets, are produced during phase explosion induced in the graphite target by the nanosecond laser pulses [3]. Liquid nanodroplets formation, that is quantitatively described in the papers of Mazzi et al. [27, 28] (the main aspects are reported in Chapter 3 of this thesis), clearly contributes to explain the formation of NDs. To study the differences between ablation in water and in LN₂, it is important to know the pressure under which NDs formation may occur, as pressure is of the main parameters for liquid-carbon to diamond-phase transition. However, experimental measurement of the pressure P reached inside the plume, which represents the recoil pressure acting on the graphite target, is still missing. Thus, to estimate this value we use the Fabbro model [29] that allows to calculate the recoil pressure as function of the laser intensity I for different combination of target material and confining medium. This model is strictly derived from the first principle of thermodynamics, with the hypothesis of assuming laser intensity I to be constant during the pulsed duration τ and treating the plume as an ideal gas. The pressure P reached inside the plume is:

$$P = 0.01 \cdot \sqrt{\frac{\alpha}{2\alpha + 3}} ZI \quad (6.1)$$

The coefficient α (usually $\alpha \approx 0.25$) is the thermal energy fraction of total internal energy (the remaining $1 - \alpha$ fraction is the energy used for ionization of the gas), and Z is the reduced shock impedance between the shock impedance of graphite [30] $Z_g = 1.2 \cdot 10^6 \text{ g cm}^{-2} \text{ s}^{-1}$ and that of liquid nitrogen [31] $Z_{LN} = 0.77 \cdot 10^5 \text{ g cm}^{-2} \text{ s}^{-1}$. The parameter Z accounts for the mechanical properties of both the target and the

confining medium, and it is given by:

$$Z = 2 \frac{Z_g Z_{LN}}{Z_g + Z_{LN}} = 0.94 \cdot 10^6 \text{ g cm}^{-2} \text{ s}^{-1} \quad (6.2)$$

In our particular case, the laser intensity is $I = 1.9 \text{ GW cm}^{-2}$, corresponding to our 500mJ focused on a 1 mm^2 spot, with a 25% energy losses because of the focusing optics. Putting this value into Eq. 6.1, the calculated recoil pressure results $P \approx 3.5 \text{ GPa}$. As it can be observed in the carbon phase diagram of Fig. 6.4(a), for the range of temperature reached during graphite ablation ($\sim 5000 \text{ K}$ [32]), this pressure is enough to obtain liquid carbon. The whole graphite-liquid-diamond transition in the case of ablation in LN_2 is represented by the purple arrow in the carbon phase diagram [4] in Fig. 6.4(a). The tilted red lines indicate the region, referred also as “diamond-like” liquid [33], where undercooled liquid carbon and metastable diamond coexist. Transition to diamond phase occurs because in this thermodynamic condition the energy barrier for diamond formation is lower than that for graphite formation [34]. Undercooling of liquid carbon is a fundamental step for NDs formation, so another possible difference between NDs synthesized in water and in LN_2 may arise from the difference cooling rate - different degree of undercooling - achieved in the ablation plume. To investigate the cooling processes, we have to compare the physical parameters of the two media. Water shows both a higher heat capacity C_v ($C_v = 74.53 \text{ J mol}^{-1} \text{ K}^{-1}$) and higher thermal conductivity Λ ($\Lambda = 0.591 \text{ W m}^{-1} \text{ K}^{-1}$ at 293 K), respect to LN_2 having heat capacity $C_v = 56.83 \text{ J mol}^{-1} \text{ K}^{-1}$ at 77 K [36] and thermal conductivity $\Lambda = 0.138 \text{ W m}^{-1} \text{ K}^{-1}$ at 77 K [35], leading to a higher efficiency in heat dissipation. However, water advantage in heat dissipation may be balanced by the much lower temperature (77 K) of liquid nitrogen as compared to room-temperature water. Quantitatively, by solving analytically the heat flow equation a reasonable estimation of the cooling rate can be obtained. A cooling rate in the order of $\sim 10^{11} \text{ K s}^{-1}$ is attained for both water and LN_2 , with liquid carbon heat capacity of $26 \text{ J mol}^{-1} \text{ K}^{-1}$ and a density of 1.6 g cm^{-3} [37]. This estimation is consistent with the usual cooling rates values reported for ablation in liquid media [38]. As a consequence, a relevant dissimilarity in the morphology of the synthesized NDs in LN_2 and water is not observed [3, 4] despite the differences in the physical properties of the two liquid media. Finally, single nitrogen atoms, required for NV centers formation, can be easily obtained inside the LN_2 because of the high laser fluence used. Indeed, the high power deposited to the graphite target

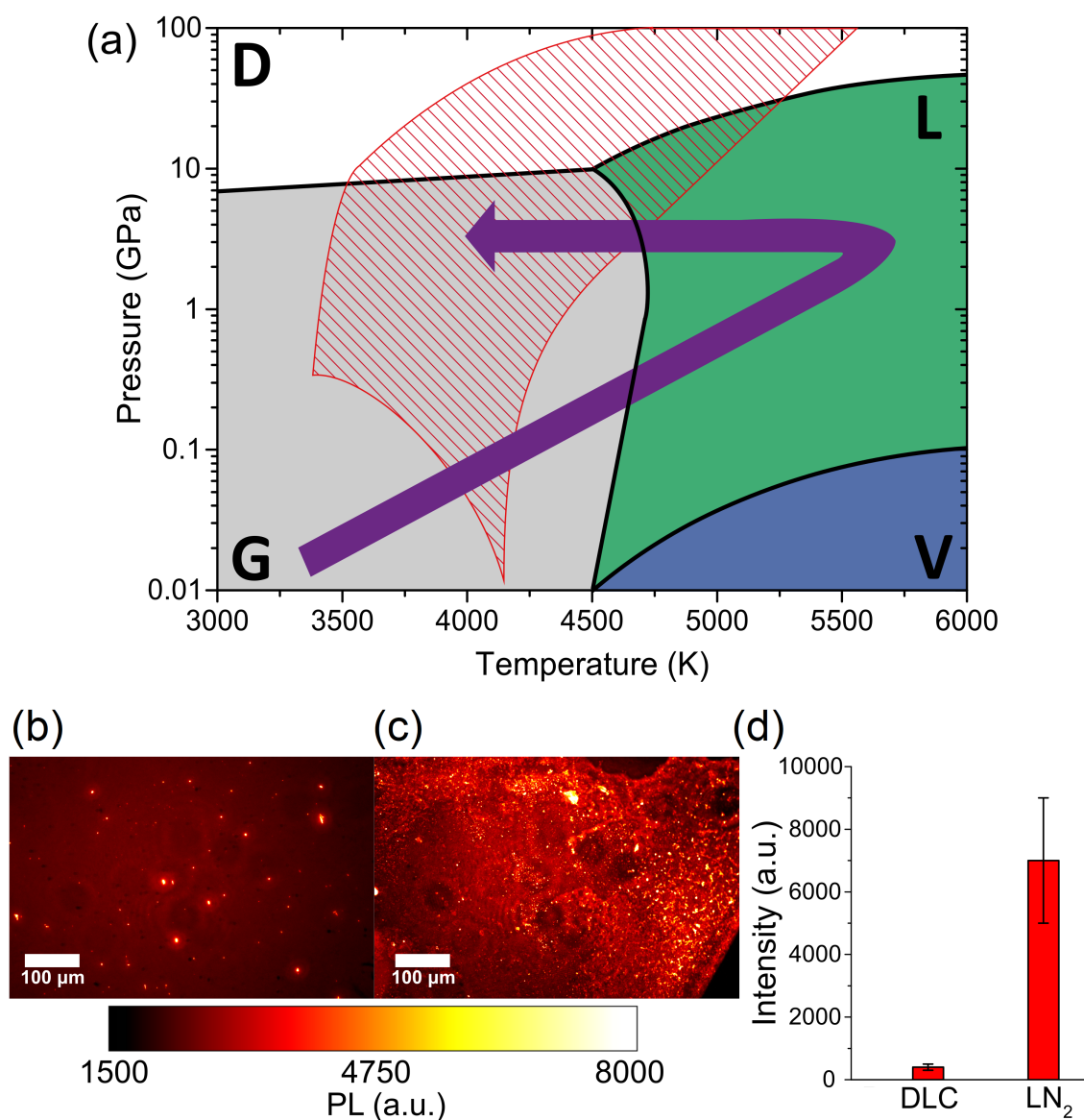


Fig. 6.4: (a) Carbon phase diagram. Stability regions of diamond (D), graphite (G), vapor (V) and liquid carbon (L) are indicated, respectively, in white, grey, blue, and green. The purple arrow shows the graphite-liquid-diamond transition used to explain NDs formation after pulsed laser irradiation of graphite in LN₂. The tilted red lines give the region known as "diamond-like liquid" [33], where undercooled liquid carbon and metastable diamond coexist. Typical PL wide field images of NDs synthesized by PLD in nitrogen atmosphere (b) and by PLA in liquid nitrogen (c). (d) PL strength comparison between the two samples, obtained by integrating the intensity of the whole PL-image after background subtraction: LN₂-NDs show a more than 10x higher emission compared to DLC-embedded NDs. The error bars of (d) are given by the standard deviation of the different integrated images.

is sufficient for emission of highly energetic species, such as carbon ions and electrons, with kinetic energy as high as 100 eV [39]. This energy is then enough to break the nitrogen molecules into single nitrogen atoms.

6.4 Comparison with nitrogen atmosphere PLD-synthesized fluorescent NDs

The results described in this section are here compared to what is reported in Chapter 5 of this thesis. The aim is to compare the results of NDs synthesis upon graphite laser ablation in liquid nitrogen and nitrogen atmosphere, to better underline the relevance of the present results towards the establishment of an experimental procedure able to prepare NDs with controlled amount of NV^- centers. Moreover, the main points of the thermodynamic model for NDs formation description will be used to explain the differences in the experimental results. For comparison, two samples are prepared, one through ablation of graphite in liquid nitrogen (referred as “LN₂”), the other in 1 Pa nitrogen atmosphere (referred as “DLC”, as in this case the NDs are embedded in a DLC film; see Chapter 5 for details). The two samples are prepared under nominally identical laser deposition conditions: laser energy of ~ 500 mJ per pulse, laser spot of ~ 1 mm² on the graphite surface for a total of 3000 laser pulses. To study the different NDs synthesis efficiency of the two methods, PL imaging is used for a quantitative optical comparison: typical PL images for DLC and LN₂ samples are given in Fig. 6.4(b) and (c). After a suitable background subtraction, the total intensity of the PL image is integrated and averaged over 5 images per sample. The standard deviation from the mean value is used as the error bar of the total PL. The result, shown in Fig. 6.4(d), proves that the LN₂-NDs have a PL emission intensity (7000 ± 2000 a.u.) that is more than one order of magnitude higher respect to DLC-Nds (400 ± 100 a.u.). The easiest explanation may rely on the larger nitrogen doping that is likely reached during ablation in LN₂, in turn leading to a larger number of NV^- centers, due to the much higher nitrogen concentration in the liquid medium (0.807 g/ml) with respect to the diluted gas at 1 Pa. However, this statement is not correct, as larger amount of nitrogen during deposition may not result in a higher NV density. This is observed for the DLC samples, where the total PL emission intensity is not monotonically increasing as function of nitrogen pressure (see Chapter 5). Therefore, the reason for the higher fluorescent NDs synthesis efficiency for ablation in LN₂ has to be searched in the different carbon

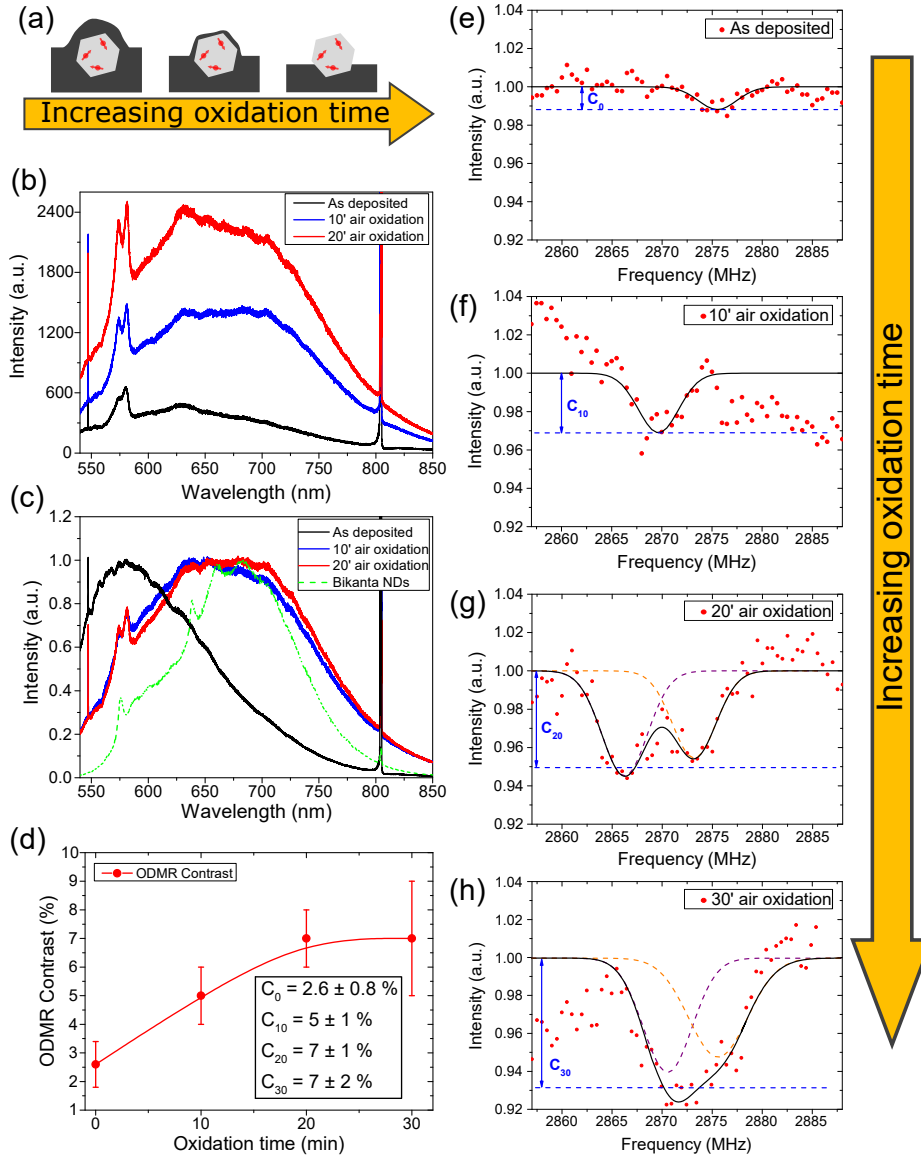


Fig. 6.5: NDs cleaning. (a) Schematics of the air-oxidation process: by removal of the graphitic shell through oxidation in air at 400°C of the sp^2 carbon atoms, the fully covered NDs are exposed. (b) Evolution of PL spectra with increasing oxidation time, represented by the yellow arrow. An increase of the PL intensity after 10 min air-oxidation (blue curve) and 20 min (red curve) with respect to the as deposited sample (black curve) is observed. (c) To highlight the shift of the PL bell after thermal treatment, the PL spectra are normalized. The green dashed curve is the PL spectrum of commercial 40 nm-uncoated NDs. (d) ODMR contrast C as function of the oxidation time. The inset gives the averaged C values for each oxidation step. Pictures (e) (f) (g) (h) give, respectively, typical ODMR for the as deposited sample and the 10', 20' and 30' oxidized ones. The red dots are the experimental values, while the black lines are the Gaussian fits. The relative RF shifts in the ODMR dips between (e), (f), (g) and (h) panels are attributed to strain effects [5] acting with a substantial component along the NV-center axis.

plume expansion dynamics within the confining medium. In particular, according to our model for NDs synthesis, two parameters play a central role for diamond phase formation: the pressure and the cooling rate reached in the ablation plume. Thus, the differences between the two samples have to be searched in the different conditions attained in the two media. The peculiar physical processes occurring during plume expansion in a dense environment, such as a liquid, are fully described in Chapter 3. For instance, it is well known that inside a liquid, the plume expansion is confined, resulting in a limited plume size [40] compared to ablation in a rarefied gas. Moreover, the pressure peak induced by the shock wave emitted during ablation in liquid (process fully described in Chapter 3) should be considered, in particular its time duration being \sim twice the laser pulse length. These two considerations suggest that the high-pressure condition - required for diamond phase formation - is enhanced during ablation in LN₂. Furthermore, due to the very efficient collisional cooling, the lifetime of a plasma plume expanding in liquid is much shorter - meaning that the cooling rate is higher. For instance, plasma lifetime for graphite ablation in air is one order of magnitude larger respect to ablation in water [42]. We are comparing the liquid phase with a rarefied 1 Pa nitrogen gas, so in our case the difference is even broader. The lifetime of the plume has a direct consequence on the phase in which the material contained in it condenses. In details, a higher lifetime brings to a larger time interval in which the ablated species are chemically active, also when the pressure conditions are not those required for diamond formation. The result is the formation of a sp² shell embedding the synthesized NDs when ablation is performed in N₂ atmosphere. Summarizing, larger NV-enriched NDs production efficiency, observed through the higher PL intensity in Fig. 6.4(b)-(d), can be related to the different condition attained inside ablation plume. In particular, a strong sp² contamination of the NV-enriched NDs surface is observed when laser ablation in a gaseous environment, due to both lower pressure and smaller cooling rates achieved in the ablation plume. A specific experiment is performed to assess this statement. In particular, to study the effect of the graphitic surface shell on the PL emission, NDs are cleaned from those sp² defects. The cleaning procedure consists in thermal oxidation in air at 400°C (Fig. 6.5(a)). At this temperature, oxygen in the air selectively etches sp²-carbon atoms with no loss of diamond. This particular cleaning method is demonstrated to be very effective for the cleaning of NDs surface [43]. The status of NDs purification is assessed by studying the PL intensity and through ODMR measurements. The effected of graphite removal in the PL spectra can be

seen in Fig. 6.5(b)-(c) for 10' and 20' air oxidation. Firstly, an increase in the PL intensity is measured (Fig. 6.5(a)) with increasing oxidation time. The observation of the quenching effect of the sp^2 related optically-active defects in the NV^- emission is thus confirmed. In particular, after 10' of air oxidation (Fig. 6.5(b) blue curve) the PL signal is more than 3x larger with respect to the as deposited sample (Fig. 6.5(b) black curve). When the air oxidation time is increased to 20' (Fig. 6.5(b) red curve), PL intensity increases by a factor 5. Remarkably, with this experiment the sp^2 origin of the spectral tail in the < 600 nm region of laser-synthesized NDs' PL curve is also confirmed. Indeed, when the spectra are normalized (Fig. 6.5(c)), is it evident a ~ 100 nm redshift of the PL spectrum. ODMR measurements provide an additional confirmation of NDs purification through thermal oxidation. The sp^2 -related fluorescence is just a constant background in the ODMR spectra, as these defects do not present a microwave-dependent energetic level configuration (at least in this RF region). Thus, a decrease of this background should be obtained with partial removal of the graphitic shell on NDs surface, allowing a better detection of NV^- emitted photons. This is actually observed in Fig. 6.5(d), which shows the ODMR contrast C as function of the oxidation time. The ODMR contrast C , defined as $C = 1 - I_{ON}/I_{OFF}$, where I_{ON} and I_{OFF} are the intensities ON-resonance and OFF-resonance, increases with the oxidation time, till reaching a saturation after 30' oxidation. The saturation of the contrast is expected because this parameter is an intrinsic property of the very NV center [23]. For each oxidation step, C is averaged over 5 fluorescent centers: Fig. 6.5(d) inset gives the average C for each step, where the error bars are the standard deviations from the average value. For the sample air-oxidized 0' (as deposited), 10', 20' and 30', typical ODMR spectra are respectively given in Fig. 6.5(e)-(f)-(g)-(h). The measured contrast ranges from $C_0 = (2.6 \pm 0.8)\%$ for the as deposited sample to $C_{30} = (7 \pm 2)\%$ for the 30' oxidized sample. It is worth noticing that the final maximum contrast of $C_{30} = (7 \pm 2)\%$ is compatible with recent ODMR analysis of HPHT fluorescent NDs [44]. Moreover, the contrast reached for the purified DLC-NDs is consistent with the contrast of the LN_2 -synthesized NDs. Summarizing, to reach the same quality - measured in term of ODRM contrast - of PL emission the DLC-NDs a purification step is required. This observation allows us to conclude that ablation of graphite in LN_2 is an efficient way to synthesize fluorescent NDs compared to other laser-assisted technique.

6.5 Conclusions

In this chapter, pulsed laser ablation of graphite immersed in liquid nitrogen is employed for the synthesis of NV-enriched ND. This method represents an efficient and novel fluorescent NDs synthesis procedure, where the undercooling thermodynamic channel acts as a booster on the density of light-emitting NDs. Selected area electron diffraction demonstrate diamond phase formation whereas optically detected magnetic resonance unequivocally proves NV⁻ origin of the detected luminescence emission. A refinement of the thermodynamic model developed in Chapter 4 of this thesis is also provided, stressing the benefits arising from the confining liquid nitrogen. Moreover, to highlight the good quality of the LN₂-synthesized fluorescent NDs, a comparison with the NV-embedding NDs previously obtained through PLA in nitrogen atmosphere (Chapter 5) is reported. In particular, ODMR spectroscopy is used as a diagnostic tool to monitor NDs surface quality. In addition, the higher PL emission of the LN₂-NDs is explained in term of the theoretical model describing diamond phase formation, namely by considering the different thermodynamic conditions achieved in the two different cases. This comparison analysis stresses the unnecessary post-synthesis PL activation or NDs cleaning. Concluding, the reported results may open the way to an efficient and controlled production of laser-synthesized (read: cheap and industrially compatible) NDs powders for application in biological quantum sensing and imaging.

References for chapter 6

- [1] A. Bhaumik, R. Sachan, J. Narayan, Tunable charge states of nitrogen-vacancy centers in diamond for ultrafast quantum devices, *Carbon* 142 (2019) 662-672.
- [2] S. Kumar, M. Nehra, D. Kedia, N. Dilbaghi, K. Tankeshwar, K.H. Kim, Nanodiamonds: Emerging face of future nanotechnology, *Carbon*. 143 (2018) 678-699
- [3] L. Basso, F. Gorrini, N. Bazzanella, M. Cazzanelli, C. Dorigoni, A. Bifone, et al., The modeling and synthesis of nanodiamonds by laser ablation of graphite and diamond-like carbon in liquid-confined ambient, *Appl. Phys. A* 124 (2018) 72.
- [4] F. Gorrini, M. Cazzanelli, N. Bazzanella, R. Edla, M. Gemmi, V. Cappello, et al., A. On the thermodynamic path enabling a room-temperature, laser-assisted graphite to nanodiamond transformation, *Sci. Rep.* 6 (2018) 35244.
- [5] L. Basso, F. Gorrini, M. Cazzanelli, N. Bazzanella, A. Bifone, A. Miotello, An all-optical single-step process for production of nanometric-sized fluorescent diamonds, *Nanoscale* 10 (2018) 5738–5744.

BIBLIOGRAPHY

- [6] C. Bradac, T. Gaebel, N. Naidoo, M.J. Sellars, J. Twamley, L.J. Brown, et al., Observation and control of blinking nitrogen-vacancy centres in discrete nanodiamonds, *Nat. Nanotechnol.* 5 (2010) 345-349.
- [7] A.C. Ferrari, J. Robertson, Raman spectroscopy of amorphous, nanostructured, diamond-like carbon, and nanodiamond, *Phil. Trans. R. Soc. Lond. A* 362 (2004) 2477-2512.
- [8] S. Praver, K.W. Nugent, D.N. Jamieson, J.O. Orwa, L.A. Bursill, J.L. Peng, The Raman spectrum of nanocrystalline diamond, *Chem. Phys. Lett.* 332 (2000) 93-97.
- [9] V.N. Mochalin, O. Shenderova, D. Ho, Y. Gogotsi, The properties and applications of nanodiamonds, *Nat. Nanotechnol.* 7 (2012) 11-23.
- [10] G.N. Yushin, S. Osswald, V.I. Padalko, G.P. Bogatyreva, Y. Gogotsi, Effect of sintering on structure of nanodiamond, *Diam. Relat. Mater.* 14 (2005) 1721-1729.
- [11] S. Osswald, V.N. Mochalin, M. Havel, G. Yushin, Y. Gogotsi, Phonon confinement effects in the Raman spectrum of nanodiamond, *Phys. Rev. B* 80 (2009) 075419.
- [12] A.C. Ferrari, D.M. Basko, Raman spectroscopy as a versatile tool for studying the properties of graphene, *Nature Nanotech.* 8 (2013) 235
- [13] S. Stehlik, M. Varga, M. Ledinsky, D. Miliaieva, H. Kozak, V. Skakalova, et al., High-yield fabrication and properties of 1.4 nm nanodiamonds with narrow size distribution, *Sci. Rep.* 6 (2016) 38419.
- [14] P.H. Chung, E. Perevedentseva, C.L. Cheng, The particle size-dependent photoluminescence of nanodiamonds, *Surf. Sci.* 601 (2007) 3866-3870.
- [15] P. Reineck, D.W. Lau, E.R. Wilson, K. Fox, M.R. Field, C. Deelepojananan, et al., Effect of surface chemistry on the fluorescence of detonation nanodiamonds, *ACS Nano* 11 (2017) 10924-10934.
- [16] A. Stacey, N. Dontschuk, J.P. Chou, D.A. Broadway, A.K. Schenk, M.J. Sear, et al., Evidence for primal sp^2 defects at the diamond surface: candidates for electron trapping and noise sources, *Adv. Mater. Interfaces* 6 (2018) 1801449.
- [17] A.R. Kirmani, W. Peng, R. Mahfouz, A. Amassian, Y. Losovyj, H. Idriss, et al., On the relation between chemical composition and optical properties of detonation nanodiamonds, *Carbon* 94 (2015) 79-84.
- [18] B.R. Smith, D. Gruber, T. Plakhotnik, The effects of surface oxidation on luminescence of nano diamonds, *Diam. Relat. Mater.* 19 (2010) 314-318.
- [19] A. Kumar, P.A. Lin, A. Xue, B. Hao, Y.K. Yap, R.M. Sankaran, Formation of nanodiamonds at near-ambient conditions via microplasma dissociation of ethanol vapour, *Nat. Commun.* 4 (2013) 2618.
- [20] P.S. DeCarli, J.C. Jamieson, Formation of diamond by explosive shock, *Science* 133 (1961) 1821-1822.

- [21] G.W. Yang, J.B. Wang, Q.X. Liu, Preparation of nano-crystalline diamonds using pulsed laser induced reactive quenching, *J. Phys. Condens. Mat.* 10 (1998) 7923-7927.
- [22] Z.Y. Chen, J.P. Zhao, T. Yano, J. Sakakibara, Growth mechanism of diamond by laser ablation of graphite in oxygen atmosphere, *Phys. Rev. B* 62 (2000) 7581-7586.
- [23] L. Rondin, J.P. Tetienne, T. Hingant, J.F. Roch, P. Maletinsky, V. Jacques, Magnetometry with nitrogen-vacancy defects in diamond, *Rep. Prog. Phys.* 77 (2014) 056503.
- [24] M.W. Doherty, N.B. Manson, P. Delaney, F. Jelezko, J. Wrachtrup, L.C. Hollenberg, The nitrogen-vacancy colour centre in diamond, *Phys. Rep.* 528 (2013) 1-45.
- [25] A.O. Levchenko, V.V. Vasil'ev, S.A. Zibrov, A.S. Zibrov, A.V. Sivak, I.V. Fedotov, Inhomogeneous broadening of optically detected magnetic resonance of the ensembles of nitrogen-vacancy centers in diamond by interstitial carbon atoms, *Appl. Phys. Lett.* 106 (2015) 102402.
- [26] L. Yang, P.W. May, L. Yin, J.A. Smith, K.N. Rosser, Growth of diamond nanocrystals by pulsed laser ablation of graphite in liquid, *Diam. Relat. Mater.* 16 (2007) 725-729.
- [27] A. Mazzi, F. Gorrini, A. Miotello, Liquid nanodroplet formation through phase explosion mechanism in laser-irradiated metal targets, *Phys. Rev. E* 92 (2015) 031301.
- [28] A. Mazzi, A. Miotello, Simulation of phase explosion in the nanosecond laser ablation of aluminum, *J. Colloid Interface Sci.* 489 (2017) 126-130.
- [29] R. Fabbro, J. Fournier, P. Ballard, D. Devaux, J. Virmont, Physical study of laser-produced plasma in confined geometry, *J. Appl. Phys.* 68 (1990) 775-784.
- [30] M.F. Gogulya, Shock structure and parameters under dynamic loading of natural graphite in the polymorphic transformation domain, *Comb. Expl. Shock Waves* 25 (1989) 87-95.
- [31] W.J. Nellis, A.C. Mitchell, Shock compression of liquid argon, nitrogen, and oxygen to 90 GPa (900 kbar), *J. Chem. Phys.* 73 (1980) 6137-6145.
- [32] T. Sakka, K. Saito, Y.H. Ogata, Emission spectra of the species ablated from a solid target submerged in liquid: vibrational temperature of C₂ molecules in water-confined geometry, *Appl. Surf. Sci.* 197 (2002) 246-250.
- [33] L.M. Ghiringhelli, J.H. Los, E.J. Meijer, A. Fasolino, D. Frenkel, Modeling the phase diagram of carbon, *Phys. Rev. Lett.* 94 (2005) 145701.
- [34] A.Y. Basharin, V.S. Dozhdikov, A.V. Kirillin, M.A. Turchaninov, L.R. Fokin, Phase diagram with a region of liquid carbon-diamond metastable states, *Tech. Phys. Lett.* 36 (2010) 559-562.
- [35] R.A. Perkins, H.M. Roder, D.G. Friend, C.N. De Castro, The thermal conductivity and heat capacity of fluid nitrogen, *Physica A* 173 (1991) 332-362.

BIBLIOGRAPHY

- [36] J.W. Magee, Molar heat capacity (CV) for saturated and compressed liquid and vapor nitrogen from 65 to 300 K at pressures to 35 MPa, *J. Res. NIST* 96 (1991) 725-740.
- [37] J. Steinbeck, G. Dresselhaus, M.S. Dresselhaus, The properties of liquid carbon, *Int. J. Thermophys.* 11 (1990) 789-796.
- [38] Z. Yan, D.B. Chrisey, Pulsed laser ablation in liquid for micro-/nanosstructure generation, *J. Photoch. Photobiol. C* 13 (2012) 204-223.
- [39] A.A. Ionin, S.I. Kudryashov, L.V. Seleznev, Near-critical phase explosion promoting breakdown plasma ignition during laser ablation of graphite, *Phys. Rev. E* 82 (2010) 016404.
- [40] C.Y. Shih, M.V. Shugaev, C. Wu, L.V. Zhigilei, Generation of subsurface voids, incubation effect, and formation of nanoparticles in short pulse laser interactions with bulk metal targets in liquid: Molecular dynamics study, *J. Phys. Chem. C* 121 (2017) 16549-16567.
- [41] C.Y. Shih, C. Wu, M.V. Shugaev, L.V. Zhigilei, Atomistic modeling of nanoparticle generation in short pulse laser ablation of thin metal films in water, *J. Colloid Interface Sci.* 489 (2017) 3-17.
- [42] K. Saito, K. Takatani, T. Sakka, Y.H. Ogata, Observation of the light emitting region produced by pulsed laser irradiation to a solid-liquid interface, *Appl. Surf. Sci.* 197 (2002) 56-60.
- [43] S. Osswald, G. Yushin, V. Mochalin, S.O. Kucheyev, Y. Gogotsi, Control of sp^2/sp^3 carbon ratio and surface chemistry of nanodiamond powders by selective oxidation in air, *J. Am. Chem. Soc.* 128 (2006) 11635-11642.
- [44] M.H. Alkahtani, F. Alghannam, L. Jiang, A.A. Rampersaud, R. Brick, C.L. Gomes, Fluorescent nanodiamonds for luminescent thermometry in the biological transparency window, *Opt. Lett.* 43 (2018) 3317-3320.

Chapter 7

Fluorescent NDs from N-doped graphite target and comparison between different laser-synthesis techniques

Throughout this thesis NV centers were obtained by pulsed laser ablation of graphite in nitrogen-containing medium, thus using the environment as a source of nitrogen for the creation of the color center. Here, the opposite process is exploited, as the source of nitrogen is the target itself. Indeed, synthesis of NV-fluorescent NDs is obtained through pulsed laser ablation of a N-doped graphite target in water. The obtained NDs are fully characterized in the morphological and optical properties, in particular with optically detected magnetic resonance spectroscopy to unequivocally prove the NV origin of the NDs photoluminescence. Moreover, this particular target is used to compare the different laser-ablation-based NDs synthesis techniques developed and described in the other chapters of this thesis. In particular, an analysis of the effect of the medium in which laser ablation is performed is reported. Along with it, the thermodynamic model used to describe NDs formation is employed to explain the different results in terms of the physical processes occurring during laser irradiation. Finally, we show that the use of this particular target can lead to a precise control in the photoluminescence intensity level in the produced NDs.

7.1 Introduction

Of great importance for sensing application is the production of NDs with highly dense NV ensemble to increase detection efficiency. As a matter of fact, sensitivity scales as \sqrt{N} , with N being the number of NV centers [1]. A multi-step post-synthesis treatment of the NDs, consisting in ion/electrons irradiation followed by annealing at high temperatures [2], is the standard way to obtain highly NV dense NDs. As widely demonstrated in this thesis, an alternative is represented by laser ablation, that successfully convert graphite into NDs with a limited size distribution (< 100 nm) [4,5]. In this chapter, fluorescent NDs are produced through ablation in water of a N-doped graphite target. The details of target preparation, the setup used for laser ablation and the techniques used for characterization (especially regarding the estimation of nitrogen concentration in the target) are all given in section 7.2. The produced sample is fully characterized in its structural and optical properties: the analysis are reported in section 7.3. NDs produced through this particular N-doped graphite target show a strong photoluminescence (PL) emission and a typical NV^- center optically detected magnetic resonance (ODMR) fingerprint. With the aim of finding the most efficient synthesis condition in terms of PL intensity, this particular target is used to compare the different fluorescent NDs production techniques developed in this thesis, namely in gaseous nitrogen (Chapter 5) and in liquid nitrogen (Chapter 6). The different results are reported in section 7.3.2, showing that ablation in liquid nitrogen brings the best NV-centers enriched NDs production efficiency. Furthermore, this experimental observation is theoretically explained by considering the chemical/physical properties of the confining medium, and the consequent processes occurring during laser ablation. This result is relevant for future NDs applications in quantum sensing, as it shows the laser-synthesis yielding the most NV-dense NDs. Finally, in section 7.3.3, the effect of nitrogen concentration in the N-doped graphite target is studied. This is done by preparing two targets with different N-doping level, that are then laser-ablated in the same confining medium. Remarkably, we showed that this particular target could open a way to obtain NDs with a tunable concentration of NV centers, by adjusting the nitrogen concentration in the starting graphite.

7.2 Experimental methods

7.2.1 N-doped target preparation

To obtain the N-doped graphite target, the starting raw material was graphite powder (median size 7-10 μm) purchased from Alfa Aesar. Chemicals, that were used without further purification, were purchased in reagent grade from Sigma Aldrich and Alfa Aesar. The N-doped graphite powder was obtained performing a 1,3-dipolar cycloaddition via amino acid in situ-generated azomehtine ylide (glycine or hystidine) on the sp^2 carbon graphite surface. The nitrogen atom required for graphite doping is brought by the cycloaddition adduct (a pyrrolidine ring). More in details: 1.102 g of graphite were suspended in a solution made by 0.550 g of paraformaldehyde (18.3 mmol, 1 eq) and 1.650 g of glycine (22.0 mmol, 1.2 eq.) in 20 mL of DMF. The suspension was allowed to react for 2h at 130°C under magnetic stirring. After cooling to room temperature the reaction mixture was centrifuged (4000 rpm, 8 min) and the supernatant was discarded. The graphite was subjected to several centrifugation cycles (water, 4000 rpm, 8 min, 3x; water/dioxane 1:1, 4000 rpm, 8 min, 3x; dioxane, 4000 rpm, 8 min, 3x). Drying at 70°C for 24 h yielded the functionalized graphite, ready for thermogravimetric analysis. By changing the composition of the initial solution: another sample with a lower concentration of nitrogen was prepared: 1.010 g of graphite were suspended in a solution of 2.52 g of p-nitrobenzaldehyde (16.7 mmol, 1 eq) and 3.080 g of hystidine (20.0 mmol, 1.2 eq.) in 45 mL of DMF. Finally, 200 mg of the N-doped graphite powder were pressed to 50 bar to form a 1 mm thick target of 1 cm diameter.

7.2.2 Pulsed laser ablation

Pulsed laser ablation of the N-doped graphite target is performed, by using the same KrF excimer laser described in Chapter 4, in different confining media: water, nitrogen atmosphere and liquid nitrogen. The different experimental setups for the three cases are the ones described in, respectively, Chapter 4, Chapter 5 and Chapter 6. In order to compare samples synthesized in the same nominal conditions, laser ablation is performed with the laser operated in the same configuration: pulse energy of ~ 500 mJ, spot size of ~ 1 mm² and a total of 3000 laser pulses. Regarding the ablation in liquid media, the ablated powder was dispersed in 250 μL of isopropanol and then 2 μL were deposited on a substrate for characterization.

7.2.3 Characterization techniques

To measure nitrogen concentration in the target thermogravimetric analysis (TGA) was performed, as this technique can provide information about the thermal stability of surface groups. Thermogravimetric measurements were carried out on a TGA 4000 analyzer (Perkin Elmer) under high purity argon atmosphere, in the temperature range $50^{\circ}\text{C} - 800^{\circ}\text{C}$, with a heating rate of $10^{\circ}\text{C min}^{-1}$ (ca.10 mg of sample were used for each analysis). The derivatization amount has been calculated from weight loss percentage differences, with respect to the untreated graphite, at 650°C , and expressed in terms of mol/g. From the measured value of molar amount of pyrrolidine adduct, the final nitrogen doping amount was calculated and expressed in terms of grams of nitrogen per gram of graphite. The other characterization methods are already described in Chapter 4 and 5.

7.3 Results and discussion

7.3.1 NDs synthesis and characterization

Before being pressed to form the target for laser ablation, the N-doped graphite powder was studied with TGA to quantify nitrogen concentration achieved during derivatization. Successful derivatization is proved as a weight loss is observed at $\sim 230^{\circ}\text{C}$ compared to untreated graphite (Fig. 7.1(a)). The weight loss is a consequence of the removal of the pyrrolidine ring containing the nitrogen from graphite. To quantify this nitrogen amount, the percentage weight loss was calculated at 650°C . From this value, and knowing the molar weight of the adduct used, a nitrogen concentration of 23.2 mg/g of graphite is calculated. At this point, N-doped graphite powder was pressed to form a pellet, that was then used as a target for laser-ablation in water. Fig. 7.1(b) reports the SEM morphological analysis of the ablated material, showing nanoparticles having size of $\sim 100 \text{ nm}$. The presence of NDs in the ablated material was proven by Raman spectroscopy. The spectrum, given in Fig. 7.1(c), is still dominated by the graphite G peak at $\sim 1580 \text{ cm}^{-1}$ (see inset), but the peak at $\sim 1340 \text{ cm}^{-1}$ is a convolution between the graphite D peak [8] and, most importantly, the diamond peak at 1335 cm^{-1} . Raman NDs peak width ($\text{FWHM} \simeq 44 \text{ cm}^{-1}$), due to partial amorphization, and its shift respect to the 1332 cm^{-1} bulk diamond peak, related to compressive mechanical strain, are usually observed for NDs [7,9]. The presence of the graphitic

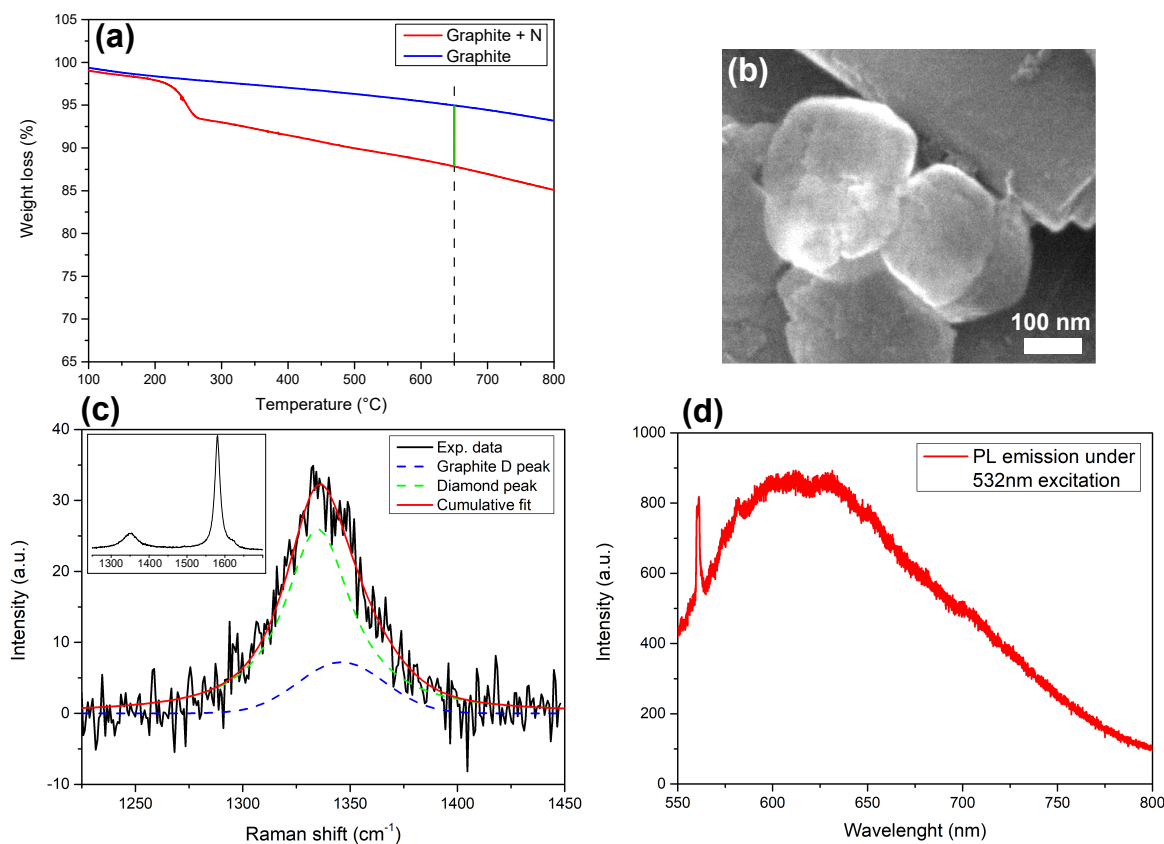


Fig. 7.1: Sample characterization. (a) TGA analysis of the N-doped graphite powder. To extract nitrogen content, the weight loss of the derivatized sample (red line) respect to the untreated graphite (blue line) is measured at the temperature of 650°C (green line). (b) Typical SEM image of the nanoparticles resulting from laser ablation in water: ~ 100 nm sizes NDs are observed. (c) Raman spectrum of the ablated powder (532 nm laser excitation). The inset shows the whole Raman spectrum, that is dominated by the so-called graphite G peak at $\sim 1580\text{ cm}^{-1}$. The detail of the peak at $\sim 1340\text{ cm}^{-1}$ is shown in this panel. The experimental data are properly fitted by two Gaussian function, one at 1335 cm^{-1} (green dashed line), attributed to compressively-strained NDs, and one at 1346 cm^{-1} , that is the graphite D peak (blue dashed line). (d) PL spectrum of the NDs obtained with a 532 nm laser pumping. The already-reported broad emission consistent with NV^{-} -fluorescence with the sp^2 -related tail is observed. The sharp peak at 561 nm (corresponding to 970 cm^{-1}) is the second order Raman peak of the silicon substrate where the powder is dispersed.

peaks means that the synthesized NDs are embedded in a graphitic shell. Moreover, both SEM analysis and Raman characterization are consistent with NDs obtained through ablation of pyrolytic graphite in different liquid environment, as reported in the previous chapter of this thesis. The PL spectrum is reported in Fig. 7.1(d), where under continuous 532 nm laser excitation a broad band emission is observed. It is consistent

with the already observed NV^- emission [10,11] shifted toward the low-wavelength region due to the presence of graphitic defect on NDs surface [12]. This is a first proof that the nitrogen contained in the target is incorporated in the forming NDs upon laser irradiation. Wide-field imaging analysis is shown in Fig 7.2(a) for the bright field and in 7.2(b) for the fluorescent imaging (532 nm excitation source) of the same sample region. As expected, not all the ablated graphite is converted into NDs. Indeed, the powder shows a strong PL, but a part of the ablated material does not present any emission. For instance, Fig. 7.2(c) gives an optical image of a micrometer-sized cluster, while the corresponding PL image is reported in Fig. 7.2(d): as observed, only a portion of it shows a PL under 532 nm laser excitation. ODMR spectroscopy is performed over

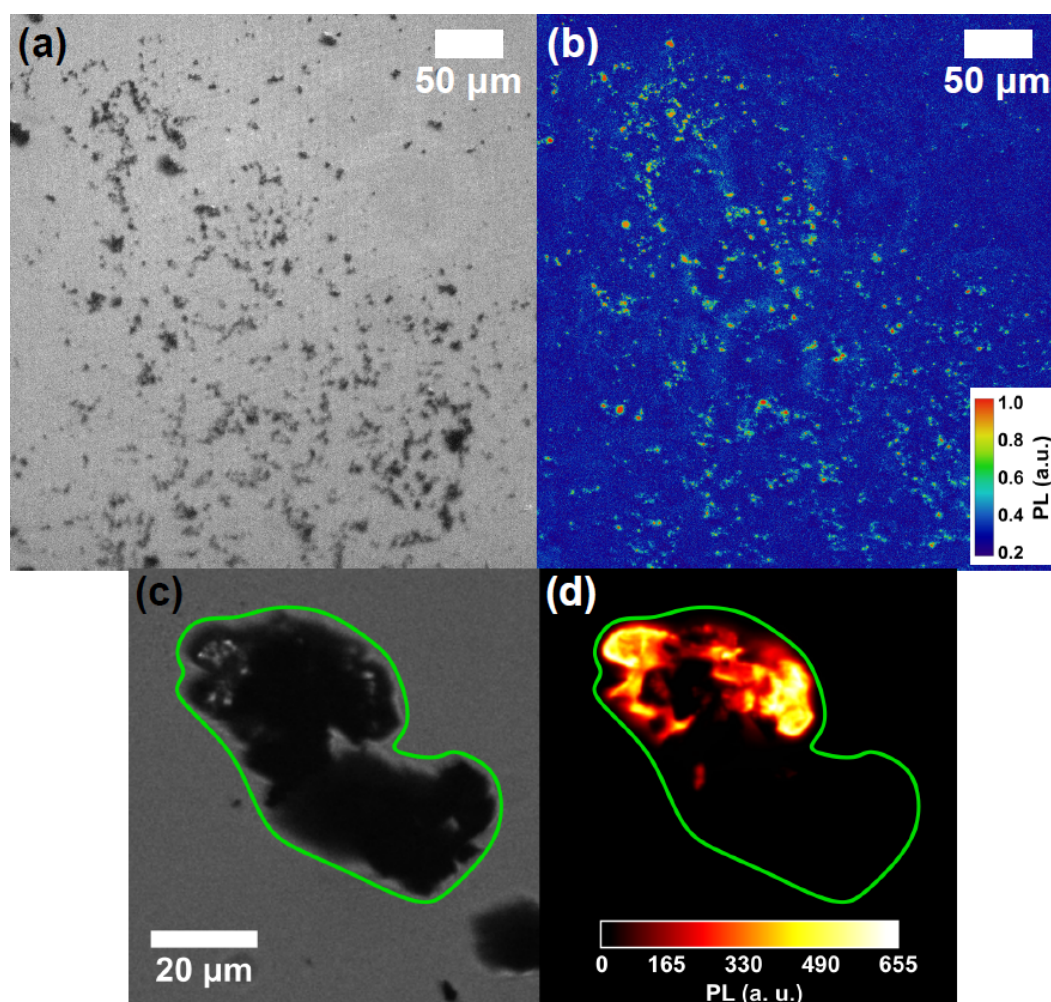


Fig. 7.2: Wide-field PL imaging of the laser-ablated powders. (a) bright field image obtained with a white lamp and (b) PL imaging of the same part of the sample with 532 nm excitation source. The bright spots in (b) are NV-fluorescent NDs. Detail of the same cluster in wide field (c) and PL imaging (d).

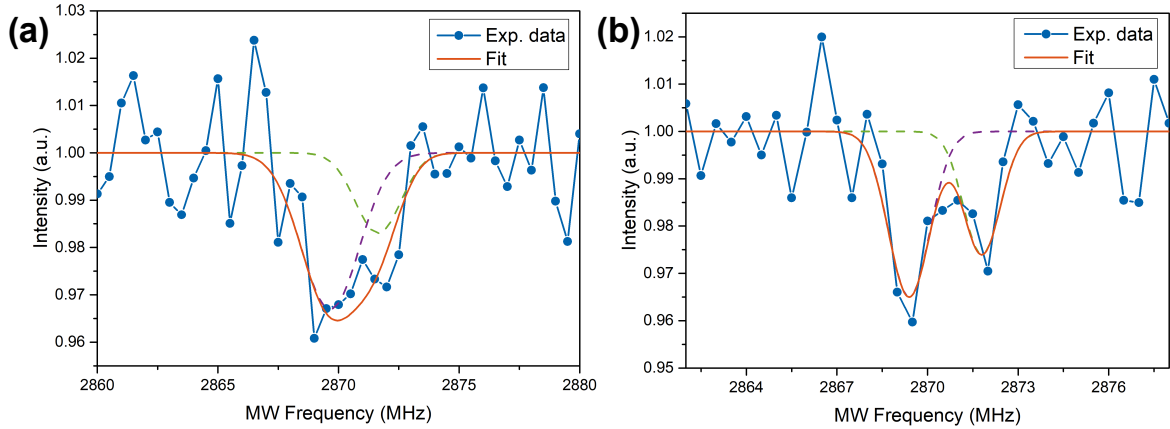


Fig. 7.3: Two typical ODMR spectra are reported in panels (a) and (b). The blue dots are the experimental data, whereas the dashed lines are the gaussians used to fit the two MW resonances. Their superposition is given by the orange line. The different splitting in the peaks composing the spectra are related to different strain field acting on the NDs hosting the NV centers.

the bright spots observed with PL imaging (Fig. 7.2(b)), to finally prove NV center formation inside the NDs. Two typical ODMR spectra in the MW range 2800-2900 MHz, obtained by monitoring the PL intensity under continuous laser excitation, are reported in Fig. 7.3. Both spectra show a decrease in PL emission at around 2870 MHz, thus proving NV^- origin of the observed PL [1]. The different split in the peaks composing the ODMR is a consequence of the different strain field acting on the NDs hosting the NV centers [6].

7.3.2 NDs production yield: role of the confining medium

Now that we have demonstrated the NV-enriched NDs synthesis through pulsed-laser ablation of N-doped graphite, this particular target is used to compare fluorescent NDs synthesis efficiency of different laser-assisted production techniques. Those are: laser ablation in water, in liquid nitrogen and in nitrogen atmosphere. Three different samples were prepared using the same N-doped graphite target which is laser irradiated in the three different media. To allow a proper comparison, the samples are produced with the same nominal condition, as described in the experimental section. The only change is the confining medium, to study its effect on the synthesis process. We do not expect any relevant difference in the produced NDs size or shape with the use of this particular target respect to standard pyrolytic graphite. This is already observed

in this chapter for ablation in water, where no main difference in the NDs structure is appreciated respect to the results reported in Chapter 4. PL imaging is used to compare the different fluorescence intensities. From the PL pictures, as the one shown in Fig. 7.2(b), the total intensity of the image is integrated after a proper background removal. For each sample, 10 images are collected and averaged. Fig. 7.4(a) reports the result of the analysis, where the PL intensity of the non-irradiated target (T), and the samples resulting of laser ablation in water (W), nitrogen atmosphere (N_2) and liquid nitrogen (LN_2) are compared. Typical PL imaging pictures are reported in Fig. 7.4(b) for the different samples. In term of fluorescent NDs production efficiency, the best result is obtained for ablation in liquid nitrogen. This sample shows an intensity 22 ± 4 times higher respect to the untreated target. Moreover, the LN_2 sample shows a double intensity respect to ablation in nitrogen atmosphere. This is a consequence of the different ablation plume expansion dynamics in a liquid or vapor

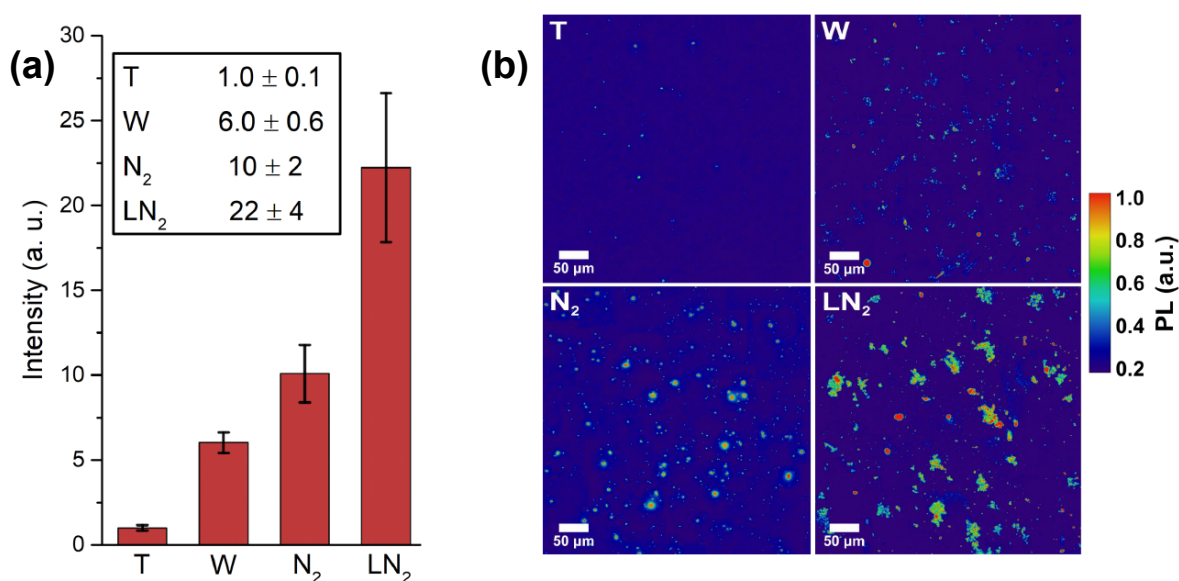


Fig. 7.4: Effect of the confining medium on fluorescent NDs synthesis efficiency. (a) The different samples are labeled as: non-irradiated target (T), ablation in water (W), in nitrogen atmosphere (N_2) and in liquid nitrogen (LN_2). The total PL level for each sample is calculated as follows. Starting from a PL image, the total intensity is integrated after proper background removal. Then, this value is averaged for a series of 10 images: the result is plotted in the histograms in panel (a). The values reported in the inset in (a) are normalized respect to the one of the initial target T, to have a direct comparison. The error bars are the standard deviations of the 10 images set. (b) Typical PL images of the four samples after background subtraction, used to calculate the total PL level in (a).

medium [13, 14]. The details of the thermodynamic model describing formation of NDs in the two cases are deeply described in Chapter 5 and 6, here only a brief summary is given. When the ablation is performed in a dense environment such as a liquid, the thermodynamic conditions required for diamond phase formation - namely pressure, temperature and rapid quenching of the plume [15, 16] - are enhanced in the inner of the ablation plume [4, 17]. Regarding the pressure, the ablation process in a 1 Pa nitrogen atmosphere brings to a pressure inside the ablation plume of 220 MPa, much lower than the pressure of ~ 3.5 GPa reached for ablation in liquid nitrogen. For this reason a larger efficiency in the synthesis of fluorescent NDs is expected for ablation in liquid nitrogen, as an high pressure state favors the formation of diamond phase during laser ablation of graphite [18]. The other process that allow to explain the observation of Fig. 7.4 is the quenching of the ablation plume. Indeed, the lifetime of the plume expanding in LN₂ is much shorter due to a more efficient collisional cooling, reaching cooling rate of 10^{11} K/s [19], compared to expansion in a rarefied environment such as nitrogen atmosphere. The longer lifetime during laser ablation in N₂ leads to a larger sp² carbon atoms contamination of the forming NDs. As a matter of fact, in this condition chemical reactions in the plume occur when temperature and pressure are decreased and no longer the ones required for diamond phase formation. The result is the deposition of NDs with a more significant sp² shell. Thus, N₂ sample is expected to show a weaker luminescence emission because graphitic layers covering NDs are reported to quench NV emission intensity [20]. Summarizing, the stronger observed PL emission for LN₂ sample (shown in Fig. 7.4(a)) can be explained by the higher NV-hosting NDs synthesis efficiency, due to larger pressure and rapid quenching, compared for instance to the N₂ case. Lastly, the less luminescent sample is the one obtained by ablation in water. This can be easily explained considering that the ablation in a nitrogen containing media brings to dissociation of N₂ molecules of the liquid/atmosphere [6, 7], providing an additional source of nitrogen doping. On the opposite, fluorescence in the sample W relies only in the nitrogen atoms contained in the target, that are subsequently incorporated by the NDs formed upon ablation, thus leading to a smaller density of NV centers in the NDs.

7.3.3 NDs production yield: role of the target

In this section, the effect on NV-synthesis efficiency of N-doping concentration in the target used for laser ablation is studied. To do that, a graphite target with a lower

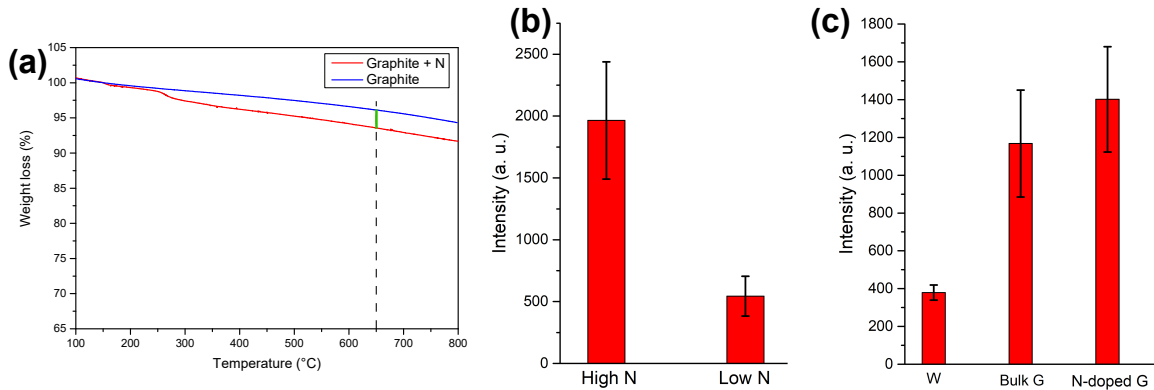


Fig. 7.5: Effect of the target on fluorescent NDs synthesis efficiency. (a) TGA analysis of the target with low nitrogen doping (“Low N” target). By measuring the weight loss of the N-doped graphite (red line) respect to untreated graphite (blue line) at 650°C (green line) nitrogen content is extracted. (b) Comparison of the PL intensities of the NDs laser-synthesized in water from the “High N” and “Low N” target. The total PL level is extracted in the usual way, by averaging a series of PL pictures. (c) Study on the most relevant nitrogen source in NV-production efficiency. PL intensity comparison between N-doped graphite ablated in water (W) and laser ablation in liquid nitrogen of standard pyrolytic graphite (Bulk G) and N-doped graphite target (N-doped G). In both (b) and (c) the PL intensity is obtained by integrating 10 images after background subtraction. The error bars are the standard deviations.

N-doping level is prepared. With TGA analysis (Fig. 7.5(a)) the nitrogen concentration is estimated to be 5.8 mg/g of graphite. This target, that will be referred as “Low N”, is compared with the target used in the first part of this chapter, that from now on will be called “High N”. The latter, as described previously, has a nitrogen concentration of 23.3 mg/g of graphite, that is ~ 4 times higher respect to the “Low N”. The two targets are laser-ablated in water with the same nominal condition, and comparison between the two samples is performed with PL imaging. As the aim of the experiment was to study the effect of the initial nitrogen doping in the target, the laser-irradiation is performed in a medium that does not bring to an additional nitrogen doping, namely water. Fig. 7.5(b) reports the result of the PL imaging analysis. A higher doping in the target does bring to a higher concentration of NV in the formed NDs, as the “High N” sample shows a larger PL intensity. Of particular interest is the following observation. The ratio between the two samples PL intensity is 4 ± 1 , consistent with the ratio between the initial nitrogen doping. Hence, the NV concentration in the laser-synthesized NDs is proportional to the nitrogen concentration in the initial target, meaning that the NDs PL emission intensity depends linearly on the target N-doping.

As a consequence, by varying nitrogen doping in the target used for laser ablation NDs fluorescence may be tuned. This result represents the first step into establishing a route for controlling the number of NV centers the synthesis of NDs. Finally, with the aim of establishing if the dominant source of nitrogen atoms to form NV centers in the NDs is the nitrogen contained in the target or in the confining medium, a last comparison is performed. Two samples are prepared, one by using as a target the nitrogen doped graphite ("N-doped G" sample) the other by using standard pyrolytic graphite ("Bulk G" sample), both by laser-ablation in liquid nitrogen. The two are compared with the W sample, namely the fluorescent NDs obtained by ablation in water of the N-doped graphite powder. The comparison, studied through PL imaging, is reported in Fig. 7.5(c). As expected, the ablation of the same N-doped target in liquid nitrogen respect to water brings to higher fluorescent NDs. Interestingly, the "Bulk G" and "N-doped G" have the same PL intensity, within the experimental errors. These two observations allows us to conclude that, at the present doping level of the target, the most relevant source of nitrogen atoms to form NV centers in the NDs is the liquid medium, *i.e.* liquid nitrogen.

7.4 Conclusions

In conclusion, the synthesis of NDs hosting NV^- centers through pulsed laser ablation of a nitrogen doped graphite target is demonstrated. Morphology and crystal structure of the NDs are fully characterized, as well as NDs optical properties. Furthermore, presence of NV centers in the NDs is unequivocally proved by optically detected magnetic resonance. With the aim of finding the best condition for the production of NV-doped NDs, the N-doped graphite target is then used to compare different laser-ablation based techniques, namely laser ablation of graphite in liquid nitrogen and in a nitrogen atmosphere. In terms of fluorescent NDs formation efficiency, the best result is obtained for ablation in liquid nitrogen: an explanation of the physical processes leading to this outcome is provided. Then, a linear dependence between the nitrogen concentration in the target and the NV-emission intensity is demonstrated. This could open a way to develop a synthesis technique of fluorescent NDs with a tunable NV concentration. Finally, we shows that, at the present N-doping level of the graphite target, the confining medium plays the most relevant role as nitrogen source in NV formation.

References for chapter 7

- [1] L. Rondin, J.P. Tetienne, T. Hingant, J.F. Roch, P. Maletinsky, V. Jacques, Magnetometry with nitrogen-vacancy defects in diamond. *Rep. Prog. Phys.* 77 (2014) 056503.
- [2] E. Abe, K. Sasaki, Tutorial: Magnetic resonance with nitrogen-vacancy centers in diamond—microwave engineering, materials science, and magnetometry, *J. Appl. Phys.* 123 (2018) 161101
- [3] A. Tallaire, O. Brinza, M. De Feudis, A. Ferrier, N. Touati, L. Binet, Synthesis of Loose Nanodiamonds Containing Nitrogen-Vacancy Centers for Magnetic and Thermal Sensing, *ACS Appl. Nano Mater.* 2 (2019) 5952-5962.
- [4] F. Gorrini, M. Cazzanelli, N. Bazzanella, R. Edla, M. Gemmi, V. Cappello, On the thermodynamic path enabling a room-temperature, laser-assisted graphite to nanodiamond transformation, *Sci. Rep.* 6 (2016) 35244.
- [5] L. Basso, F. Gorrini, N. Bazzanella, M. Cazzanelli, C. Dorigoni, A. Bifone, A. Miotello, The modeling and synthesis of nanodiamonds by laser ablation of graphite and diamond-like carbon in liquid-confined ambient, *Appl. Phys. A*, 124 (2018) 72.
- [6] L. Basso, F. Gorrini, M. Cazzanelli, N. Bazzanella, A. Bifone, A. Miotello, An all-optical single-step process for production of nanometric-sized fluorescent diamonds, *Nanoscale*, 10 (2018) 5738-5744.
- [7] L. Basso, N. Bazzanella, M. Cazzanelli, A. Miotello, On the route towards a facile fluorescent nanodiamonds laser-synthesis, *Carbon*, 153 (2019) 148-155.
- [8] A.C. Ferrari, J. Robertson, Raman spectroscopy of amorphous, nanostructured, diamond-like carbon, and nanodiamonds, *Phil. Trans. Roy. Soc. Lond.* 362 (2004) 2477-2512.
- [9] S. Praver, K.W. Nugent, D.N. Jamieson, J.O. Orwa, L.A. Bursill, J.L. Peng, The Raman spectrum of nanocrystalline diamond, *Chem. Phys. Lett.* 332 (2000) 93-97.
- [10] C. Bradac, T. Gaebel, N. Naidoo, M.J. Sellars, J. Twamley, L.J. Brown, Observation and control of blinking nitrogen-vacancy centres in discrete nanodiamonds, *Nat. Nanotech.* 5 (2010) 345.
- [11] P.H. Chung, E. Perevedentseva, C.L. Cheng, The particle size-dependent photoluminescence of nanodiamonds, *Surf. Sci.* 601 (2007) 3866-3870.
- [12] A.R. Kirmani, W. Peng, R. Mahfouz, A. Amassian, Y. Losovyj, H. Idriss, K. Katsiev, On the relation between chemical composition and optical properties of detonation nanodiamonds, *Carbon*, 94 (2015) 79-84.
- [13] C.Y. Shih, M.V. Shugaev, C. Wu, L.V. Zhigilei, Generation of subsurface voids, incubation effect, and formation of nanoparticles in short pulse laser interactions

- with bulk metal targets in liquid: Molecular dynamics study, *J. Phys. Chem. C*, 121 (2017) 16549-16567.
- [14] S.S. Harilal, C.V. Bindhu, M.S. Tillack, F. Najmabadi, A.C. Gaeris, Internal structure and expansion dynamics of laser ablation plumes into ambient gases, *J. Appl. Phys.* 93 (2003) 2380-2388.
- [15] C.Y. Shih, C. Wu, M.V. Shugaev, L.V. Zhigilei, Atomistic modeling of nanoparticle generation in short pulse laser ablation of thin metal films in water, *J. Colloid Interface Sci.* 489 (2017) 3-17.
- [16] K. Saito, K. Takatani, T. Sakka, Y.H. Ogata, Observation of the light emitting region produced by pulsed laser irradiation to a solid-liquid interface, *Appl. Surf. Sci.* 197 (2002) 56-60.
- [17] D. Amans, A.C. Chénus, G. Ledoux, C. Dujardin, C. Reynaud, O. Sublemontier, Nanodiamond synthesis by pulsed laser ablation in liquids, *Diam. Relat. Mater.* 18 (2009) 177-180.
- [18] C.X. Wang, P. Liu, H. Cui, G.W. Yang, Nucleation and growth kinetics of nanocrystals formed upon pulsed-laser ablation in liquid, *Appl. Phys. Lett.* 87 (2005) 201913.
- [19] Z. Yan, D.B. Chrisey, Pulsed laser ablation in liquid for micro-/nanosstructure generation, *J. Photoch. Photobiol. C*, 13 (2012) 204-223.
- [20] B.R. Smith, D. Gruber, T. Plakhotnik, The effects of surface oxidation on luminescence of nano diamonds, *Diam. Relat. Mater.* 19 (2010) 314-318.

Conclusions

In the present thesis, our results regarding the use of pulsed laser ablation in the synthesis of fluorescent nanodiamonds (NDs) are described. We demonstrated that this particular technique, which has been used for the production of large variety of nanoparticles, allows the synthesis of nanodiamonds and, most importantly, to the direct formation of nitrogen-vacancy (NV) centers inside diamond nanostructures. A general overview of the context in which this work was developed, in particular the motivation that is pushing the research activity in this field, as well as the details of the thesis content are given in Chapter 1.

Then, an introduction on NV centers physics is provided in Chapter 2, where details on the crystal and electronic structure of this particular defect of diamond lattice, together with the description of its optical properties, are reported. A great interest is placed in the description of the spin-Hamiltonian used to describe the NV, that is essential to explain NV optical transitions dependence to environmental parameters, such as temperature or electromagnetic field. Moreover, ODMR spectroscopy - in particular the physical process behind this technique - is described, as it is the main NV characterization technique used here. Finally, a quick overview on NV centers application in quantum technology is given, with a focus on quantum sensing and quantum information.

Chapter 3 provides a description of NDs properties and consequent potential applications that have been proposed for this peculiar nanoparticle. Furthermore, the main NDs synthesis technique that are currently commercially available, also for NV-enriched NDs, are detailed. The second part of this chapter is devoted to pulsed laser ablation (PLA). The peculiar aspects of this techniques are highlighted, as they are used in the experimental chapters of the thesis to explain NDs formation upon PLA of graphite. The results obtained for synthesis of NDs though PLA of graphite in water are reported in Chapter 4. We experimentally demonstrated that with this technique direct synthesis

of NDs is obtained, in a cheap and easily scalable process. Moreover, to explain diamond phase formation a thermodynamic model based on a graphite-liquid-diamond transition is developed. This model takes into account the extreme thermodynamic conditions reached during a PLA experiment, namely the high pressure, the high temperature and cooling rate. Once NDs production has been proven, the second part of this thesis regards the synthesis of NV-centers in NDs.

In Chapter 5 the first way in which we successfully synthesized fluorescent NDs is presented. PLA of graphite in a controlled nitrogen atmosphere is implemented. Our results clearly show that in a single-step process, diamond phase formation and nitrogen incorporation is achieved. Moreover, ODMR is used to estimate the native strain field acting on NDs.

NV-enriched NDs were also synthesized through PLA in liquid nitrogen (Chapter 6). Also in this case NV-origin of the observed fluorescence is confirmed by ODMR. Furthermore, in this chapter a comparison with the sample obtained in nitrogen atmosphere is performed, highlighting the good quality of the liquid-nitrogen-synthesized fluorescent NDs. Moreover, ODMR spectroscopy is used to study the NDs surface purity from sp^2 -carbon-related defects.

Finally, in Chapter 7, fluorescent NDs are obtained by PLA of N-doped graphite in water, thus using the ablated target as the source of nitrogen atom for NV formation, rather than the environment. This particular target is then used to perform a quantitative comparison between all the different NDs synthesis method employed in this thesis, showing that laser-irradiation in liquid nitrogen is the best route in term of NV-enriched NDs synthesis efficiency. This observation is explained in term of the thermodynamic model developed in Chapter 4.

The experimental observations reported in this thesis clearly show that pulsed laser ablation can provide a method for the synthesis of fluorescent NDs. These are relevant results for pushing the development of devices based on NV-centers in NDs for a number of applications. Indeed, the absence of a cheap and industrially scalable synthesis technique is one of the main factor limiting NV-based systems expansion. In particular, PLA allows to overcome most of the difficulties and drawbacks of the standard production techniques. For instance, post-synthesis processes to increase the NV concentration or to activate NV fluorescent are not needed and, remarkably, PLA permits a good control in NDs size (~ 30 nm). Furthermore, quantum sensing with laser-synthesized fluorescent NDs is demonstrated for "internal" parameters, such as

NDs native strain field and NDs surface purity. The future perspective of this activity may be the implementation of these laser-synthesized NDs for quantum sensing of "external" environmental parameters.